

# Material and mechanical properties of young basalt in drill cores from the oceanic island of Surtsey, Iceland

M.D. Jackson<sup>1,†</sup>, M.J. Heap<sup>2,3</sup>, G. Vola<sup>4</sup>, M. Ardit<sup>5</sup>, J.M. Rhodes<sup>6</sup>, J.G. Peterson<sup>7</sup>, N. Tamura<sup>8</sup>, and M.T. Gudmundsson<sup>9</sup>

<sup>1</sup>Department of Geology and Geophysics, University of Utah, Salt Lake City, Utah 84112, USA

<sup>2</sup>Université de Strasbourg, CNRS, Institut Terre et Environnement de Strasbourg, UMR 7063, Strasbourg F-67084, France

<sup>3</sup>Institut Universitaire de France, Paris 75231, France

<sup>4</sup>Cimprogetti S.R.L. The Green Edge of Lime Technologies, Dalmine 24044, Italy

<sup>5</sup>Department of Physics and Earth Science, University of Ferrara, Ferrara I-44122, Italy

<sup>6</sup>Department of Geosciences, University of Massachusetts, Amherst, Massachusetts 01003, USA

<sup>7</sup>Department of Geology and Geological Engineering, Colorado School of Mines, Golden, Colorado 80401, USA

<sup>8</sup>Advanced Light Source, Lawrence Berkeley National Laboratory, Berkeley, California 94720, USA

<sup>9</sup>Nordvulk, Institute of Earth Sciences, University of Iceland, Reykjavik 102, Iceland

## ABSTRACT

Characterization of 2017 drill core samples from Surtsey, an oceanic island produced by 1963–1967 eruptions in the offshore extension of Iceland's east rift zone, reveals highly heterogeneous microstructural, physical, and mechanical properties in subaerial, submarine, and subseafloor basaltic deposits. The connected porosity varies from 42% in weakly consolidated lapilli tuff in a submarine inflow zone to 21% in strongly lithified lapilli tuff in upper subseafloor deposits near the explosively excavated conduit. Permeability, however, varies over six orders of magnitude, from  $10^{-18}$  m<sup>2</sup> to  $10^{-13}$  m<sup>2</sup>. Uniaxial compressive strength, P-wave velocity, and thermal conductivity are also highly variable: 10–70 MPa, 1.48–3.74 km·s<sup>-1</sup>, and 0.472–0.862 W·m<sup>-1</sup>·K<sup>-1</sup>, respectively. Synchrotron X-ray microdiffraction analyses integrated with major-element geochemistry and quantitative X-ray powder diffraction analyses describe the initial alteration of fresh glass, incipient consolidation of a fine-ash matrix, and partial closure of pores with mineral cements. Permeability, micro-mechanical, and thermal property modeling highlight how porosity and pore size in eruptive fabrics—modified through diverse cementing microstructures—influence the physical properties of the pyroclastic deposits. Borehole temperatures, 25–141 °C (mea-


sured from 1980 to 2018), do not directly correlate with rock strength properties; rather, the abundance and consolidation of a binding fine-ash matrix appears to be a primary factor. Analytical results integrated with archival data from 1979 drill core samples provide reference parameters for geophysical and heat transfer studies, the physical characteristics of pyroclastic deposits that lithify on a decadal scale, and the stability and survival of oceanic islands over time.

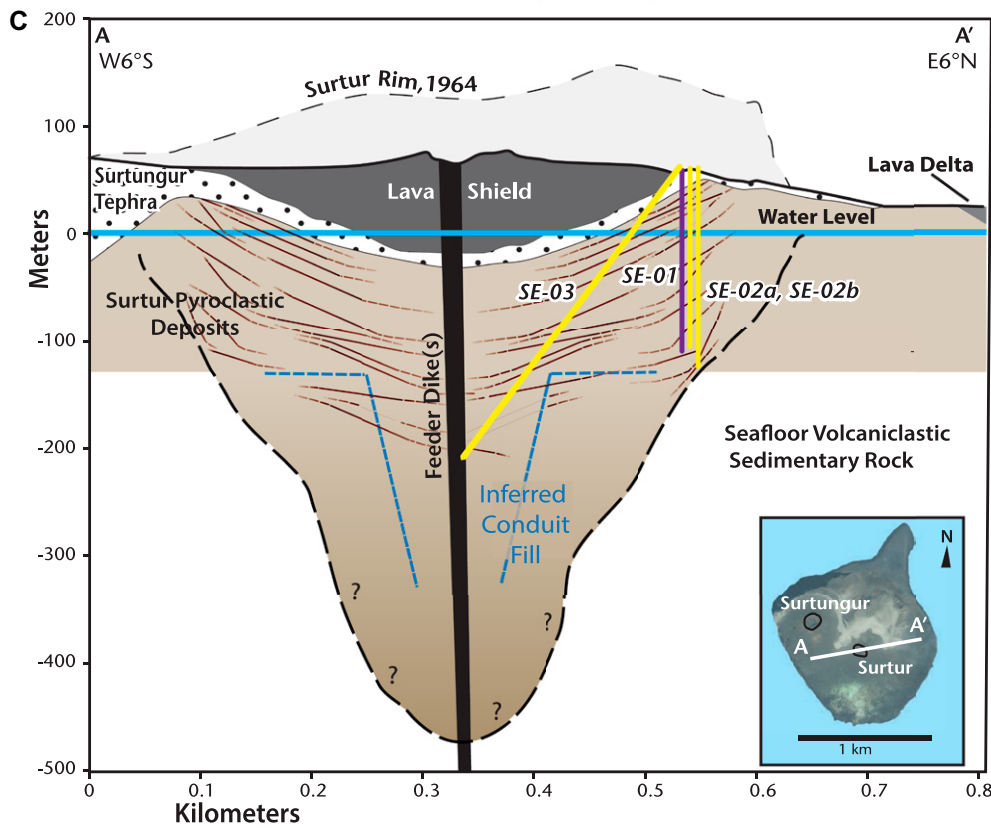
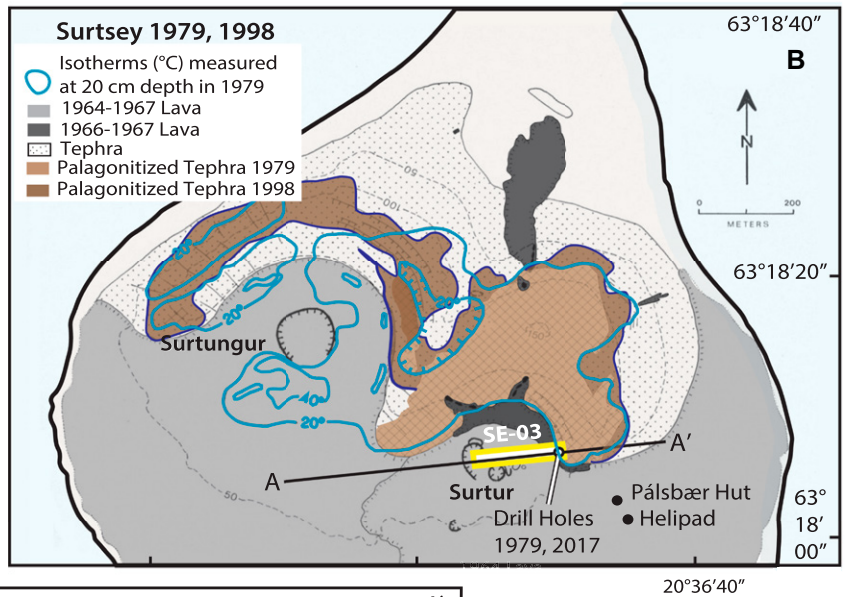
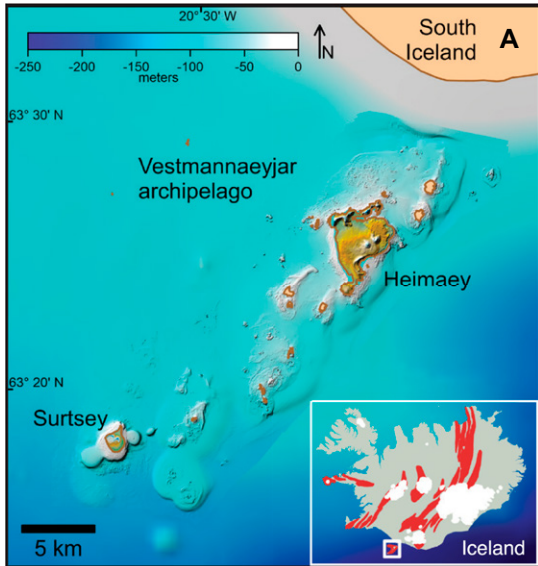
## INTRODUCTION

Surtsey is a young oceanic island that grew from the seafloor during 1963–1967 eruptions in the offshore extension of the east Icelandic rift zone (Thorarinsson et al., 1964; Thorarinsson, 1967; Fig. 1). The island has been monitored continuously since eruption began on 14 November 1963. It thus offers a unique natural experiment and precise record of the eruptive processes, primary volcanic fabrics, and early hydrothermal mineralization that influence the diagenesis, lithification, and physical characteristics of basalt in Earth's oceanic crust. The composition of the basalt; the alteration of subaerial, submarine, and subseafloor pyroclastic deposits; and the evolution of diverse subsurface microbial communities have been investigated in time-lapse drill cores acquired in 1979 and 2017 from Surtur crater, which erupted from November 1963 to April 1964 (Jakobsson and Moore, 1982, 1986; Marteinson et al., 2015; Schipper et al., 2015; Jackson et al., 2019a, 2019b; Kleine et al., 2020; Prause et al., 2020, 2022; Bergsten et al., 2021, 2022).

The Jakobsson and Moore (1986) *Geological Society of America Bulletin* article describes hydrothermal minerals and rates of alteration—the cumulative changes in rock composition, mineralogy, texture, and physical characteristics—in subaerial and submarine basaltic deposits during the 15 years after Surtur eruptions terminated. Here, these archival descriptions are integrated with laboratory measurements of the material and physical properties of 2017 drill cores and the results of mineralogical, geochemical, and modeling investigations not available in the 1980s. These data extend the legacy of the Jakobsson and Moore (1986) research and create an updated reference for future longitudinal studies of the subsurface structure of Surtsey.

Authigenic alteration of volcanic glass and the crystallization of mineral cements—zeolites, calcium-silicate hydrates, sulfites, and carbonates—induces changes in the material and mechanical properties of pyroclastic deposits. These changes influence the reservoir characteristics of geothermal systems in Iceland (Franzson et al., 2001; Lévy et al., 2018; Eggertsson et al., 2020; Nono et al., 2020; Scott et al., 2023); provide insights into ground deformation modeling and the stability of active and quiescent volcanoes (Vanorio et al., 2002; Vinciguerra et al., 2009; Zhu et al., 2011; Heap et al., 2014, 2015, 2017a; Marmoni et al., 2017; Heap and Violay, 2021); and define relationships among porosity, strength, and permeability in basalt (Fisher, 1998; Saar and Manga, 1999; Walker et al., 2013; Schaefer et al., 2015; Violay et al., 2015; Di Muro et al., 2021). The evolution of physical characteristics is difficult to decipher in ancient pyroclastic deposits, however. Only a

M.D. Jackson  <https://orcid.org/0000-0002-5180-3060>  
†m.d.jackson@utah.edu



### Structural and Hydrothermal Zones

- 1 Subaerial tuff cone
- 2 Tidal flux zone
- 3 Upper submarine lapilli tuff
- 4 Submarine inflow zone
- 5 Lower submarine tephra and lapilli tuff
- 6 Upper subseafloor lapilli tuff
- 7 Lower subseafloor lapilli tuff and basaltic intrusion
- 8 Seafloor sedimentary rock

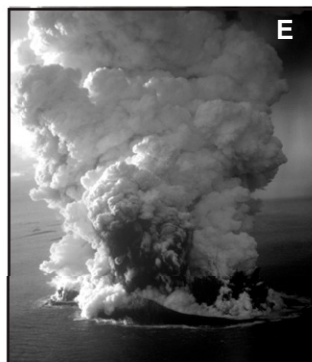
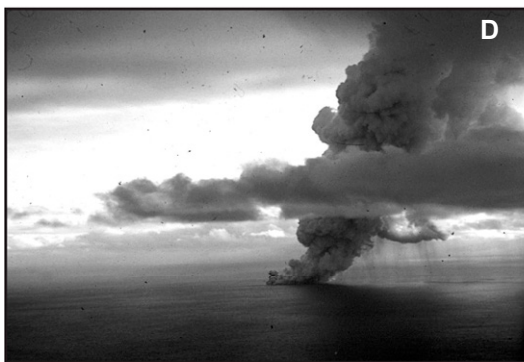


**Figure 1.** (A) Map of the Vestmannaeyjar archipelago in the offshore extension of the eastern Icelandic rift zone (bathymetry: Icelandic Coast Guard). Red zones on the map of Iceland show volcanic systems (after Jackson et al., 2019b). (B) Geologic map of Surtsey, Iceland, shows palagonitized tuff in 1979 and 1998 (after Jakobsson and Moore, 1982; Jakobsson et al., 2000). (C) Cross section of Surtur shows the 1979 SE-01 cored borehole (black) and 2017 cored boreholes (yellow), the principal zones of Surtur deposits, and seafloor volcanoclastic sedimentary rocks. Beds defined by grain size differences follow orientations from McPhie et al. (2020) and Moore and Jackson (2020). Black dashed line—subseafloor diatreme inferred by Moore (1985). Blue dashed line—minimum subsurface vent and conduit deposits that fit 2017 drilling results (after Jackson et al., 2019b). Surtsey in eruption on (D) 14 November 1963, (E) 30 November 1963, and (F) in spring 1964 (courtesy of T. Mann and R.J. Carson).

few experimental studies document how physical characteristics evolve as pyroclastic deposits consolidate to form rock (e.g., Heap et al., 2020a; Kennedy et al., 2022).

### Material Evolution in Products of Surtseyan Volcanism

Explosive hydrovolcanic eruptions, including Surtseyan-type eruptions (Németh and Kósik, 2020), in which magmas interact explosively with shallow bodies of water in oceanic rift zones, subglacial terrains, and continental lakes, have been recognized in submarine, subglacial,

and lacustrine environments around the world. For example, these include Pahvant Butte (Utah, USA, 15 ka; Gilbert, 1890; White, 1996; Verolino et al., 2018), Capelinhos (Azores, 1957–1958; Cole et al., 2001), Gjálp (Iceland, 1996; Jakobsson and Gudmundsson, 2008), Hunga Tonga–Hunga Ha’apai (Tonga, 2014–2015 and 2022; Colombier et al., 2018; Terry et al., 2022), and Anak Krakatau (Sunda Strait, Indonesia, 2018; Grilli et al., 2019; Walter et al., 2019).

The alteration of basalt in water-rich environments contributes to chemical, mineralogical, and biomediated changes in Earth’s continental and oceanic crust (e.g., Stefánsson and Gisla-

son, 2001; Fisher and Wheat, 2010; Staudigel, 2014; Nikitzuk et al., 2016; Kleine et al., 2020). This alteration is commonly considered to occur through palagonitization, a poorly defined process that proceeds through a continuum of chemical interactions of basaltic glass and crystals with water and microbial activity (e.g., Staudigel and Hart, 1983; Stroncik and Schmincke, 2002; Fisk et al., 2003). The terms sideromelane, an ideal, rapidly cooled basic glass, and palagonite, the hydration product of sideromelane, were proposed in 1853 before petrographic microscopy was commonly in use (von Waltershausen, 1853). Palagonite now indicates an alteration product of basalt associated with diverse mineral assemblages (Peacock and Fuller, 1928; Stroncik and Schmincke, 2002), principally clay, zeolite, and calcium-silicate hydrate minerals (e.g., Hay and Iijima, 1968; Jakobsson and Moore, 1986; Pauly et al., 2011). Recent investigations of authigenic microstructures in basalt with transmission electron microscopy and synchrotron applications describe the complexity of alteration processes at the submicrometer scale (e.g., Zhou et al., 1992; Benzerara et al., 2007; Jackson et al., 2019a; Smith and Horgan, 2021). In this article, fresh basaltic glass is confirmed with micro X-ray diffraction ( $\mu$ XRD) analysis. Authigenic fabrics and mineral cements are described with microscopy and quantitative phase analysis of X-ray powder diffraction data (QPA-XRPD).

### A Window into Very Young Oceanic Basalt

Poorly sorted lapilli tuff, comprising ash (<2 mm) to medium-sized lapilli (8–10 mm), with variable proportions of very fine ash, forms ~95 vol% of the 2017 Surtur drill cores (White and Houghton, 2006; McPhie et al., 2020). (Tephra refers to unconsolidated fragmental juvenile vitric and crystal components and seafloor lithic components of the Surtsey eruption.) This research investigates 16 core segments collected in 2017 from eight structural and hydrothermal zones (Figs. 1 and 2): (1) subaerial tuff cone, 0–56 m below surface (m.b.s.) (B1 and B2); (2) zone of tidal flux, 56–65 m.b.s. (B3); (3) zone of current maximal temperatures in the submarine hydrothermal system, 65–142 m.b.s. (B4, B5, D8, and D9); (4) submarine inflow zone, 142–

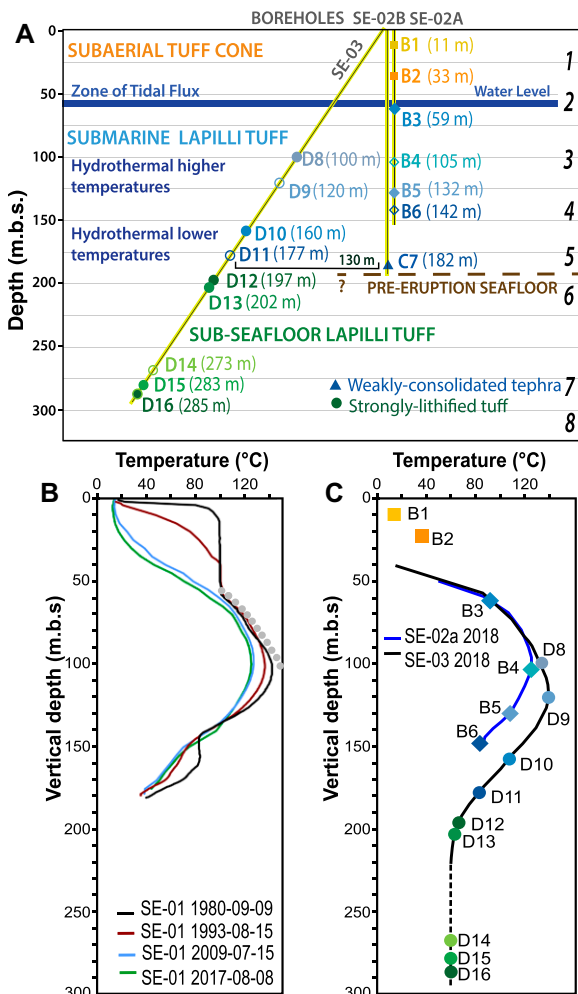


**Figure 2.** Surtur drill core samples and temperature measurements. (A) Core segment samples collected in 2017 (in vertical meters below surface, m.b.s.). Numbers show vertical structural and hydrothermal zones (see Fig. 1C). (B) SE-01 borehole temperatures measured in 1980, 1993, 2009, and 2017; gray dotted line is the 1980 boiling point curve (after Jakobsson and Moore, 1986; Jakobsson et al., 2019b). (C) SE-02a and SE-03 borehole temperatures measured in 2018 (Weisenberger et al., 2021).

155 m.b.s. (B6); (5) lower submarine tephra and lapilli tuff, 145–186 m.b.s. (C7, D10, and D11); (6) uppermost subseafloor lapilli tuff, 195–205 m.b.s. (D12 and D13); (7) lower subseafloor lapilli tuff, 205–285 m.b.s. (D14 and D15) and basaltic intrusion (D16); and (8) xenoliths of volcanoclastic sedimentary rocks of the pre-eruption seafloor. These zones, with some variations, are described in previous publications (Jakobsson and Moore, 1982, 1986; Jackson et al., 2019a; Jackson, 2020; Kleine et al., 2020; McPhie et al., 2020; Moore and Jackson, 2020; Prause et al., 2020, 2022; Bergsten et al., 2021, 2022; Montesano et al., 2023).

Subaerial deposits of Surtseyan volcanism are typically poorly sorted, with beds rich in ash-sized fragments punctuated by larger composite bombs. Subaqueous deposits may also include horizons of vesicular tephra with little fine ash-sized fraction (White, 1996; Verolino et al., 2022). At Surtur, those coarse-grained horizons occur in the submarine inflow zone (4); lower submarine, weakly consolidated tephra and lapilli tuff (5); and intermittently in deep-submarine and subseafloor deposits (6). Elsewhere, very fine- to medium-sized ash (0.063–0.500 mm in diameter) forms a binding matrix that includes mineral cements, particularly in well-lithified lapilli tuff (McPhie et al., 2020). Layers defined by grain size differences have apparent dip toward the central conduit that averages 48° (Moore, 1985; McPhie et al., 2020; Moore and Jackson, 2020; Fig. 1C).

Consolidation of the Surtur pyroclastic deposits began with explosive hydrovolcanism and explosive reworking of tephra to produce submarine and subseafloor slump and slide deposits (Jakobsson and Moore, 1982; Moore, 1985; McPhie et al., 2020; Moore and Jackson, 2020). Chemical and mineralogical changes in basaltic glass and primary crystals, olivine (Fo<sub>75-87</sub>), plagioclase (An<sub>53-80</sub>), and clinopyroxene (Jakobsson, 1979; Wenk et al., 1980; Schipper et al., 2015) at wide-ranging temperatures and fluid compositions (Kleine et al., 2020) then produced heterogeneous alteration fabrics (Jakobsson and Moore, 1986; Jackson et al., 2019a; Prause et al., 2020, 2022). In 1979, higher temperature subaerial and submarine deposits consolidated to become lapilli tuff (Jakobsson and Moore, 1982, 1986), but unaltered, unlithified tephra occupied much of the lower 42 m of the SE-01 borehole. In 2017, weakly consolidated deposits occurred only at ~146–148 m.b.s. and below ~182 m.b.s. (McPhie et al., 2020).

This research integrates laboratory measurements of physical properties with descriptions of eruptive and in situ alteration fabrics from the 1979 and 2017 drill cores to investigate how lithification of tephra progressed at Surtsey 50

years after eruptions terminated. The research addresses five principal questions:

(1) How can the earliest stages of tephra lithification be quantified?

(2) How do material and mechanical properties of the lapilli tuff deposits vary? Do mineral cements play the most important role in increasing rock compressive strength? Or do interdependent changes in eruptive fabrics—tephra particle size distribution, initial porosity, and permeability—create a primary framework for development of rock strength?

(3) How have rates of lithification varied since drilling in 1979?

(4) What is the current state of the Surtsey structure? Could a weak submarine inflow zone threaten the stability of the young island? What subsurface features could allow the island to persist as a subaerial feature of the Vestmannaeyjar archipelago?

(5) What do the physical characteristics of the Surtur pyroclastic deposits reveal about Surtseyan volcanoes worldwide? More specifically, how do volcanic islands stabilize themselves and resist erosion over time?

## GEOLOGIC CONTEXT

The birth of Surtsey occurred through explosive interactions of basaltic magma with seawater in 1963–1964, followed by effusive eruptions of lavas from the Surtur and Surtungur craters in 1964–1967 (Thorarinsson et al., 1964; Thorarinsson, 1967; Fig. 1). Surficial deposits have been comprehensively described (e.g., Thorarinsson, 1967; Lorenz, 1974; Jakobsson et al., 2000; Óskarsson et al., 2020). A 181-m-deep cored borehole (SE-01; Hole A) drilled in 1979 (Figs. 1 and 2) traversed subaerial and submarine deposits at borehole temperatures of 25–141 °C, as measured in 1980 (Jakobsson and Moore, 1982, 1986). The borehole terminated in unconsolidated tephra at 40 °C near the depth of the pre-eruption seafloor, ~130 m below sea level (m.b.s.l.) (Thorarinsson et al., 1964; Thors and Jakobsson, 1982; Jakobsson et al., 2009). Variable rates of alteration, measured through the thickness of authigenic mineral layers on olivine crystal fragments and sideromelane pyroclasts, appeared to be mainly related to hydrothermal temperatures (Jakobsson and Moore, 1986; Prause et al., 2020, 2022).

The Surtsey Underwater Volcanic System for Thermophiles, Alteration Processes and Innovative Concretes (SUSTAIN) drilling project, sponsored by the International Continental Scientific Drilling Program (ICDP), acquired two vertical drill cores in 2017 (SE-02A and SE-02B; ICDP Holes B and C) that extend to 151 m.b.s. and 192 m.b.s., respectively (Figs. 1 and 2; Jackson

et al., 2019b; Weisenberger et al., 2019). While the lowermost core recovered in SE-02B is Surtur tephra (~186 m.b.s.), no core was recovered in the bottom 4 m of the borehole. Thus, the minimum depth to the pre-eruption seafloor at this locality is 128–130 m.b.s.l., similar to previous estimates (Thorarinsson et al., 1964; Thors and Jakobsson, 1982; Jakobsson et al., 2009). An inclined cored borehole (SE-03; ICDP Hole D) plunges ~55° from horizontal in a 264° azimuthal direction. It extends to ~354 m measured depth (along the length of the inclined borehole) and ~294.7 vertical m.b.s. beneath Surtur crater. The core reaches into subseafloor pyroclastic basalt and occasional intrusive basalt (McPhie et al., 2020) but never encounters intact seafloor volcanoclastic sedimentary rock. The contiguous basaltic deposits therefore confirm a subsurface pyroclastic eruptive conduit, or diatreme, postulated by Moore (1985). Earlier hypotheses, by contrast, assumed that the pre-eruption seafloor remained mainly intact underneath the eruptive vents (Thorarinsson, 1967; Kokelaar and Durant, 1983).

## MATERIALS AND ANALYTICAL AND EXPERIMENTAL METHODS

### Drill Core Samples

Sixteen core segments 30–35 cm in length were selected from the 2017 SUSTAIN vertical SE-02A (Hole B) and SE-02B (Hole C) cores, drilled as HQ (63.5 mm core diameter), and the inclined SE-03 core (Hole D), drilled as HQ to 214 m measured depth (175 m.b.s.) and NQ (47.6 mm core diameter) to ~354 m measured depth (Jackson et al., 2019b; Weisenberger et al., 2019; Figs. 1 and 2; Figs. S1 and S2 in the Supplemental Material<sup>1</sup>). In 2021, downhole measurements revealed that the average angle of the SE-03 borehole from vertical is 33.4° ± 0.2° rather than 35° (Weisenberger et al., 2022). The principal discrepancy begins at the transition from the HQ3 to NQ3 drill bit. The D8–D13 positions are largely correct, but the D14–D16 positions are up to 4.7 m.b.s. deeper than the planned borehole path and almost 8 m farther east. Sample elevations are referenced to coordinates in the ICDP digital information system (Table S1, without corrections).

<sup>1</sup>Supplemental Material. Supplemental Texts S1–S6 (including Equations S1–S7, Figures S1–S9, and Tables S1 and S2) and Supplemental Data S1 (physical property measurements) and S2 (QPA-XRPD results). Please visit <https://doi.org/10.1130/GSAB.S.24790482> to access the supplemental material, and contact editing@geosociety.org with any questions.



The lapilli tuff samples have uniform fabrics without coarse lapilli, xenolithic (non-juvenile) clasts, slumps, or shear planes. Temperature data were measured in the SE-01 borehole in August 2017, prior to drilling the SE-02A and SE-02B boreholes (Fig. 2B). In 2018, temperatures were measured in the SE-02A borehole and inclined SE-03 borehole (Fig. 2C; Weisenberger et al., 2021); the 2018 SE-02A temperature data are mainly similar to the 2017 SE-01 data. Reference samples are half-core slices distributed to the SUSTAIN science team for collaborative research that includes measurements of material characteristics, whole-rock geochemistry, magnetic properties (Jackson et al., 2019b), petrographic studies (Prause et al., 2020), volumes of matrix pores (Moore and Jackson, 2020),  $\mu$ CT-derived image volumes (Kahl et al., 2021a, 2021b), and chemical analyses of mineralized phases (Montesano et al., 2023).

### Rock Testing Experiments

Rock properties were measured at the Strasbourg Institute of Earth and Environment (ITES), Strasbourg, France. Cylindrical subcores, cored to 20 mm diameter and precision-ground to a nominal length of 40 mm, were prepared from the drill core segments and seafloor rock. Core segment C7 disaggregated during coring. The subcores were then rinsed in water and vacuum dried at 40 °C for  $\geq 48$  h. Dry bulk-rock density was calculated using the dry mass and dimensions of the subcores. The connected porosity for each subcore was calculated using the skeletal volume measured by a helium pycnometer and the bulk sample volume measured using digital calipers. One subcore of each segment, deformed to failure under uniaxial compression (see below), was hand-powdered. The solid density of the segment was calculated using the mass and volume (measured using the helium pycnometer) of the powder. The total porosity was then calculated using the dry bulk-rock density of each subcore and the solid density of the segment from which the subcore was prepared. The isolated porosity was calculated by subtracting the connected porosity from the total porosity.

Permeability was measured for each vacuum-dry subcore using a benchtop gas (nitrogen) permeameter (Farquharson et al., 2015; Heap and Kennedy, 2016) at ambient temperature and under confining pressure of 1 MPa using either the steady-state method (for high-permeability samples) or the pulse-decay method (for low-permeability samples). For the steady-state experiments, steady-state volumetric flow rates were measured (using a gas flowmeter) for six different pore-pressure differentials (measured using a pressure transducer). Pulse-decay

measurements were performed by monitoring the decay of a pressure differential over time (measured using a pressure transducer). These data were used to calculate permeability using Darcy's law (Heap et al., 2017b). When necessary, data were corrected using the Klinkenberg or Forchheimer corrections.

P-wave velocity was measured along the sample axis on vacuum-dry subcores at ambient pressure and temperature. The subcores were held in a custom-built jig under an axial stress of 1 MPa to ensure good contact between the sample and the endcaps containing the piezoelectric sensors. The frequency of the signal, generated using a waveform generator, was set at 700 Hz, and the travel time was measured using a digital oscilloscope.

The thermal diffusivity and thermal conductivity of the vacuum-dry subcores were measured at ambient pressure and temperature with a Hot Disk TPS 500 Thermal Constants Analyzer using the transient plane source method (Gustafsson, 1991; Heap et al., 2020b). Thermal property measurements were performed using a sensor consisting of two 10-mm-thick nickel foil spirals insulated on both sides by 30- $\mu$ m-thick Kapton sandwiched between pairs of vacuum-dry subcores with similar porosities. Four measurements were made for each pairing. The volume-specific heat capacity provided by the Hot Disk TPS 500 was divided by the bulk sample density to provide the specific heat capacity of the bulk sample.

The uniaxial compressive strength of select subcores was measured using a uniaxial load frame. Vacuum-dry samples were deformed at ambient temperature at a strain rate of  $10^{-5}$  s $^{-1}$  until macroscopic failure. A lubricating wax was applied to the ends of each subcore to avoid friction between the sample and metal piston. Axial displacement and axial force were measured using a linear variable differential transducer and a load cell, respectively, and were converted to axial strain and axial stress using the sample dimensions. The deformation of the metal piston was removed from the measured displacement. The static Young's modulus was calculated using the stress-strain data from the elastic portion of the experiments (Heap et al., 2020c).

### Petrographic Studies

Studies of polished thin sections used an Olympus BX53M microscope in the Bowen Laboratory, Department of Geology and Geophysics, University of Utah, Salt Lake City, Utah, USA. Areas selected for synchrotron  $\mu$ XRD and micro X-ray fluorescence spectrometry ( $\mu$ XRF) investigations were cut from the glass-mounted thin section. The 0.03-mm-thick

rock slices were detached from the glass with nitromethane and mounted on adhesive tape for beamline experiments. Thin sections of Surtur tuff prepared in 1979 with glass coverslips were provided by J.G. Moore.

### Scanning Electron Microscopy Imaging and Energy-Dispersive Spectroscopy Analyses

Scanning electron microscopy (SEM) back-scattered electron (BSE) images and energy-dispersive spectroscopy (EDS) were obtained with the Zeiss EVOMA10 scanning electron microscope at the Department of Earth and Planetary Science at the University of California, Berkeley, California, USA. The imaging was performed at a beam energy of 15 keV and beam current of 850 pA. SEM-BSE images and EDS analyses were also obtained with the FEI Quanta 600F scanning electron microscope (ThermoFisher Scientific, Massachusetts, USA) at the Electron Microscopy and Surface Analysis Lab at the University of Utah, USA. Imaging was performed at a beam energy of 20 keV and beam current of 1 nA. Unpublished SEM secondary electron (SE) images from 1980 were provided by J.G. Moore.

### Quantitative Phase Analysis by X-Ray Powder Diffraction (QPA-XRPD)

X-ray powder diffraction (XRPD) experiments were performed on the subcore powders at the Cimprogetti Srl Laboratory, Dalmine, Italy. Each sample was finely ground in an agate mortar and mixed with 10 wt% zincite (ZnO, previously calibrated with the alumina National Institute of Technology standard reference material 676) as an internal standard for the quantification of crystalline phases and amorphous content (Snyder and Bish, 1989; Gualtieri et al., 2014). Samples were then side-loaded on a flat aluminum sample holder, and data collection was performed on a Miniflex 600 diffractometer (Rigaku, Tokyo) working in Bragg-Brentano geometry and equipped with a Cu-anode X-ray tube, an Ni filter to suppress the CuK $\beta$  component, and a D/teX ultrahigh-speed detector set to CuK $\alpha_{1,2}$  radiation. The powder was scanned in a continuous mode from 3° 2 $\theta$  to 90° 2 $\theta$ , with a step size of 0.02° 2 $\theta$  and counting time of 0.3 s per step. The identification of crystalline phases through qualitative phase analysis was performed with the PDXL2 software (Rigaku, Tokyo). Subsequently, XRPD patterns were modeled with the fundamental-parameter Rietveld approach (TOPAS v. 5.0, Bruker) for the quantification of identified crystalline phases (QPA) and amorphous content.

**Figure 3.** Petrographic micrographs from thin sections of 2017 Surtur core segments (see Fig. 2 for depth in vertical meters below surface [m.b.s.]) taken in plane-polarized light. (A) B1: 12.2 m.b.s., 96 °C in 1980, 15 °C in 2017. (B) B2: 35.0 m.b.s., 100 °C in 1980, 36 °C in 2017. (C) B3: 57.6 m.b.s., 102 °C in 1980, 87 °C in 2017. (D) B4: 105.0 m.b.s., 141 °C in 1980, 124 °C in 2017. (E) B5: 131.7 m.b.s., 109 °C in 1980, 105 °C in 2017. (F) B6: 141.8 m.b.s., 85 °C in 1980, 93 °C in 2017. (G) C7: 181.3 m.b.s., 40 °C at 181 m.b.s. in 1980, 44 °C at 175 m.b.s., 2017. (H) D8: 89.5 vertical m.b.s., 109.3 m measured depth, 125 °C in 2018. (I) D9: 109.1 vertical m.b.s., 133.2 m measured depth, 137 °C in 2018. (J) D10: 145.6 vertical m.b.s., 177.8 m measured depth, 120 °C in 2018. (K) D11: 178.9 vertical m.b.s., 217.9 m measured depth, 86 °C in 2018. (L) D12: 196.0 vertical m.b.s., 239.4 m measured depth, 67 °C in 2018. (M) D13: 198.0 vertical m.b.s., 241.4 m measured depth, 64 °C in 2018. (N) D14: 217.0 m.b.s., 330.8 m measured depth, 57 °C in 2018. (O) D15: 281.3 m.b.s., 344.2 m measured depth, 57 °C in 2018. Ol—olivine crystal fragments altered to lizardite (Table 1).

## Whole-Rock Geochemical Analyses

Major-element whole-rock elemental analyses were acquired from powdered subcores using fused La-bearing lithium borate glass disks and a Siemens MRS-400 multichannel, simultaneous X-ray spectrometer at the Ronald B. Gilmore X-Ray Fluorescence Laboratory in the Department of Geosciences at the University of Massachusetts, Amherst, Massachusetts, USA. The SE-01 tephra sample at 171 m.b.s. serves as a reference for the original unaltered tephra composition (Jackson et al., 2019b). Loss on ignition (LOI), determined at 1020 °C, includes adsorbed and combined H<sub>2</sub>O and CO<sub>2</sub>, and provides a guide to the abundance of hydrous and carbonate minerals.

## Synchrotron $\mu$ XRF and $\mu$ XRD Investigations

Experiments at Advanced Light Source beamline 12.3.2 investigated submicron-sized crystals with powder microdiffraction (Tamura, 2014; Stan and Tamura, 2018). The rock slice mounted on tape was loaded in transmission mode, with the detector placed at 39° to the incident beam. A monochromatic X-ray beam of 10 keV was focused to 2 × 5  $\mu$ m spot size. A DECTRIS Pilatus 1M area detector placed at ~150 mm recorded Debye rings from crystalline and nanocrystalline phases. The experimental geometry was calibrated using  $\alpha$ -Al<sub>2</sub>O<sub>3</sub> powder. X-ray diffractograms have *d*-spacing reflections integrated radially for 2 $\theta$  3°–54° over a 76° arc segment ( $\chi$ ) around the cone of diffraction. These are shown as plots of intensity versus *d*-spacing or intensity versus  $Q = 2\pi/d$ -spacing (Å), or  $Q$  (Å<sup>-1</sup>), to increase readability of lower *d*-spacing reflections. Numbered points correspond to a specific analysis referenced spatially in a qualitative calcium (Ca), iron (Fe), or titanium (Ti)  $\mu$ XRF scan.

## RESULTS

A process-oriented framework for deciphering measurements of physical characteristics begins with descriptions of the nanocrystalline

phases that initiate alteration in basaltic glass and the secondary crystalline phases that cement the lapilli tuff. The volcanic fabric, in situ mineralization, temperature history, and laboratory measurements of physical properties of each sample are then integrated to distinguish the diverse characteristics of the young deposits and create a template for comparison with other oceanic basalt systems.

## Mineralization of Tephra and Lapilli Tuff

### Initiation of Tephra Consolidation

Core segment C7, at 181.3 m.b.s., in the lower submarine zone (5) has translucent, yellowish gray (Munsell 5Y 7/2), apparently fresh glass visible in plane-polarized light (PPL) (Figs. 2A and 3G). XRPD identifies plagioclase and olivine as primary crystalline phases in the weakly consolidated tephra, as well as secondary anhydrite and gypsum (Figs. 4A and 4B). Authigenic incipient clay mineral(s) associated with altered glass give broad reflections. The bulk amorphous content is estimated at 84.6 wt% (Table 1).

By contrast, weakly consolidated lapilli tuff at 141.8 m.b.s., core segment B6, records the onset of tephra lithification in the seawater inflow zone (4) (Jakobsson and Moore, 1986; Jackson et al., 2019b). Translucent, yellowish gray (5Y 7/2), apparently fresh glass persists, yet opaque domains occur in larger pyroclasts and the ash matrix (Fig. 3F). XRPD identifies a broad peak centered at *d* = 14.7 Å associated with the (001) reflection of incipient clay mineral(s), which is more pronounced than that of C7 (Fig. 4B; Table 1). The amorphous content is  $\leq$ 81.1 wt%.

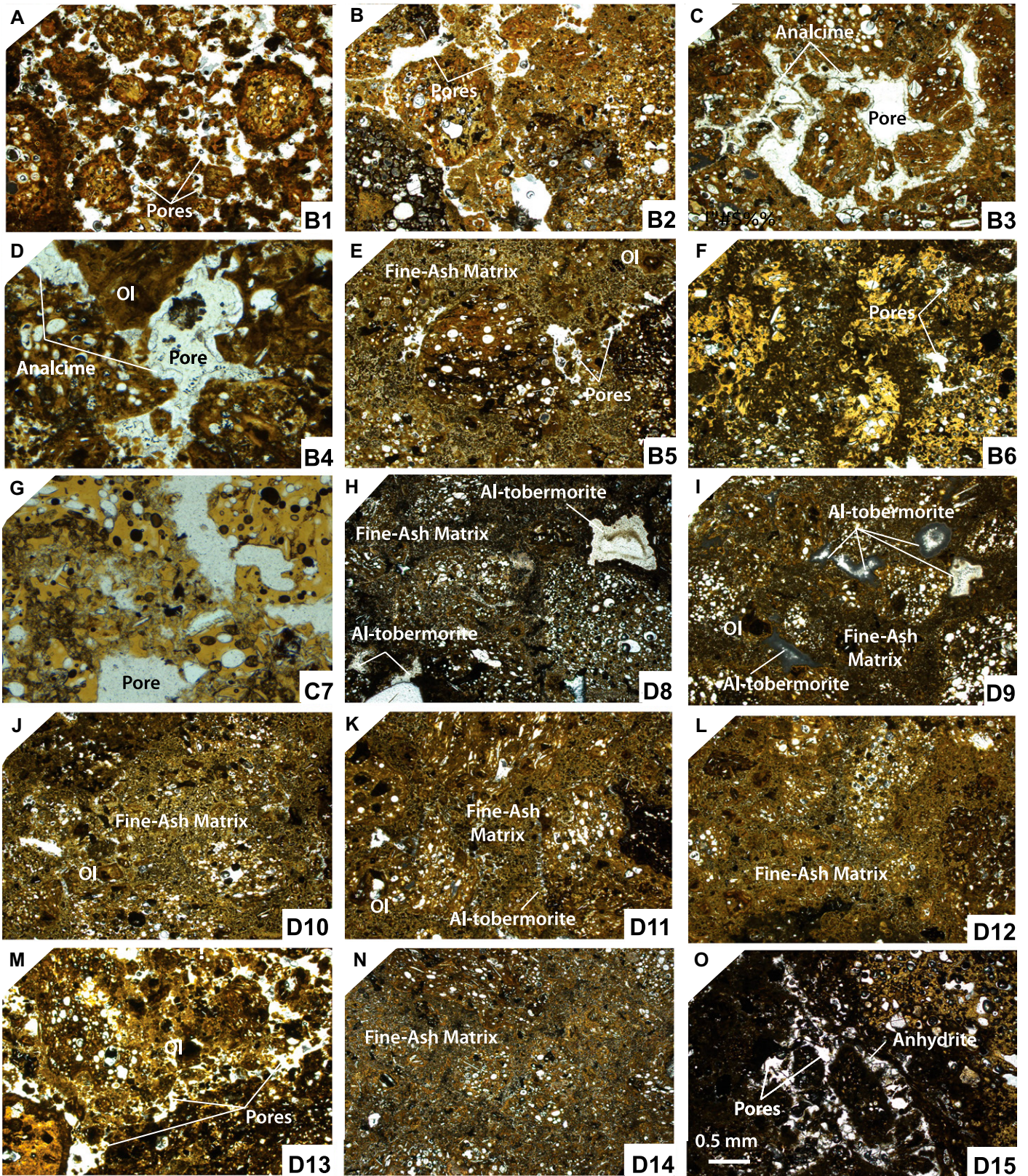
The XRPD scattering contribution of the amorphous phase is a distinguishing feature of the C7 and B6 diffraction patterns, where the background line results in a wide bump in the 15–45° 2 $\theta$  range, similar to aluminosilicate glasses (Fig. S3). In crystalline solids, unit cells repeat through translational symmetry, producing atomic order over long ranges. By contrast, amorphous materials are characterized by an atomic arrangement that lacks long-range periodicity (Kaduk et al., 2021). Transitionally amorphous and crystalline materials contain crystalline domains on the scale of nanometers;

these nanocrystalline materials have many complex features (Caraballo et al., 2015; Smith and Horgan, 2021). Distinctions among amorphous, nanocrystalline, and fully crystalline materials have important implications for gaining new insights into the complex materials typically described as sideromelane and palagonite (Stroncik and Schmincke, 2002).

This fine-scale progression of basaltic glass alteration is shown by synchrotron  $\mu$ XRD and  $\mu$ XRF analyses across a weakly altered pyroclast at 144.6 m.b.s. (zone 4; Fig. 5). Debye diffraction diagrams and plots of *d*-spacing intensity (Figs. 5A and 5B) indicate fresh glass (site #178), transitionally nanocrystalline clay mineral with a faint 1.53 Å reflection (#176), and further nanocrystalline clay mineral reflections at 2.63 Å and 4.64 Å (#174, #172, and #171). In the #172 and #171 analyses, short, faint arcs of pinpoint reflections at 1.49 Å, 1.99–2.03 Å, 2.11 Å, 2.45 Å, and 2.56 Å may be associated with incipient clinocllore, a chlorite group mineral. The absence of (001) interlayer reflections indicates a lack of long-range order. The broadly diffuse and continuous reflections contrast with spotty reflections associated with crystals of plagioclase, olivine, and calcite (#171).

Transects of  $\mu$ XRD analyses across the pyroclast, #167–#180, and its perimeter, #21–#34, further reveal transitions from fresh glass to nanocrystalline clay mineral, especially in the ash matrix (#23–#34; Figs. 5D and 5E). The transitions appear similar to diffuse, micrometer-scale domains that surround fine ash in C7 (Figs. 6A and 6B). Although the altered glass retains a translucent, yellowish gray (5Y 7/2) color in PPL, it no longer represents sideromelane, which is defined as fresh basaltic glass (e.g., Stroncik and Schmincke, 2002). The Debye diffraction diagrams suggest that nanocrystalline clay minerals with nonideal patterns contribute to the X-ray amorphous component of the QPA-XRPD analysis, which is defined here as materials lacking the long-range order of crystalline materials. The  $\mu$ XRD analyses indicate that micrometer-scale domains contain diverse phases and that nanocrystalline materials contributed to diagenesis and lithification (Smith and Horgan, 2021).





### Mineral Cements in Lapilli Tuff

Complex relationships exist among mineral cements, principally zeolites and Al-tober-

morite, in the pores of 1979 and 2017 drill core samples (Jakobsson and Moore, 1986; Jackson et al., 2019a; Prause et al., 2020, 2022; Mon-

tesano et al., 2023). The C7 tephra has large pores, >50  $\mu\text{m}$ , and little cohesion (Figs. 6A and 6B). In contrast, the strongly lithified D12



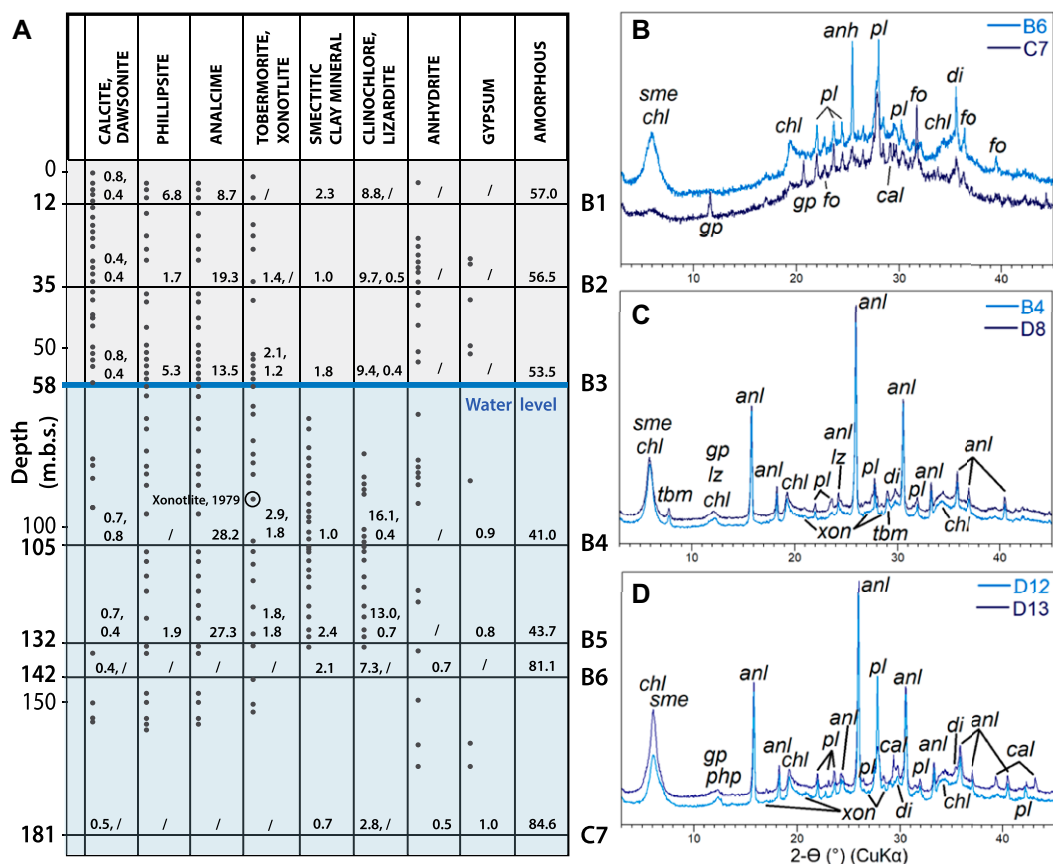


**Figure 4.** Authigenic and secondary mineral assemblages of Surtur pyroclastic basalt. (A) Hydrothermal minerals identified in the 1979 SE-01 drill core through optical microscopy, scanning electron microscope imaging, X-ray powder diffraction, and electron microprobe analysis (after Jakobsson and Moore, 1986, their fig. 6), and compared with quantitative phase analysis of X-ray powder diffraction data employing the Rietveld method for 2017 SE-02A and SE-02B samples (Table 1; Supplemental Text S2 [see text footnote 1]). Diffraction patterns: (B) weakly consolidated submarine tephra, C7, and lapilli tuff, B6; (C) well-lithified submarine lapilli tuff, B4 and D8; (D) seafloor lapilli tuff, D12 and D13. Mineral abbreviations (Warr, 2021): anh—*anhydrite*; anl—*analcime*; cal—*calcite*; chl—*clinchlore*; di—*diopside*; fo—*olivine*; gy—*gypsum*; lz—*lizardite*; pl—*plagioclase*; sme—*smectitic clay mineral*; tbm—*Al-tobermorite*; xon—*xonotlite*.

lapilli tuff has very fine ash packed among fine-ash shards; pores within fine-ash domains are  $<5\ \mu\text{m}$  in diameter (Figs. 6C and 6D). Conversely, the binding matrix of the B5 lapilli tuff and its 1979 precursor, 79S-134, at 134 m.b.s., contains ash shards surrounded by pores rimmed with mineral cements (Figs. 6E and 6F). In 1979, the pore openings averaged  $\sim 50\ \mu\text{m}$ . In 2017, they had decreased to  $\sim 10\text{--}15\ \mu\text{m}$ ; larger pores,  $> 350\ \mu\text{m}$ , have rims of mineral cements (Figs. 6G and 6H). Other lapilli tuff fabrics, D13 and D15, have a predominance of coarse, vesicular pyroclasts surrounded by connected pores (Figs. 3M and 3O). Similar fabrics are shown by X-ray  $\mu$ -computed tomography reconstructions of reference samples RS24, 212.0 m.b.s., and RS26, 228.6 m.b.s. (Figs. 6I and 6J). The compact fabric of RS27, at 235.1 m.b.s., more closely resembles that of sample D12 (Fig. 6K; Kahl et al., 2021b).

Unpublished 1980 SEM-SE images from the submarine SE-01 core samples show precipitation and subsequent dissolution of zeolites, phillipsite (Fig. 7A), and analcime (Figs. 7B and 7C), and crystallization of Al-tobermorite (Figs. 7A–7D), an unusual layered calcium–aluminum–sili-

cate–hydrate mineral that is the principal crystalline cementing phase in ancient Roman marine concrete (Jackson et al., 2017). The  $\mu\text{XRD}$  and  $\mu\text{XRF}$  investigations of the 2017 submarine B4 and D8 samples at 105.0 m.b.s. and 89.5 m.b.s. further describe these diverging reaction pathways (Figs. 7E, 7F, and 8). B4 has matrix pores  $\geq 2\ \text{mm}$  in diameter (Fig. 3D), with prominent analcime selvages of up to  $150\ \mu\text{m}$ . Fine sprays of Al-tobermorite crystals protrude from the analcime into the pore space (Figs. 8A and 8B). SEM-EDS maps (Fig. 8C) reveal elevated Na, Si, and Al at the exterior pore surface, and elevated Ca and Si in the interior. The  $\mu\text{XRD}$  analyses (Fig. 8D) show a broad  $14.10\ \text{\AA}$  reflection of nanocrystalline clay mineral in the altered glass of neighboring pyroclasts (#82), strong analcime reflections along the surfaces of the matrix pore (#44, #72, #190, and #242), and traces of Al-tobermorite that protrude from analcime (#44).

D8 has matrix pores mainly  $\leq 2\ \text{mm}$  in diameter (Fig. 3H). Al-tobermorite crystals of  $\leq 100\ \mu\text{m}$  formed on pore surfaces and within vesicles in pyroclasts (Figs. 8F and 8G). SEM-EDS maps of typical pores (Fig. 8H) show elevated concentrations of Ca and Si, and lesser Al, while  $\mu\text{XRD}$

analyses identify Al-tobermorite with  $11.21\ \text{\AA}$  interlayer spacing (Fig. 8J). A broad reflection of nanocrystalline clay mineral at  $13.53\ \text{\AA}$  derives from altered fine ash in the pore (Figs. 8I and 8J). Analcime occurs mainly in vesicular pyroclasts (Fig. 7F, site 4).

The 1980 SEM-SE images at 63.1 m.b.s. and 88.1 m.b.s. also show Al-tobermorite crystals extending from partially dissolved analcime crystals (Figs. 7B and 7C). At 118.5 m.b.s., by contrast, Al-tobermorite crystals protrude from the clay-rich surface of a vesicle in a pyroclast (Fig. 7D), similar to the 2017 D8 sample (Fig. 7F, site 3). Precipitation and dissolution of mineral cements, which record changing fluid compositions and partial closure of pore throats, were well established in 1979. Geochemical reaction path modeling using simulated temperatures, water pH, and elemental mobility for the Surtur system (Kleine et al., 2020) demonstrates that high pH—and thus, low water-rock ratios—favor the formation of Al-tobermorite over analcime. Limiting access to seawater inflow and/or decreasing permeability through in situ mineralization will ultimately favor crystallization of Al-tobermorite.



TABLE 1. MINERAL ASSEMBLAGES AND AMORPHOUS COMPONENTS FOR SURTUFF BASALTIC LAPILLI TUFF AND SEAFLOOR VOLCANICLASTIC SEDIMENTARY ROCK DETERMINED THROUGH X-RAY POWDER DIFFRACTION QUANTITATIVE PHASE ANALYSIS (XRPD-QPA)

SUSTAIN core segment sample	B1	B2	B3	SE-02A borehole		B4	B5	B6	SE-02B borehole		C7	D8	D9	D10	D11	SE-03 borehole		D12	D13	D14	D15	Tuff cone
	B1-1a	B2-1a	B3-1b	B4-1b	B5-3a	B6-1a	B5-3a	B6-1a	Fragment	D8-2a	D9-1a	D10-1a	D11-2b	D12-2a	D13-1b	D14-2a	D15-2a	D12-2a	D13-1b	D14-2a	D15-2a	S8T-1
Subcore sample	12.2	35.0	57.6	105.0	137.1	141.8	137.1	141.8	181.3	89.5	109.1	145.6	178.9	196.0	198.0	271.0	281.9	196.0	198.0	271.0	281.9	Seafl oor lithic bomb
Depth (m.b.s.)										(109.3)	(133.2)	(177.8)	(217.9)	(239.4)	(241.4)	(330.8)	(343.2)	(239.4)	(241.4)	(330.8)	(343.2)	Seafl oor lithic bomb
SE-03 borehole depth (m)																						
Temperature 1960 (°C)*	96	100	102	141	109	85	109	85	40	125	137	120	86	67	64	57	57	67	64	57	57	
Temperature 2017, 2018 (°C)†§	15	36	87	124	105	93	105	93	44	125	137	120	86	67	64	57	57	67	64	57	57	
Crystalline phases (wt%)																						
<i>Volcanic silicates</i>																						
Plagioclase (pl)	8.5(0.3)	6.0(0.2)	5.9(0.2)	3.9(0.5)	3.2(0.5)	5.5(0.2)	3.2(0.5)	5.5(0.2)	7.0(0.2)	5.8(0.2)	7.5(0.2)	5.3(0.2)	6.8(0.2)	8.0(0.4)	9.1(0.4)	11.2(0.3)	8.6(0.2)	8.0(0.4)	9.1(0.4)	11.2(0.3)	8.6(0.2)	18.4(0.3)
Dioptside (di)	2.7(0.3)	1.1(0.1)	1.9(0.1)	2.3(0.1)	2.4(0.1)	0.8(0.1)	2.4(0.1)	0.8(0.1)	1.1(0.1)	2.6(0.1)	2.7(0.1)	2.8(0.1)	3.6(0.1)	3.1(0.1)	3.3(0.2)	2.9(0.2)	2.7(0.1)	3.1(0.1)	3.3(0.2)	2.9(0.2)	2.7(0.1)	9.2(0.1)
Dorsterite (fo)	2.8(0.1)	1.7(0.1)	2.9(0.1)	b.d.l.	b.d.l.	2.0(0.1)	b.d.l.	2.0(0.1)	1.8(0.1)	b.d.l.	b.d.l.	b.d.l.	0.4(0.1)	b.d.l.	0.4(0.1)	b.d.l.	b.d.l.	b.d.l.	0.4(0.1)	b.d.l.	b.d.l.	1.6(0.1)
<i>Authigenic zeolites</i>																						
Analcime (anl)	8.7(0.2)	19.3(0.2)	13.5(0.3)	28.2(0.3)	27.3(0.3)	n.d.	n.d.	n.d.	n.d.	25.5(0.3)	24.8(0.3)	28.1(0.3)	26.9(0.3)	24.9(0.3)	24.9(0.4)	23.9(0.3)	26.0(0.3)	24.9(0.3)	24.9(0.4)	23.9(0.3)	26.0(0.3)	0.8(0.1)
Phillipsite (php)	6.8(0.2)	1.7(0.1)	5.3(0.2)	b.d.l.	1.9(0.1)	n.d.	n.d.	n.d.	n.d.	1.5(0.1)	1.0(0.2)	1.4(0.2)	1.0(0.2)	1.4(0.2)	1.8(0.2)	1.3(0.2)	2.0(0.2)	1.4(0.2)	1.8(0.2)	1.3(0.2)	2.0(0.2)	1.5(0.1)
<i>Calcium silicate hydrates</i>																						
Al: tobermorite (tbm)	n.d.	1.4(0.1)	2.1(0.1)	2.9(0.1)	1.8(0.1)	n.d.	n.d.	n.d.	n.d.	2.6(0.1)	2.6(0.1)	0.6(0.1)	1.4(0.1)	b.d.l.	b.d.l.	0.3(0.1)	b.d.l.	b.d.l.	b.d.l.	0.3(0.1)	b.d.l.	b.d.l.
Xonolite (xon)	n.d.	n.d.	1.2(0.1)	1.8(0.1)	1.8(0.0)	n.d.	n.d.	n.d.	0.5(0.1)	1.6(0.1)	1.8(0.1)	2.6(0.1)	1.7(0.1)	1.9(0.2)	0.9(0.1)	0.9(0.1)	1.0(0.1)	1.9(0.2)	0.9(0.1)	0.9(0.1)	1.0(0.1)	0.5(0.1)
<i>Serpentine group</i>																						
Lizardite (lz)	b.d.l.	0.5(0.1)	0.4(0.1)	0.4(0.1)	0.7(0.1)	n.d.	n.d.	n.d.	n.d.	0.6(0.1)	0.8(0.1)	0.9(0.1)	0.5(0.1)	0.7(0.1)	0.8(0.1)	0.9(0.1)	1.1(0.1)	0.7(0.1)	0.8(0.1)	0.9(0.1)	1.1(0.1)	0.5(0.1)
<i>Sulfides</i>																						
Anhydrite (anh)	n.d.	n.d.	n.d.	n.d.	n.d.	0.7(0.1)	n.d.	0.7(0.1)	0.5(0.1)	n.d.	n.d.	n.d.	n.d.	n.d.	n.d.	n.d.	n.d.	n.d.	n.d.	n.d.	n.d.	n.d.
Gypsum (gp)	n.d.	n.d.	n.d.	0.9(0.1)	0.8(0.1)	n.d.	0.8(0.1)	n.d.	1.0(0.1)	0.7(0.1)	0.8(0.1)	1.1(0.1)	0.9(0.1)	2.0(0.2)	1.9(0.2)	1.7(0.2)	0.8(0.2)	2.0(0.2)	1.9(0.2)	1.7(0.2)	0.8(0.2)	0.6(0.1)
<i>Carbonates</i>																						
Calcite (cal)	0.8(0.1)	0.4(0.1)	0.8(0.1)	0.7(0.1)	0.7(0.1)	0.4(0.1)	0.7(0.1)	0.4(0.1)	0.5(0.1)	0.6(0.1)	0.9(0.1)	0.8(0.1)	3.4(0.1)	0.8(0.1)	3.7(0.1)	0.9(0.1)	4.2(0.1)	0.8(0.1)	3.7(0.1)	0.9(0.1)	4.2(0.1)	0.7(0.1)
Dawsonite (dws)	0.4(0.1)	0.4(0.1)	0.4(0.1)	0.8(0.1)	0.4(0.1)	n.d.	n.d.	n.d.	n.d.	0.6(0.1)	0.6(0.1)	0.3(0.1)	b.d.l.	0.6(0.1)	0.4(0.1)	0.3(0.1)	0.3(0.1)	0.6(0.1)	0.4(0.1)	0.3(0.1)	0.3(0.1)	b.d.l.
<i>Oxide and Hydroxides</i>																						
Quartz (qz)	n.d.	n.d.	n.d.	n.d.	n.d.	n.d.	n.d.	n.d.	n.d.	n.d.	n.d.	n.d.	n.d.	n.d.	n.d.	n.d.	n.d.	n.d.	n.d.	n.d.	n.d.	n.d.
Hematite (hem)	0.5(0.1)	n.d.	n.d.	n.d.	n.d.	n.d.	n.d.	n.d.	n.d.	n.d.	n.d.	n.d.	n.d.	n.d.	n.d.	n.d.	n.d.	n.d.	n.d.	n.d.	n.d.	n.d.
Goethite (gth)	0.7(0.1)	0.3(0.1)	0.9(0.1)	n.d.	n.d.	n.d.	n.d.	n.d.	n.d.	n.d.	n.d.	n.d.	n.d.	n.d.	n.d.	n.d.	n.d.	n.d.	n.d.	n.d.	n.d.	n.d.
<i>Clay minerals</i>																						
Chlorite grp. (chl)	8.8(0.9)	9.7(0.9)	9.4(0.8)	16.1(1.5)	13.0(1.3)	7.3(0.3)	14.8(1.4)	14.9(1.7)	2.8(0.2)	14.8(1.4)	14.9(1.7)	15.0(1.5)	14.4(1.5)	16.7(1.9)	14.2(1.9)	18.1(1.7)	15.7(1.9)	16.7(1.9)	14.2(1.9)	18.1(1.7)	15.7(1.9)	5.8(0.3)
Smectite grp. (sme)	2.3(0.2)	1.0(0.1)	1.8(0.2)	1.0(0.3)	2.4(0.2)	2.1(0.2)	1.2(0.3)	3.0(0.2)	0.7(0.1)	1.2(0.3)	3.0(0.2)	1.2(0.3)	1.1(0.3)	b.d.l.	2.2(0.2)	1.6(0.2)	1.8(0.2)	b.d.l.	2.2(0.2)	1.6(0.2)	1.8(0.2)	3.0(0.2)
Amorphous phase (wt%)	57.0(1.2)	56.5(1.0)	53.5(0.8)	41.0(0.4)	43.7(1.6)	81.1(0.4)	42.0(1.5)	38.5(1.8)	84.6(0.4)	42.0(1.5)	38.5(1.8)	40.0(1.7)	36.1(1.6)	40.0(1.9)	36.0(1.9)	36.0(1.8)	35.0(1.8)	40.0(1.9)	36.0(1.9)	36.0(1.8)	35.0(1.8)	57.4(0.8)
XRD-QPA Sum (wt%)	100.0	100.0	100.0	100.0	100.0	100.0	100.0	100.0	100.0	100.0	100.0	100.0	100.0	100.0	100.0	100.0	100.0	100.0	100.0	100.0	100.0	100.0
R <sub>wpp</sub>	5.56	5.34	5.86	6.72	6.52	4.19	6.15	6.36	3.74	6.15	6.36	6.53	6.3	6.81	7.47	6.88	5.77	6.81	7.47	6.88	5.77	5.85
Mineral cements <sup>#</sup>	16.7	23.2	23.3	35.3	34.7	1.1	33.1	32.5	2.5	33.1	32.5	34.8	35.4	31.6	33.8	29.3	35.1	31.6	33.8	29.3	35.1	4.1
Clay minerals	11.1	10.7	11.2	17.1	15.4	9.4	16	17.9	3.5	16	17.9	16.2	15.5	16.7	16.4	19.7	17.5	16.7	16.4	19.7	17.5	8.8

Note: Amorphous phases include fresh volcanic glass and incipient mineral phases lacking long-range order. b.d.l.—below detection limit (<0.1 wt%); grp.—group; m.b.s.—meters below surface; n.d.—not detected; SUSTAIN—Surtsey Underwater Volcanic System for Thermophiles, Alteration Processes and Innovative Concretes drilling project; R<sub>wpp</sub>—R-weighted pattern, criterion of fit resulting from the Rietveld refinement, Toby (2006), Equation S1 (see text footnote 1); Supplemental Data S2 (see text footnote 1). Mineral symbols are those approved by the International Mineralogical Association (IMA) Commission on New Minerals, Nomenclature and Classification (CNMNC), Warr (2021). See Figures 4, S3, and S4; Table S1 (see text footnote 1).

\*Jakobsson and Moore (1986).

†SE-02A, SE-02B borehole temperatures (Jackson et al., 2019b).

‡SE-03 borehole temperatures (Weisenberger et al., 2021). Vertical depths below surface shown in italics.

#Zeolites, calcium silicate hydrates, sulfates, carbonates.

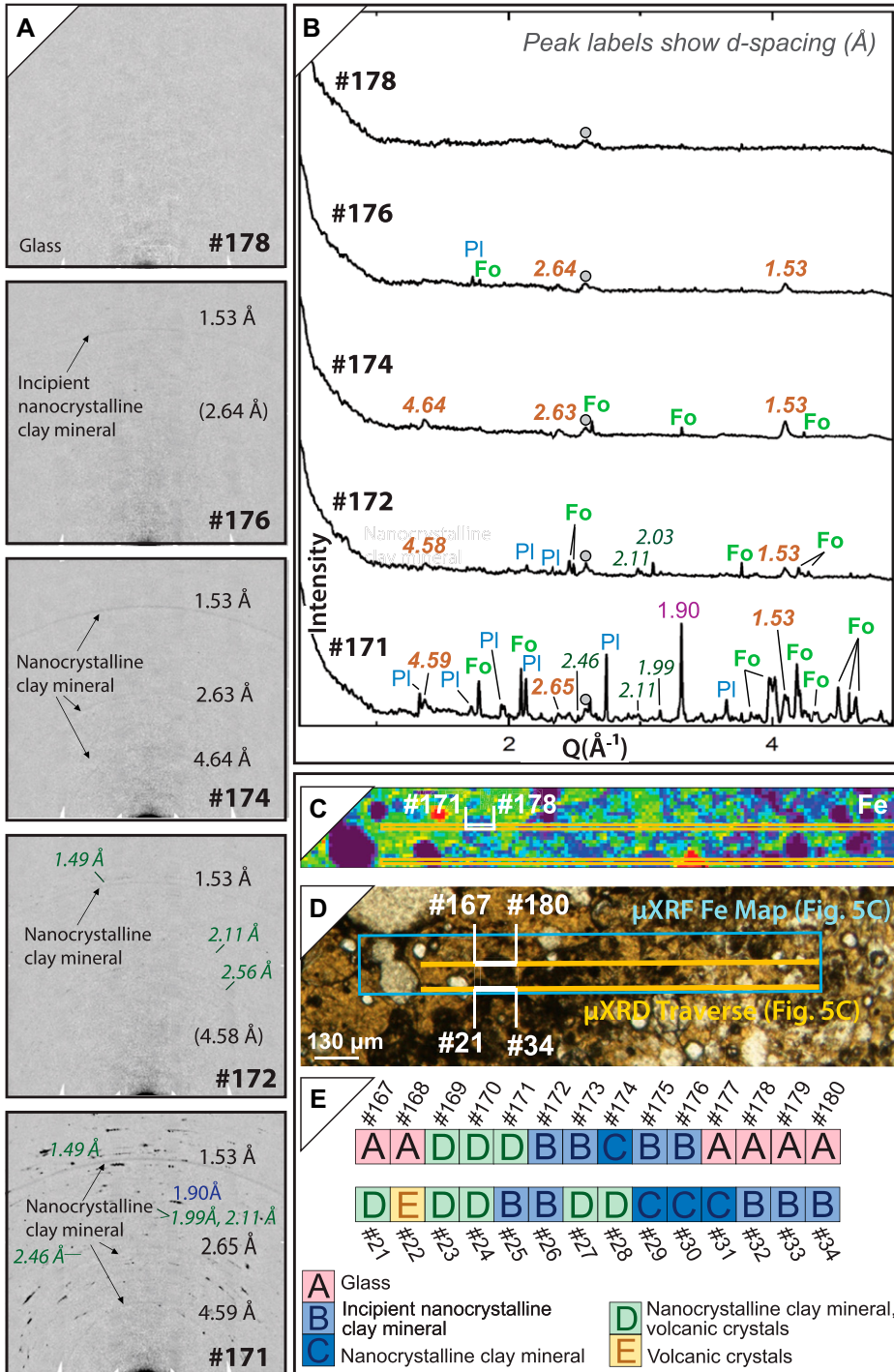


**Figure 5. Alteration of basaltic glass described with micro X-ray diffraction (μXRD) and micro X-ray fluorescence spectrometry (μXRF) analyses in weakly consolidated tuff at 144.6 m below surface (m.b.s.), submarine inflow zone, 4. (A) Debye diffraction diagrams in a glassy pyroclast (shown in part D) show the transition from fresh basaltic glass (#178) to weak reflections of nanocrystalline clay mineral (#176, #174, #172, and #171, gray labels, Å) and incipient clinocllore (#172 and #171, green labels, Å), 2–3 μm spot size. No interlayer d-spacings reflections are detected, indicating a lack of longer range-order in clay mineral structures. (B) Intensity versus Q (Å<sup>-1</sup>) for the #178–#171 μXRD analyses. Brown—nanocrystalline clay mineral; dark green—clinocllore; violet—calcite. Gray circles denote a flaw on the detector. Mineral abbreviations (Warr, 2021): fo—olivine; pl—plagioclase. (C) Qualitative Fe μXRF map (red indicates highest concentrations) shows the two μXRD transects and analyses. (D) Petrographic image, taken in plane-polarized light, shows the μXRD transects and area of the μXRF map. (E) Fresh glass and authigenic phases in the transect across the pyroclast (#167–#180) and its perimeter with the ash matrix (#21–#34).**

4 has lower Na<sub>2</sub>O + K<sub>2</sub>O and SiO<sub>2</sub> than the well-lithified submarine and subseafloor lapilli tuff (zones 3, 5, 6, and 7).

**Physical Characteristics**

**Subaerial Tuff Cone (0–56 m.b.s.; Zone 1)**

The B1 (12.2 m.b.s.) and B2 (35.0 m.b.s.) core segments are light grayish orange (10YR 6/4), moderately well-consolidated lapilli tuff, which comprises the dominant lithofacies of the subaerial tuff cone (Lorenz, 1974; McPhie et al., 2020; Figs. 1, 2, and S2). Abundant armored lapilli, formed of weakly altered light olive-brown to moderate yellow (5Y 5/6–5Y 6/6) altered glass and dark gray tachylite (N3) pyroclasts, have thin (<10 μm) zeolitic surface coatings (Figs. 3A and 3B). Vesicular pyroclasts are surrounded by broadly connected open space in B1 (Fig. 3A). B2 has weakly consolidated fine-ash matrix; matrix pores 5–15 mm in diameter connect around larger clasts (Fig. 3B). The altered glass of the fine-ash matrix is not birefringent but is weakly birefringent in larger pyroclasts. XRPD identifies clinocllore and smectitic clay mineral (Fig. 4A; Table 1). The onset of a broad peak at ~1.53–1.54 Å suggests that the smectitic phase (here, termed smectite) is trioctahedral,

Overall, the pyroclastic deposits with measurable anhydrite and gypsum—B6, C7, and D15—have elevated SO<sub>3</sub> (Figs. 4A and 9; Tables 1 and 2). Lapilli tuff in the zone of tidal flux, B3, has low Na<sub>2</sub>O, perhaps resulting from leaching during early glass alteration. K<sub>2</sub>O is slightly higher in subaerial and submarine samples than in subseafloor samples. Recent studies of 1979 and 2017 drill core samples describe the leaching of

SiO<sub>2</sub>, Al<sub>2</sub>O<sub>3</sub>, MgO, CaO, Na<sub>2</sub>O, and K<sub>2</sub>O from glass during early palagonitic alteration. A subsequent uptake of these elements from the solution occurs during further maturation of mineralized phases, except for CaO, which shows little change, and Na<sub>2</sub>O, which continues to decrease (Prause et al., 2020, 2022). Indeed, a total alkali-silica (TAS) diagram (Le Bas et al., 1986; Fig. S6) shows that the lapilli tuff of zones 1, 2, and

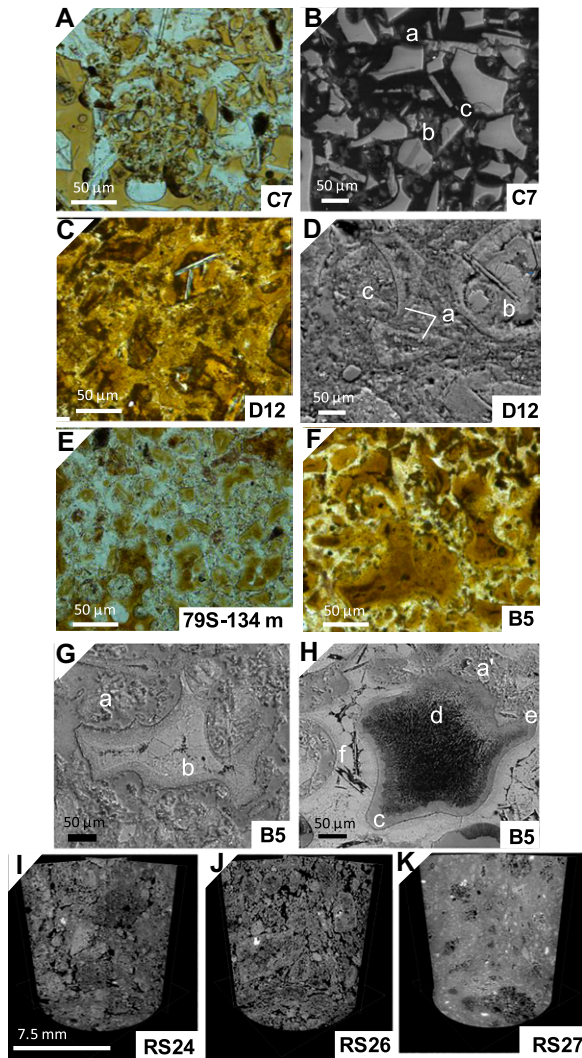


**Figure 6. Pore microstructures.** (A) C7, 181.3 m below surface (m.b.s.), image taken in plane-polarized light (PPL). (B) Scanning electron microscope-backscattered electron (SEM-BSE) image, C7, (a, b) diffuse perimeters of weakly altered glass shards, and (c) anhydrite. (C) D12, 198.0 m.b.s., PPL. Pore space that is empty in C7 contains very fine ash. (D) SEM-BSE image, D12, (a) altered glass shards, (b) dissolved plagioclase lath surrounded by acicular Al-tobermorite and xonotlite, and (c) binding matrix with subspherical pores, mainly  $<1\text{--}5\ \mu\text{m}$ . (E and F) Comparison of fine-ash matrix in archival 1979 thin section, 79S-134, 134 m.b.s., and 2017 thin section, B5, 137.1 m.b.s., PPL. Pore openings average  $50\ \mu\text{m}$  in 79S-134 and  $10\text{--}15\ \mu\text{m}$  in B5. (G and H) SEM-BSE images, B5, (a) pores in binding matrix, (b) altered glass pyroclast with an isotropic rim and birefringent interior, and matrix pore with (c) analcime, (d) Al-tobermorite, (e) closure of pore throat, and (f) dissolved plagioclase laths in a pyroclast. (I–K)  $\mu\text{CT}$ -derived image volumes show fabric components in SE-03 drill core reference samples RS24, 212.0 m.b.s.;

RS26, 228.6 m.b.s.; and RS27, 235.1 m.b.s. (after Kahl et al., 2021b). Reconstructed cylindrical shape ( $15\ \text{mm}$  in diameter and height) has  $7.5\ \mu\text{m}/\text{voxel}$  resolution. Highly attenuating phases (magnetite and olivine) are light gray values; areas of low X-ray absorption are dark gray (in situ mineralization) or black (voids, cracks).

with mainly divalent cations (e.g., Mg and Fe) at the octahedral site. Thus, the amorphous content, 56.5 wt%, mainly derives from weakly altered glass, which is mainly translucent in PPL. Analcime and phillipsite in B1 formed prior to drilling in 1979. More abundant analcime and phillipsite occur in B2; traces of Al-tobermorite fill vesicles in pyroclasts. Temperatures in the SE-01 borehole at the elevation of B1 decreased from  $96\ ^\circ\text{C}$  in 1980 to  $15\ ^\circ\text{C}$  in 2017 and, at B2, from  $100\ ^\circ\text{C}$  in 1980 to  $36\ ^\circ\text{C}$  in 2017 (Fig. 2B).

In the B1 and B2 subcores, connected porosity is 26%–38% (average of 35%) and 29%–43% (average of 37%), respectively (Figs. 10–13; Table 3). The bulk densities of B1 and B2 are low,  $1.55\text{--}1.78\ \text{g}\cdot\text{cm}^{-3}$  (average of  $1.60\ \text{g}\cdot\text{cm}^{-3}$ )

and  $1.43\text{--}1.71\ \text{g}\cdot\text{cm}^{-3}$  (average of  $1.55\ \text{g}\cdot\text{cm}^{-3}$ ). The total porosities are close to connected porosities; isolated porosities are 0.0%–3.9% and 0.0%–2.7%, respectively. Permeability is highly variable, ranging from  $2.69 \times 10^{-13}\ \text{m}^2$  to  $1.66 \times 10^{-12}\ \text{m}^2$  for B1, and from  $7.58 \times 10^{-17}\ \text{m}^2$  to  $7.30 \times 10^{-13}\ \text{m}^2$  for B2. P-wave velocity is  $1.59\text{--}2.99\ \text{km}\cdot\text{s}^{-1}$  in B1, and  $1.23\text{--}3.00\ \text{km}\cdot\text{s}^{-1}$  in B2. The average thermal conductivity, thermal diffusivity, and specific heat capacity of B1 are  $0.470\ \text{W}\cdot\text{m}^{-1}\cdot\text{K}^{-1}$ ,  $0.287\ \text{mm}^2\cdot\text{s}^{-1}$ , and  $1.048\ \text{kJ}\cdot\text{kg}^{-1}\cdot\text{K}^{-1}$ , respectively; for B2, averages are  $0.524\ \text{W}\cdot\text{m}^{-1}\cdot\text{K}^{-1}$ ,  $0.325\ \text{mm}^2\cdot\text{s}^{-1}$ , and  $1.107\ \text{kJ}\cdot\text{kg}^{-1}\cdot\text{K}^{-1}$ . The uniaxial compressive strength (UCS) of two B1 subcores is 13.7 MPa and 13.2 MPa and, for two B2 subcores, 9.5 MPa and 9.2

MPa. The calculated static Young's modulus is 3.8 GPa and 3.5 GPa, and 3.8 GPa and 3.2 GPa, respectively.

#### Tidal Flux Zone (56–65 m.b.s.; Zone 2)

Water level in the Surtur boreholes is affected by ocean tides that are attenuated and delayed relative to tides in the open ocean. The common tidal range between successive high and low tides is 5–10 cm (Moore et al., 1992). In 1979, mean water level in the SE-01 borehole was 61.9 m.b.s. By 1992, water level had risen  $\sim 0.5\ \text{m}$ , mainly due to subsidence of the island (Moore, 1982; Moore et al., 1992); the average groundwater level is always slightly above sea level. In 2017, tidal flux in the SE-02A borehole was centered at 58 m.b.s. (water level, Fig. 2A) (Jackson et al., 2019b; Weisenberger et al., 2019).

The B3 core segment (57.6 m.b.s.) is moderately well-lithified lapilli tuff, which is grayish olive (10Y 4/2) in overall color (Fig. S2). It has altered, olive gray (5Y 3/2), vesicular pyroclasts and common armored lapilli. The altered glass of the fine-ash matrix is not birefringent, but larger pyroclasts have thin isotropic rims and weakly birefringent interiors (Fig. 3C). Matrix pores, of up to 10 mm in diameter, have surface coatings of mineral cements, mainly analcime (and phillipsite); Al-tobermorite fills vesicles of pyroclasts. XRPD identifies analcime, 13.5 wt%; phillipsite, 5.3%; Al-tobermorite, 2.1 wt%; clinocllore, 9.4 wt%; and smectite, 1.8 wt%. The amorphous content, 53.5 wt%, likely derives from clay mineral without XRPD long-range order (Fig. 4A, Table 1). Borehole temperatures decreased from  $102\ ^\circ\text{C}$  to  $87\ ^\circ\text{C}$  from 1980 to 2017 (Fig. 2B).

For B3 subcores, connected porosity is high, 31%–39% (average of 33%; Figs. 10–13; Table 3), and bulk density is  $1.49\text{--}1.67\ \text{g}\cdot\text{cm}^{-3}$  (average of  $1.61\ \text{g}\cdot\text{cm}^{-3}$ ). The total and isolated porosities are 33.8%–40.9% and 0.0%–3.8%, respectively. Permeability ranges from  $9.91 \times 10^{-15}\ \text{m}^2$  to  $1.21 \times 10^{-12}\ \text{m}^2$  (although the permeability of  $1.21 \times 10^{-12}\ \text{m}^2$  in one subcore is anomalously high, and average permeability is  $\sim 10^{-14}\ \text{m}^2$ ). P-wave velocity is  $1.55\text{--}2.22\ \text{km}\cdot\text{s}^{-1}$ . The average thermal conductivity, thermal diffusivity, and specific heat capacity are  $0.538\ \text{W}\cdot\text{m}^{-1}\cdot\text{K}^{-1}$ ,  $0.317\ \text{mm}^2\cdot\text{s}^{-1}$ , and  $1.056\ \text{kJ}\cdot\text{kg}^{-1}\cdot\text{K}^{-1}$ , respectively. The UCS of two B3 subcores is 18.1 MPa and 21.8 MPa, and the calculated static Young's modulus is 3.8 GPa and 4.6 GPa, respectively.

#### Upper Submarine Lapilli Tuff (65–142 m.b.s.; Zone 3)

Well-lithified to very well-lithified lapilli tuff extends through the zone of submarine maximal temperatures at  $\sim 65\text{--}142\ \text{m.b.s.}$  in the vertical boreholes and  $\sim 65\text{--}160\ \text{m.b.s.}$  in the inclined



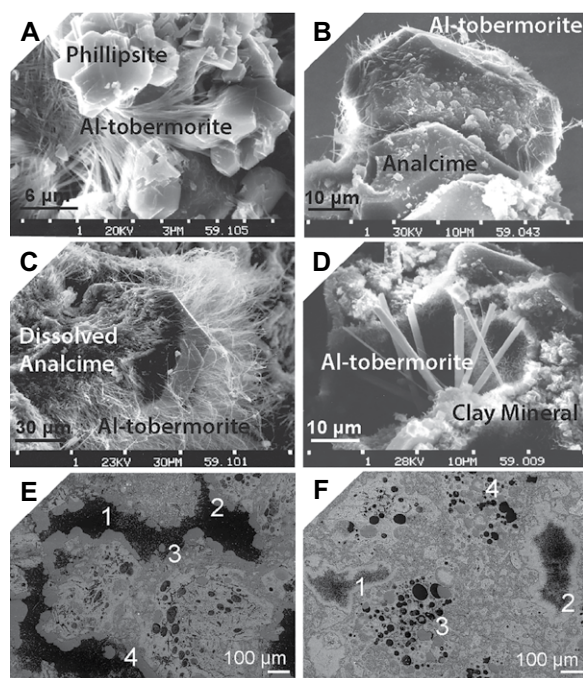


**Figure 7. Well-lithified submarine lapilli tuff. Scanning electron microscope–secondary electron (SEM-SE) images, 1980: (A) 11.1 m.b.s., near B1; (B) 63.1 m.b.s., near B3; (C) 88.1 m.b.s., above B4; (D) 118.5 m.b.s., above B5 (J.G. Moore, 2014, personal commun.). Scanning electron microscope–backscattered electron (SEM-BSE) images, 2017: (E) B4: sites 1–4, sprays of Al-tobermorite crystals protrude from analcime pore surface coatings; (F) D8: sites 1–3, Al-tobermorite pore surface coatings, and site 4, vesicle with analcime surface coating and subsequent Al-tobermorite.**

borehole (Figs. 1C and 2; Table 3). The B4 and B5 core segments, which are moderate olive-gray (5Y 5/2) overall, appear less compact than the D8 and D9 core segments, which are dark greenish gray (5GY 4/1) overall (Fig. S2). In B4 and B5, the altered glass of the fine-ash matrix is not birefringent, but larger pyroclasts have an isotropic rim and birefringent interior (Figs. 3D, 3E, 6F–6H, and 7E); B5 has intermittent zones of oriented birefringence. In D8 and D9, altered glass of the fine-ash matrix is not birefringent, except in clasts >100 μm in diameter. XRPD identifies similar abundances of mineral cements: 27–28 wt% analcime in B4 and B5; 25 wt% analcime in D8 and D9; phillipsite <1–2 wt%; Al-tobermorite <2–3 wt%; and xonotlite, a layered calcium–silicate–hydrate mineral with acicular morphology (Bernstein et al., 2009; Figs. 4A and 4C; Table 1). Xonotlite occurs in the 1979 core only at 125 m.b.s., where temperatures were  $\geq 141^\circ\text{C}$  (Jakobsson and Moore, 1986).

Clinochlore and smectite are detected throughout at 13–16 wt% and 1–3 wt%, respectively. The amorphous content (39–44 wt%) appears to be nanocrystalline clay mineral in altered glass with no XRPD long-range order, as indicated by  $\mu\text{XRD}$  and  $\mu\text{XRF}$  analyses at 88 m.b.s. and 138 m.b.s. in archival SE-01 lapilli tuff (Jackson et al., 2019a). Olivine is below detection limits, which indicates pervasive alteration to lizardite (Table 1). B4 (105.0 m.b.s.) occurs at the borehole temperature maximum,  $141^\circ\text{C}$  in 1980 and  $124^\circ\text{C}$  in 2017. At B5 (131.7 m.b.s.), temperatures were  $109^\circ\text{C}$  in 1980 and  $105^\circ\text{C}$  in 2017.

At D8 (89.5 vertical m.b.s.; 109.3 m measured depth) and D9 (109.1 vertical m.b.s.; 133.2 m measured depth), 2018 borehole temperatures (Weisenberger et al., 2021) were  $125^\circ\text{C}$  and  $137^\circ\text{C}$ , respectively (Figs. 2B and 2C).

The B4 and D8 subcores show pronounced differences (Figs. 2 and 10–13; Table 3). B4 subcores have high connected porosities, 31%–36% (average of 33%), and low bulk densities, averaging  $1.60\text{ g}\cdot\text{cm}^{-3}$ . The total and isolated porosities are 33.0%–37.9% and 1.8%–2.8%, respectively. Permeability ranges from  $2.17 \times 10^{-17}\text{ m}^2$  to  $9.23 \times 10^{-16}\text{ m}^2$ . P-wave velocity is  $2.71\text{--}2.95\text{ km}\cdot\text{s}^{-1}$ . The average thermal conductivity, thermal diffusivity, and specific heat capacity are  $0.589\text{ W}\cdot\text{m}^{-1}\cdot\text{K}^{-1}$ ,  $0.363\text{ mm}^2\cdot\text{s}^{-1}$ , and  $1.024\text{ kJ}\cdot\text{kg}^{-1}\cdot\text{K}^{-1}$ , respectively. The UCS of two subcores is 5.6 MPa and 19.8 MPa; the calculated static Young's modulus is 5.6 GPa and 5.6 GPa, respectively. In contrast, the connected porosity of D8 subcores is 27%–31% (average of 28%), lower than that of B4; the total and isolated porosities are 27.1%–31.4% and 0.0%–4.2%, respectively. The average bulk density is  $1.79\text{ g}\cdot\text{cm}^{-3}$ . Permeability,  $7.31 \times 10^{-19}\text{ m}^2$  to  $2.34 \times 10^{-17}\text{ m}^2$ , is nearly two orders of magnitude lower than that of B4. P-wave velocity is  $3.12\text{--}3.56\text{ km}\cdot\text{s}^{-1}$ . The average thermal conductivity, thermal diffusivity, and specific heat capacity of D8 are  $0.719\text{ W}\cdot\text{m}^{-1}\cdot\text{K}^{-1}$ ,  $0.383\text{ mm}^2\cdot\text{s}^{-1}$ , and  $1.052\text{ kJ}\cdot\text{kg}^{-1}\cdot\text{K}^{-1}$ , respectively. The UCS of two subcores is 42.6 MPa and 35.7 MPa, and the calculated static Young's modulus is 10.9 GPa, respectively. These are substantially higher values than those of the B4 subcores.

The B5 and D9 core segments show less variability. The connected porosity for B5 is 28%–32% (average of 30%), and for D9, 28%–34% (average of 32%; Figs. 10–13). The bulk density is  $1.70\text{--}1.77\text{ g}\cdot\text{cm}^{-3}$  (average of  $1.74\text{ g}\cdot\text{cm}^{-3}$ ) and  $1.59\text{--}1.75\text{ g}\cdot\text{cm}^{-3}$  (average of  $1.67\text{ g}\cdot\text{cm}^{-3}$ ), respectively. The total and isolated porosities of B5 subcores are 30.6%–33.7% and 2.0%–2.8%, respectively; for D9 subcores, these are 31.5%–37.6% and 1.3%–3.8%. Permeability ranges from  $4.78 \times 10^{-17}\text{ m}^2$  to  $1.14 \times 10^{-16}\text{ m}^2$  for B5, and  $3.01 \times 10^{-18}\text{ m}^2$  to  $7.17 \times 10^{-16}\text{ m}^2$  for D9. P-wave velocity is  $2.60\text{--}3.11\text{ km}\cdot\text{s}^{-1}$  in B5, and  $2.56\text{--}3.27\text{ km}\cdot\text{s}^{-1}$  in D9. The average thermal conductivity, thermal diffusivity, and specific heat capacity are  $0.622\text{ W}\cdot\text{m}^{-1}\cdot\text{K}^{-1}$ ,  $0.357\text{ mm}^2\cdot\text{s}^{-1}$ , and  $1.016\text{ kJ}\cdot\text{kg}^{-1}\cdot\text{K}^{-1}$  for B5 and, for D9,  $0.624\text{ W}\cdot\text{m}^{-1}\cdot\text{K}^{-1}$ ,  $0.367\text{ mm}^2\cdot\text{s}^{-1}$ , and  $1.030\text{ kJ}\cdot\text{kg}^{-1}\cdot\text{K}^{-1}$ . The UCS of two B5 subcores is 17.6 MPa and 18.6 MPa; the UCS of two D9 subcores is higher, 28.9 MPa and 31.5 MPa. The calculated static Young's modulus for B5 subcores is 6.6 GPa and 6.8 GPa and, for D8 subcores, 7.4 GPa and 8.2 GPa.

#### **Submarine Inflow Zone (142–155 m.b.s.; Zone 4)**

Weakly consolidated tephra deposits encountered in the 1979 drill core at 140–143.8 m.b.s., 148.5–149.7 m.b.s., 157.4–168.6 m.b.s., and 170.5–180.6 m.b.s. were thought to channel the flow of cold seawater into the hydrothermal system (Jakobsson and Moore, 1982; Ólafsson and Jakobsson, 2009). A 2017 geophysical log confirms that cool water of high salinity enters the SE-02B borehole at 143–150 m.b.s. (Jackson et al., 2019b; Fig. 1). The B6 core segment (141.8 m.b.s.) is weakly-consolidated lapilli tuff, which is moderate olive-brown (5Y 3/4) overall (Fig. S2). Vesicular pyroclasts are bounded by pores that are  $\leq 15\text{ mm}$  in length. A moderate olive-brown (5Y 4/4) to olive-gray (5Y 3/2) matrix of fine-ash contains abundant pores >100 μm in diameter (Fig. 3F). Vesicular lapilli have yellow-gray (5Y 7/2), translucent interiors in PPL. There are no birefringent altered glass domains. XRPD detects no analcime, phillipsite, nor Al-tobermorite; amorphous content is high, 81.1 wt%, and mainly derived from apparently fresh glass (Figs. 4A, 4B, and S4; Table 1). Borehole temperatures were  $85^\circ\text{C}$  in 1980, and  $93^\circ\text{C}$  in 2017 (Figs. 2B and 2C).

For the B6 subcores, connected porosity is 40%–44% (average of 42%; Figs. 10–13; Table 3), and bulk density is  $1.50\text{--}1.58\text{ g}\cdot\text{cm}^{-3}$  (average of  $1.54\text{ g}\cdot\text{cm}^{-3}$ ). The total and isolated porosities are 42.2%–45.2% and 1.5%–2.4%, respectively. Permeability is the highest of all samples, at  $2.14 \times 10^{-13}\text{ m}^2$  to  $5.10 \times 10^{-13}\text{ m}^2$ . P-wave velocity is  $1.28\text{--}1.68\text{ km}\cdot\text{s}^{-1}$ . The average ther-



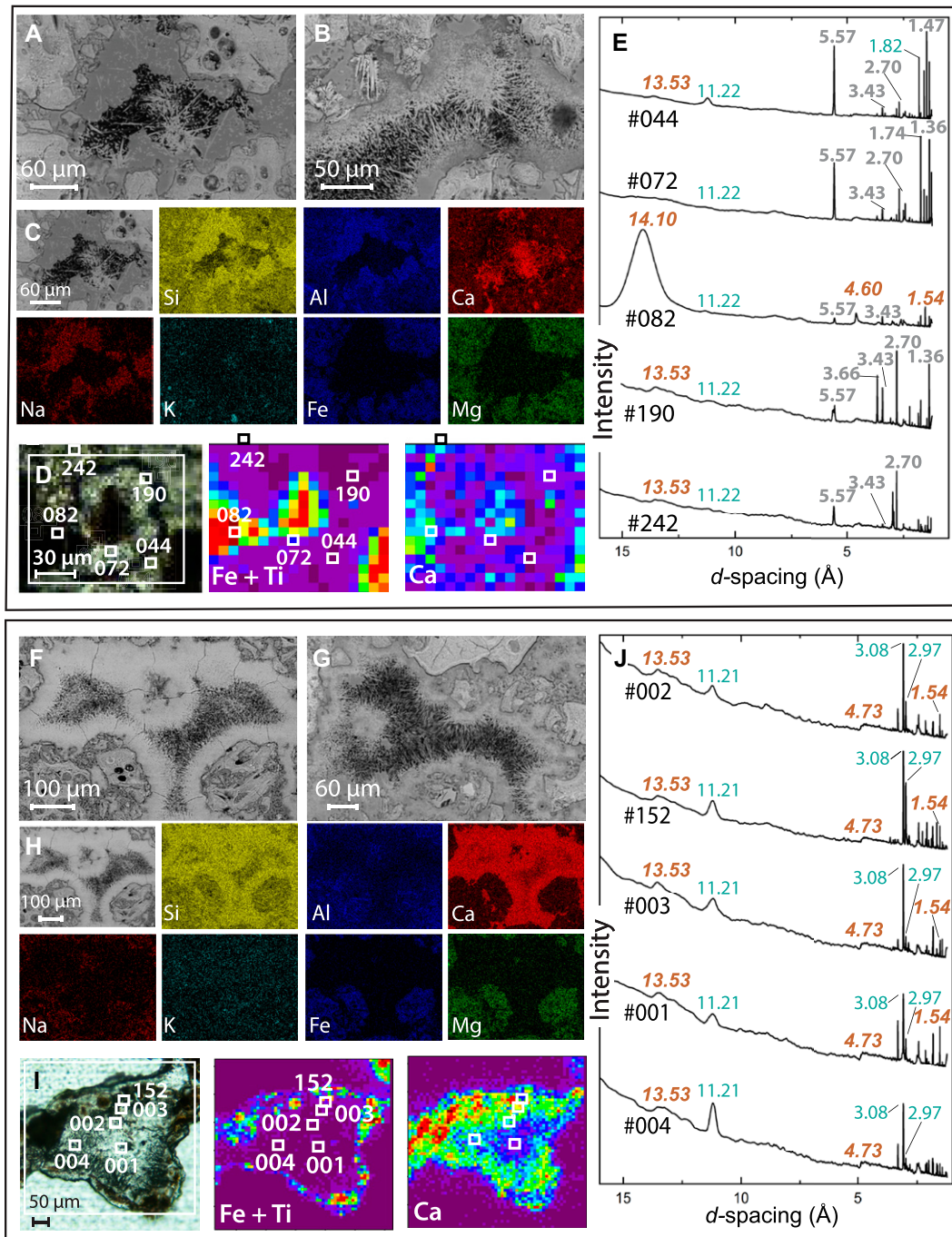


Figure 8. Mineral cements in matrix pores described with micro X-ray diffraction ( $\mu$ XRD) and micro X-ray fluorescence spectrometry ( $\mu$ XRF) analyses, indicating diverse reaction pathways: (A–E) B4, 105.0 m.b.s.; (F–J) D8, 89.5 m.b.s. (A, B, F, G) Scanning electron microscope–backscattered electron (SEM-BSE) images of pores. (C, H) Scanning electron microscopy–energy dispersive X-ray spectroscopy (SEM-EDS) maps of elemental concentrations. (D, I) Petrographic images and qualitative Fe + Ti and Ca  $\mu$ XRF maps showing sites of  $\mu$ XRD analyses. (E, J) Intensity versus  $d$ -spacing diffraction patterns; brown—nanocrystalline clay mineral; gray—analcime; blue—Al-tobermorite.

mal conductivity, thermal diffusivity, and specific heat capacity are  $0.472 \text{ W}\cdot\text{m}^{-1}\cdot\text{K}^{-1}$ ,  $0.351 \text{ mm}^2\cdot\text{s}^{-1}$ , and  $0.873 \text{ kJ}\cdot\text{kg}^{-1}\cdot\text{K}^{-1}$ , respectively. The measured UCS and calculated static Young's modulus of two subcores are 11.6 MPa and 9.9 MPa, and 2.0 GPa and 2.0 GPa, respectively.

#### Lower Submarine Tephra and Lapilli Tuff (145–186 m.b.s.; Zone 5)

**Vertical SE-02B borehole.** Very weakly consolidated tephra of the C7 core segment

(181.3 m.b.s.), which is brownish black (5YR 2/1) in overall color (Fig. S2), retain translucent, apparently fresh glass; there is no birefringence in the opaque, altered glass domains (Figs. 3G, 6A, and 6B). XRPD identifies high amorphous content, 84.2 wt%, and traces of anhydrite and gypsum (Figs. 4A and 4B; Table 1). Borehole temperatures measured in 2017 at 175 m.b.s.,  $44^\circ\text{C}$ , are similar to those measured at 181 m.b.s. in 1980,  $40^\circ\text{C}$  (Fig. 2B).

The connected porosity and permeability of C7 could not be measured; the sample disintegrated during subcore preparation. Using the dimensions of a section of the sample, the total porosity and bulk density were estimated to be 40.3% and  $1.66 \text{ g}\cdot\text{cm}^{-3}$ , respectively. Permeability,  $7.72 \times 10^{-14} \text{ m}^2$ , was estimated using a TinyPerm II field permeameter (Farquharson et al., 2015). Thermal properties were measured using two sections of the sample; the thermal conductivity, thermal diffusivity, and specific

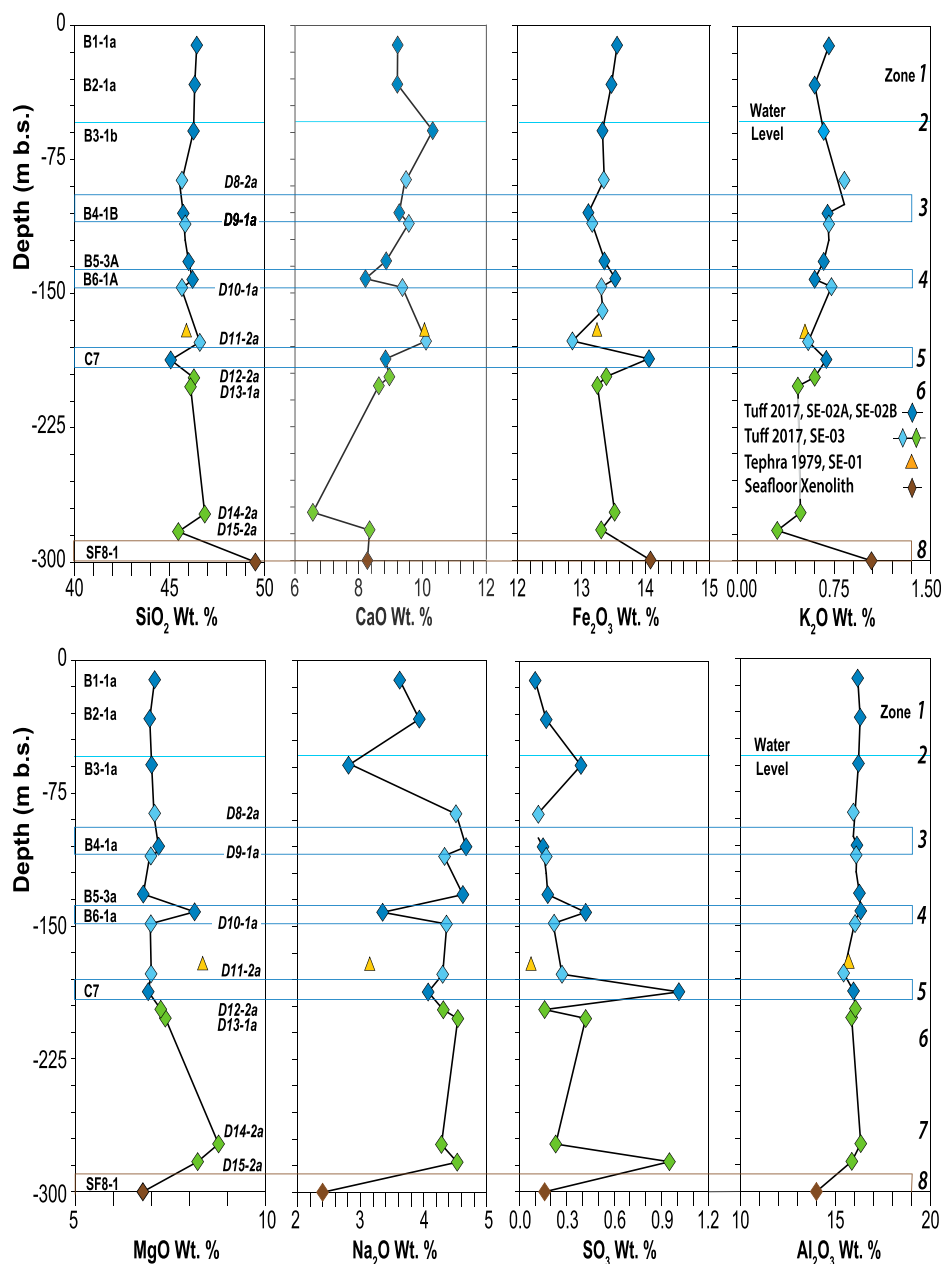


**Figure 9.** Whole-rock major-element compositions of powdered subcores (see Figs. 1C and 2A) determined through X-ray fluorescence analyses following Rhodes and Vollinger (2004; Tables 2 and S2 [see text footnote 1]).

heat capacity are  $0.547 \text{ W}\cdot\text{m}^{-1}\cdot\text{K}^{-1}$ ,  $0.529 \text{ mm}^2\cdot\text{s}^{-1}$ , and  $0.630 \text{ kJ}\cdot\text{kg}^{-1}\cdot\text{K}^{-1}$ , respectively.

**Inclined SE-03 borehole.** The very well-lithified, dark greenish gray (5GY 4/1) lapilli tuff of the D10 core segment (145.6 vertical m.b.s.; 177.8 m measured depth) and the D11 core segment (178.9 vertical m.b.s.; 217.9 m measured depth) occur within the lower submarine hydrothermal zone (Figs. 1 and 2), ~15–30 m above the inferred depth of the pre-eruption seafloor (Figs. 1C and 2A). Borehole temperatures in 2018 (Weisenberger et al., 2021)

were  $120 \text{ }^\circ\text{C}$  near D10, and  $86 \text{ }^\circ\text{C}$  near D11 (Figs. 2B and 2C).

The D10 and D11 subcores have compact fabrics. Abundant matrix, composed of angular tachylite shards and very fine ash, surrounds vesicular pyroclasts (Figs. 3J and 3K). The altered glass of the matrix is not birefringent except for clasts  $>300 \text{ }\mu\text{m}$  in size; larger pyroclasts have a birefringent interior with zones of oriented birefringence. Occasional voids of  $\leq 0.5 \text{ mm}$  are partially filled with mineral cements. XRPD identifies abundant analcime,

27–28 wt%; phillipsite, 1 wt%; Al-tobermorite, 1 wt%; and xonotlite, 2–3 wt% (Fig. 4A; Table 1). Clinochlore is detected at 14–15 wt% and smectite,  $<2 \text{ wt}\%$ ; the amorphous component, 36–40 wt%, appears to be clay mineral phases without long-range order. D11 also contains 2 wt% of quartz from xenolithic inclusions.

The D10 and D11 subcores have similar properties (Figs. 10–13; Table 3). The connected porosity is low, 23%–27% (average of 25%) and 22%–28% (average of 25%), respectively, and bulk density is high,  $1.80\text{--}1.89 \text{ g}\cdot\text{cm}^{-3}$  (average of  $1.85 \text{ g}\cdot\text{cm}^{-3}$ ) and  $1.86\text{--}2.00 \text{ g}\cdot\text{cm}^{-3}$  (average of  $1.94 \text{ g}\cdot\text{cm}^{-3}$ ; Figs. 10–13; Table 3). The total porosities are 26.0%–29.5% and 22.4%–28.0%, respectively, and the isolated porosities are 1.8%–5.3% and 0.0%–1.0%. The permeability ranges from  $4.45 \times 10^{-19} \text{ m}^2$  to  $4.15 \times 10^{-18} \text{ m}^2$  for the D10 subcores, the lowest in the entire sample suite; permeability is  $1.16 \times 10^{-18} \text{ m}^2$  to  $3.33 \times 10^{-17} \text{ m}^2$  for the D11 subcores. P-wave velocity is high,  $3.29\text{--}3.71 \text{ km}\cdot\text{s}^{-1}$  and  $3.36\text{--}3.51 \text{ km}\cdot\text{s}^{-1}$ , respectively. The average thermal conductivity, thermal diffusivity, and specific heat capacity are  $0.788 \text{ W}\cdot\text{m}^{-1}\cdot\text{K}^{-1}$ ,  $0.436 \text{ mm}^2\cdot\text{s}^{-1}$ , and  $0.986 \text{ kJ}\cdot\text{kg}^{-1}\cdot\text{K}^{-1}$  for D10, and  $0.814 \text{ W}\cdot\text{m}^{-1}\cdot\text{K}^{-1}$ ,  $0.446 \text{ mm}^2\cdot\text{s}^{-1}$ , and  $0.947 \text{ kJ}\cdot\text{kg}^{-1}\cdot\text{K}^{-1}$  for D11. The UCS for two D10 subcores is 51.9 MPa and 45.0 MPa, and, for a D11 subcore, 57.9 MPa. The static calculated Young's modulus is 13.0 GPa and 11.8 GPa for the D10 subcores, and 14.1 GPa for the D11 subcore.

#### **Uppermost Subseafloor Lapilli Tuff (195–205 m.b.s.; Zone 6)**

The dark greenish-gray (5GY 4/1) lapilli tuff of the D12 (196.0 vertical m.b.s.; 239.4 m measured depth) and D13 (198.0 vertical m.b.s.; 241.6 m measured depth) core segments occur just below the inferred pre-eruption seafloor (Figs. 1C and 2A). D12 is strongly lithified, with abundant very fine-ash matrix and cohesive interfacial zones along altered pyroclasts (Fig. 3L). By contrast, D13 is moderately well-consolidated, with abundant large, connected pores and narrow rims of fine ash on vesicular pyroclasts (Fig. 3M; Jackson, 2020). In D12, altered glass of the fine-ash matrix is not birefringent, yet larger pyroclasts have internal mottled birefringence and intermittent oriented birefringence. There is little fine-ash matrix in D13; the vesicles in larger pyroclasts have weakly birefringent rims. XRPD analyses (Figs. 4A and 4D; Table 1) identify analcime, 25 wt%; phillipsite and xonotlite,  $<2 \text{ wt}\%$ ; and traces of Al-tobermorite. Mineral cements comprise ~32–34 wt% of both samples. Clinochlore is identified at 14–17 wt%, yet smectite is mainly below detection limits; the amorphous content, 36–44 wt%, is clay mineral without long-range order. Bore-

TABLE 2. MAJOR-ELEMENT GEOCHEMISTRY FROM POWDERED SUBCORES FOR 2017 SURTUR BASALTIC LAPILLI TUFF AND SEAFLOOR VOLCANICLASTIC SEDIMENTARY ROCK

SUSTAIN core segment sample	B1	B2	B3	B4	B5	B6	C7	D8	D9	D10	D11	D12	D13	D14	D15	S8T
2017 SUSTAIN drill core	SE-02A borehole						SE-02B borehole	SE-03 borehole						Lithic bomb		
Subcore sample	B1-1a*	B2-1a	B3-1b	B4-1b	B5-3a	B6-1a	C7	D8-2a	D9-1a	D10-1a	D11-2b	D12-2a	D13-1b	D14-2a	D15-2a	S8T-1
Depth (m.b.s.)	12.2	35.0	57.6	105.0	131.7	141.8	181.3 <sup>†</sup>	89.5	109.1	145.6	178.9	196.0	198.0	271.0	281.3	
SE-03 borehole, measured depth (m)								(109.3)	(133.2)	(177.8)	(217.9)	(239.4)	(241.4)	(330.8)	(343.2)	
SiO <sub>2</sub> (wt%)	46.43	46.32	46.26	45.72	46.00	46.21	45.06	45.65	45.82	45.65	46.59	46.28	46.10	46.85	45.46	49.51
TiO <sub>2</sub> (wt%)	2.36	2.36	2.31	2.27	2.34	2.38	2.56	2.29	2.28	2.32	2.19	2.29	2.27	2.36	2.26	2.81
Al <sub>2</sub> O <sub>3</sub> (wt%)	16.17	16.30	16.21	16.13	16.26	16.33	15.95	15.94	16.09	16.03	15.43	16.05	15.85	16.33	15.86	14.00
Fe <sub>2</sub> O <sub>3</sub> (wt%)	13.56	13.47	13.33	13.11	13.36	13.53	14.05	13.35	13.17	13.33	12.86	13.39	13.25	13.52	13.31	14.08
MnO (wt%)	0.20	0.20	0.20	0.19	0.20	0.20	0.20	0.20	0.20	0.20	0.19	0.20	0.21	0.21	0.18	0.23
MgO (wt%)	7.09	6.96	7.01	7.19	6.79	8.14	6.92	7.09	6.99	6.99	7.00	7.25	7.37	8.77	8.22	6.78
CaO (wt%)	9.22	9.21	10.32	9.27	8.86	8.21	8.84	9.48	9.57	9.32	10.11	8.96	8.63	6.56	8.34	8.27
Na <sub>2</sub> O (wt%)	3.62	3.93	2.81	4.67	4.62	3.35	4.07	4.51	4.33	4.36	4.30	4.31	4.54	4.28	4.53	2.40
K <sub>2</sub> O (wt%)	0.71	0.60	0.67	0.70	0.67	0.60	0.69	0.83	0.71	0.73	0.55	0.60	0.47	0.49	0.31	1.04
P <sub>2</sub> O <sub>5</sub> (wt%)	0.36	0.35	0.36	0.35	0.35	0.35	0.37	0.34	0.35	0.35	0.33	0.35	0.35	0.36	0.34	0.50
SO <sub>3</sub> (wt%)	0.10	0.17	0.39	0.15	0.18	0.42	1.01	0.12	0.17	0.22	0.27	0.16	0.42	0.23	0.95	0.16
TOTAL (wt%)	99.84	99.87	99.86	99.75	99.63	99.71	99.72	99.80	99.68	99.50	99.82	99.84	99.46	99.97	99.74	99.77
LOI (wt%)	10.32	10.17	12.01	11.92	10.21	2.42	0.98	11.34	10.88	10.46	9.99	8.98	9.57	8.45	9.98	6.89

Note: Compositions are referenced to glassy, unaltered tephra sampled in 1979 at 171 meters below surface (m.b.s.) from the SE-01 drill core (Jackson et al., 2019b; Figs. 9 and S6; Table S2 [see text footnote 1]). SUSTAIN—Surtsey Underwater Volcanic System for Thermophiles, Alteration Processes and Innovative Concretes drilling project; LOI—loss on ignition.

\*Top of the 30-cm-long core segment. Vertical boreholes: SE-02A, ICDP Hole B; SE-02B, ICDP Hole C. Inclined borehole: SE-03, ICDP Hole D (vertical depths below surface shown in italics). ICDP—International Continental Scientific Drilling Program.

<sup>†</sup>Fragment of disaggregated core segment

hole temperatures in 2018 (Weisenberger et al., 2021) were 67 °C near D12, and 64 °C near D13.

The D12 and D13 subcores have dissimilar properties (Figs. 10–13; Table 3). The connected porosity in the D12 subcores is 20%–23% (average of 21%), yet the D13 subcores average 34%. The bulk density of D12 is high, 2.00–2.08 g·cm<sup>-3</sup> (average of 2.03 g·cm<sup>-3</sup>), yet is low for D13, 1.64–1.67 g·cm<sup>-3</sup> (average of 1.66 g·cm<sup>-3</sup>). The total and isolated porosities of the D12 subcores are 19.6%–22.5% and 0.0%–2.5%, respectively; they are 34.0%–37.4% and 0.6%–3.6% for the D13 subcores. Permeabil-

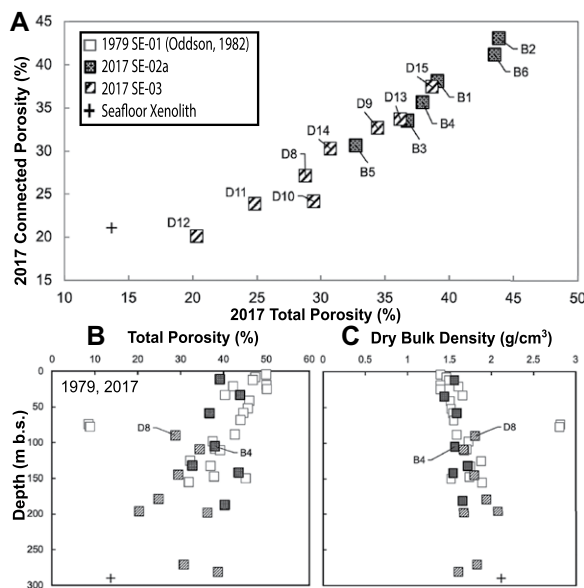
ity of D12 subcores varies from  $3.89 \times 10^{-17}$  m<sup>2</sup> to  $5.41 \times 10^{-19}$  m<sup>2</sup> (with one outlier at  $1.32 \times 10^{-15}$  m<sup>2</sup>), while the permeability of the D13 subcores is far higher,  $2.22 \times 10^{-13}$  m<sup>2</sup> to  $1.02 \times 10^{-12}$  m<sup>2</sup>. P-wave velocity is high for D12, 3.44–3.74 km·s<sup>-1</sup>, yet is low for D13, 2.45–3.11 km·s<sup>-1</sup>. The average thermal conductivity, thermal diffusivity, and specific heat capacity for D12 are 0.862 W·m<sup>-1</sup>·K<sup>-1</sup>, 0.365 mm<sup>2</sup>·s<sup>-1</sup>, and 0.8967 kJ·kg<sup>-1</sup>·K<sup>-1</sup>, respectively, and for D13, 0.633 W·m<sup>-1</sup>·K<sup>-1</sup>, 0.420 mm<sup>2</sup>·s<sup>-1</sup>, and 0.917 kJ·kg<sup>-1</sup>·K<sup>-1</sup>. The UCS of one D12 subcore is measured at 70.5 MPa, yet the UCS of one D13

subcore is just 15.4 MPa. The calculated static Young's modulus for D12 and D13 is 16.2 GPa and 5.8 GPa, respectively.

#### Lower Subseafloor Tuff and Coherent Basalt (205–285 m.b.s.; Zone 7)

A continuous section of lapilli tuff extends from 205 m to 342 m measured depth, with the exception of intrusive basalt at ~236.3–238.7 m and 342.4–352.0 m measured depth (McPhie et al., 2020). The section seems to almost entirely comprise facies resedimented from unstable tephra depositional sites and/or tephra recycled explosively through the vent (McPhie et al., 2020; Moore and Jackson, 2020). The dark greenish-gray (SGY 4/1) lapilli tuff is compact and very well lithified in the D14 core segment (217 m.b.s., 330.8 m measured depth) but porous and only moderately well consolidated in the D15 core segment (281.3 m.b.s., 343.2 m measured depth) (Figs. 1C, 2, and S2). A basaltic intrusion, core segment D16 (281.9 m.b.s., 344.2 m measured depth), may represent part of the magmatic feeder to Surtur crater (Jackson et al., 2019b; Weisenberger et al., 2022). Borehole temperatures in 2018 (Weisenberger et al., 2021) were 57 °C.

D14 has compact fine-ash matrix and few matrix pores visible at the petrographic scale (Fig. 3N). D15, by contrast, contains abundant vesicular pyroclasts and large matrix pores, of ≤5 mm in diameter, commonly with anhydrite infill (Fig. 3O). The altered glass of the fine-ash matrix of D14 is not birefringent, yet larger pyroclasts have internal mottled birefringence and intermittent oriented birefringence. There is little fine-ash matrix in D15; altered glass in larger



Figs. 3J, 3K, and 3L). (C) Dry bulk densities of 1979 samples (Oddsson, 1982) do not differ significantly from those of the 2017 samples (Table 3).

**Figure 10. Connected porosity, total porosity, and dry bulk density measurements from 1979 and 2017 drill cores. (A) Connected porosities of 2017 subcores show mainly small deviations from total porosity. (B) Total porosities of 1979 core samples (Oddsson, 1982) do not differ greatly from those of the 2017 core samples at equivalent elevations, except for B1 and B3. For example, the total porosity of B4 subcores, 36.2%, is almost identical to that measured at equivalent depth in the 1979 core, 37.5%–38.0%, 98–108.9 m.b.s. The D10, D11, and D12 lapilli tuff subcores, from 145.6 m.b.s. to 196.0 m.b.s., have low total porosities (see**



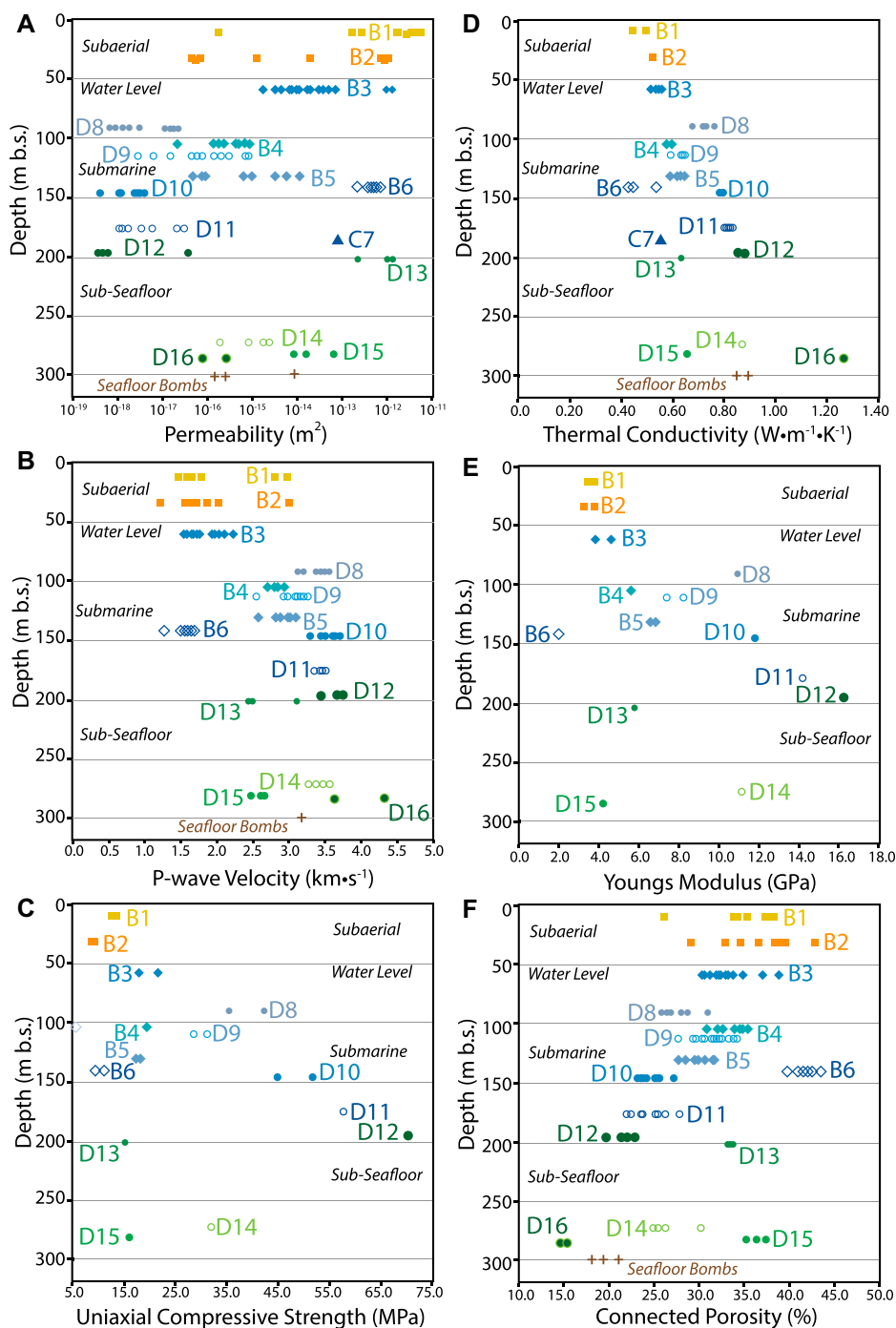


**Figure 11. Results of laboratory measurements of physical properties of 2017 Surtur pyroclastic basalt, intrusive basalt, and seafloor rock with respect to vertical depth (Fig. 2; Tables 3 and 4; Supplemental Text S1 [see text footnote 1]): (A) permeability; (B) P-wave velocity; (C) uniaxial compressive strength; (D) thermal conductivity; (E) static Young's modulus; (F) connected porosity.**

vesicular pyroclasts is weakly birefringent. In D15, XRPD identifies abundant analcime, 24–26 wt%; phillipsite, <2 wt%; Al-tobermorite and xonotlite, <1 wt%; and anhydrite, <1 wt%. Clinocllore is abundant, 16–18 wt%, and smec-

tite, <2 wt%; the amorphous content, 35–36 wt%, is presumably of clay mineral without long-range order (Fig. 4A; Table 1).

The D14 and D15 subcores have dissimilar properties (Figs. 10–13; Table 3). The connected

porosity is 25%–30% (average of 27%) for D14, and 35%–37% (average of 36%) for D15. The bulk density of D14 is high, 1.83–1.94 g·cm<sup>-3</sup>, but low for D15, 1.61–1.65 g·cm<sup>-3</sup>. D14 subcores have total and isolated porosities of 26.5%–30.7% and 0.4%–3.8%, respectively; these are 37.0%–38.7% and 1.2%–1.6% for the D15 subcores. The D14 permeability ranges from  $2.06 \times 10^{-16}$  m<sup>2</sup> to  $2.41 \times 10^{-15}$  m<sup>2</sup>, yet D15 permeability is an order of magnitude higher, from  $8.32 \times 10^{-15}$  m<sup>2</sup> to  $6.71 \times 10^{-14}$  m<sup>2</sup>. P-wave velocity for D14 is 3.28–3.56 km·s<sup>-1</sup> but 2.47–2.66 km·s<sup>-1</sup> for D15. The average thermal conductivity, thermal diffusivity, and specific heat capacity for D14 are 0.866 W·m<sup>-1</sup>·K<sup>-1</sup>, 0.485 mm<sup>2</sup>·s<sup>-1</sup>, and 0.918 kJ·kg<sup>-1</sup>·K<sup>-1</sup>, respectively; for D15, these are 0.654 W·m<sup>-1</sup>·K<sup>-1</sup>, 0.455 mm<sup>2</sup>·s<sup>-1</sup>, and 0.900 kJ·kg<sup>-1</sup>·K<sup>-1</sup>. The UCS of one subcore of D14 and one subcore of D15 are 32.0 MPa and 16.4 MPa, respectively; the static Young's modulus is calculated to be 11.1 GPa and 4.2 GPa.

The coherent intrusive basalt of the D16 subcores has low connected porosity (average of 15%) and high bulk density, 2.51 g·cm<sup>-3</sup>. Permeability is  $8.15 \times 10^{-17}$  m<sup>2</sup> to  $2.71 \times 10^{-16}$  m<sup>2</sup>, less than the D8, D10, and D11 subcore measurements, but P-wave velocity is 3.63–4.31 km·s<sup>-1</sup>. The average thermal conductivity, thermal diffusivity, and specific heat capacity are 1.26 W·m<sup>-1</sup>·K<sup>-1</sup>, 0.661 mm<sup>2</sup>·s<sup>-1</sup>, and 0.761 kJ·kg<sup>-1</sup>·K<sup>-1</sup>, respectively. No UCS tests were performed on the D16 subcores.

#### Seafloor Volcaniclastic Sedimentary Rock (Zone 8)

Subcores of xenolithic bombs of seafloor rock (Alexandersson, 1972) have low connected porosities (average of 19%) and high bulk density of 2.22 g·cm<sup>-3</sup>. Permeability and P-wave velocity are  $1.56 \times 10^{-16}$  m<sup>2</sup> to  $8.08 \times 10^{-15}$  m<sup>2</sup> and 3.17 km·s<sup>-1</sup>, respectively. The average thermal conductivity, thermal diffusivity, and specific heat capacity are 0.872 W·m<sup>-1</sup>·K<sup>-1</sup>, 0.402 mm<sup>2</sup>·s<sup>-1</sup>, and 0.989 kJ·kg<sup>-1</sup>·K<sup>-1</sup>. No UCS tests were performed on the seafloor rock. XRPD identifies analcime and phillipsite, <2 wt%; traces of calcite and gypsum; clinocllore, 6 wt%; smectite, 3 wt%; and amorphous content, 57 wt%, mainly as weakly altered detrital volcanic glass (Fig. 4; Table 1). Whole-rock compositions have high SiO<sub>2</sub>, Fe<sub>2</sub>O<sub>3</sub>, and K<sub>2</sub>O, but low Na<sub>2</sub>O and Al<sub>2</sub>O<sub>3</sub> in comparison to 1979 reference tephra (Fig. 9; Table 2).

## DISCUSSION

### Porosity, Permeability, and Strength

Permeability and UCS measurements of the lapilli tuff subcores increase and decrease,



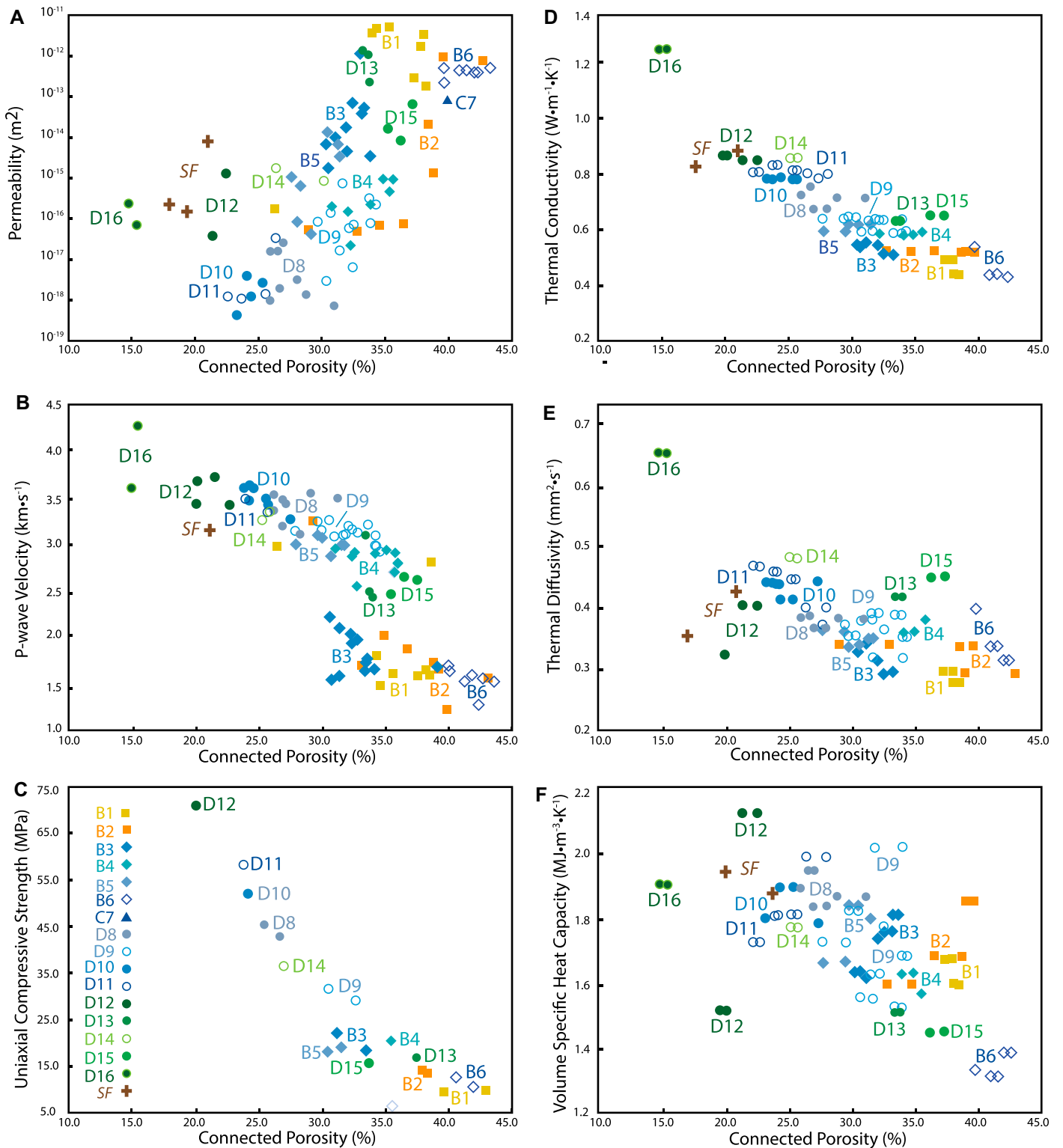


**Figure 12. Results of laboratory measurements of physical properties of 2017 Surtur pyroclastic basalt, intrusive basalt, and seafloor rock subcores as a function of connected porosity (Fig. 2; Tables 3 and 4; Supplemental Text S1 [see text footnote 1]): (A) permeability; (B) P-wave velocity; (C) uniaxial compressive strength (UCS); (D) thermal conductivity; (E) thermal diffusivity; (F) volume-specific heat capacity.**

respectively, as a function of increasing porosity (Fig. 12) in accordance with previously published data for volcanic rocks (e.g., Farquharson

et al., 2015; Heap and Violay, 2021). These measurements reveal two structural puzzles within the Surtur deposits.

First, subcores with the highest strengths (D10, D11, and D12, at 145.6 m.b.s., 178.9 m.b.s., and 196.0 m.b.s., respectively) occur

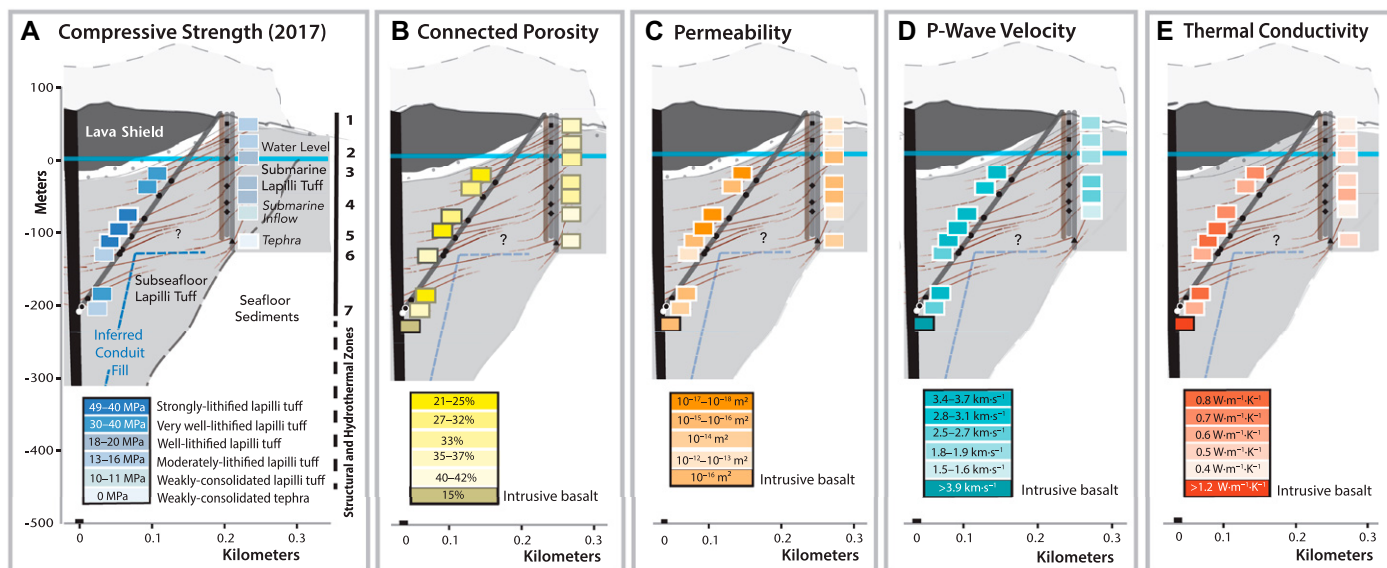


**Figure 13.** Sketches showing the current structure of Surtur deposits: (A) uniaxial compressive strength (UCS); (B) connected porosity; (C) permeability; (D) P-wave velocity; and (E) thermal conductivity. Pyroclastic eruptions at Surtur terminated on January 31, 1964. By June 1979, tephra had mainly consolidated to form lapilli tuff with heterogeneous properties (measured in 2017 drill cores). Lithification is referenced to UCS. Some submarine lapilli tuff subcores have permeability two orders of magnitude less than the Surtur intrusive basalt.

at elevations near the pre-eruption seafloor (Figs. 2A and 13). To the east, very weakly consolidated tephra (C7, at 181.3 m.b.s.) disaggregates so that strength cannot be measured (Figs. 6A–6D, 11, and 12). The weakly consolidated tephra and lapilli tuff deposits encountered in the lower submarine zone by the

vertical boreholes may persist for a few tens of meters to the west. However, there are no sustained traces of weakly consolidated tephra or lapilli tuff in the submarine and subseafloor sections of the inclined borehole (McPhie et al., 2020). Instead, the D10–D12 subcores correspond to very well- to strongly lithified

deposits with layers inclined at apparent dips of 40°–80°WNW (McPhie et al., 2020; Moore and Jackson, 2020; Fig. 1C). A material discontinuity evidently exists within the ~130 m of lateral separation between the vertical and inclined boreholes at the elevation of the pre-eruption seafloor (Figs. 2A and 13).

**TABLE 3. MATERIAL AND MECHANICAL PROPERTIES OF SUBCORE SAMPLES OF 2017 SURTUR DRILL CORE SEGMENTS FROM PRINCIPAL STRUCTURAL AND HYDROTHERMAL ZONES**

Structural and thermal zones	Vertical depth* (m.b.s.)	Subcore sample	Dry bulk density (g/cm <sup>3</sup> )	Connected porosity (%)	Total porosity (%)	Isolated porosity (%)	Permeability (m <sup>2</sup> )	P-wave velocity (km/s)	Compressive strength (MPa)	Young's modulus (GPa)
Subaerial tuff cone (0–56 m.b.s.; zone 1)	12, 35	B1, B2	1.43–1.78	26.4–43.1	30.3–42.9	0.0–3.9	2.18 × 10 <sup>-13</sup> to 2.38 × 10 <sup>-12</sup>	1.48–2.99	9.2–13.7	3.2–3.8
Tidal flux zone (56–65 m.b.s.; zone 2)	58	B3	1.49–1.67	30.6–39.0	33.7–40.9	0.0–3.8	1.50 × 10 <sup>-13</sup>	1.55–2.22	18.1–21.8	3.8–4.6
Upper submarine lapilli tuff (65–142 m.b.s.; zone 3)	105, 132 90, 109	B4, B5 D8, D9	1.56–1.77 1.59–1.85	27.9–35.9 26.1–34.4	30.6–37.9 27.1–37.6	1.8–2.8 0.0–4.2	4.15 × 10 <sup>-16</sup> to 2.79 × 10 <sup>-15</sup> 7.95 × 10 <sup>-18</sup> to 1.42 × 10 <sup>-16</sup>	2.60–3.11 2.56–3.20	17.6–19.8 28.9–42.6	5.6–6.8 8.2–10.9
Submarine inflow zone (142–155 m.b.s.; zone 4)	142	B6	1.50–1.58	39.9–43.5	42.2–45.2	1.5–2.4	4.06 × 10 <sup>-13</sup>	1.28–1.68	9.9–11.6	2.0
Lower submarine tephra and lapilli tuff (145–186 m.b.s.; zone 5)	145, 179 181	D10, D11 C7 <sup>†</sup>	1.80–2.00 —	22.3–28.1 —	22.4–29.5 40.3	0.0–5.3 —	2.37 × 10 <sup>-18</sup> to 8.86 × 10 <sup>-18</sup> 7.72 × 10 <sup>-14</sup>	3.29–3.71 —	45.0–57.9 —	11.8–14.1 —
Uppermost subseafloor lapilli tuff (195–205 m.b.s.; zone 6)	196 198	D12 D13	2.00–2.08 1.64–1.73	20.0–22.6 33.4–33.9	19.6–22.5 34.0–37.4	0.0–2.5 0.6–3.6	3.14 × 10 <sup>-16</sup> 8.37 × 10 <sup>-13</sup>	3.44–3.74 2.45–3.11	70.5 15.4	16.2 5.8
Lower subseafloor tuff and coherent basalt (205–285 m.b.s.; zone 7)	271 281 282	D14 D15 D16	1.83–1.94 1.61–1.65 2.51	25.2–30.3 35.4–37.5 14.9–15.4	26.5–30.7 37.0–38.7 —	0.4–3.8 1.2–1.6 —	1.31 × 10 <sup>-15</sup> 3.04 × 10 <sup>-14</sup> 1.76 × 10 <sup>-16</sup>	3.28–3.56 2.47–2.66 3.63–4.31	32.0 16.4 —	11.1 4.2 —
Seafloor volcanoclastic sedimentary rock (zone 8)	Subaerial tuff cone <sup>§</sup>	S3T-01 S3T-02 S8T-01	2.25 2.29 2.11	19.4 18.0 21.1	— — —	— — —	1.56 × 10 <sup>-16</sup> 2.38 × 10 <sup>-16</sup> 8.08 × 10 <sup>-15</sup>	3.17 — —	— — —	— — —

*Note:* Regarding structural and thermal zones, see Figures 1, 2, 10–13, and S1–S2; Table S1; and Supplemental Data S1 (see text footnote 1 for Supplemental Material). A cell with a dash signifies no material or mechanical property measurement. m.b.s.—meters below surface.  
<sup>\*</sup>Top of the 30-cm-long core segment. Vertical boreholes: SE-02A, ICDP Hole B; SE-02B, ICDP Hole C. Inclined borehole: SE-03, ICDP Hole D (vertical depths below surface shown in italics). Elevations rounded to nearest meter. ICDP—International Continental Scientific Drilling Program.  
<sup>†</sup>Fragment; the C7 core segment disaggregated during subcore preparation.  
<sup>§</sup>Lithic bombs of seafloor volcanoclastic sedimentary rock.

Second, proximate subseafloor lapilli tuff deposits—the D12 and D13 samples, 6 m apart, and the D14 and D15 samples, 10 m apart—show pronounced differences in porosity, permeability, UCS, and P-wave velocity. The porous lapilli tuff of D13 and D15 has high connected porosity, high permeability, and low UCS and P-wave velocity (Figs. 13A–13D; Table 3). The compact lapilli tuff of D12 and D14, by contrast, has permeability several orders of magnitude lower, and much higher UCS and P-wave velocity.

Three central questions emerge from these observations. How did the strong anisotropy in permeability and strength develop? What do these disparate physical characteristics reveal about explosive eruptive processes and the subseafloor deposits? What is the present distribution of weakly consolidated deposits in the Surtur structure?

### Permeability and Strength Modeling

Two models provide insights into how lapilli tuff fabrics influence permeability and strength. A permeability model optimized for granular materials such as basaltic tephra (Wadsworth et al., 2016) provides insight into links among porosity, grain size, and permeability. Next, a micromechanical model that describes the mechanical behavior and strength of porous materials, the wing-crack model of Sammis and Ashby (1986), provides insight into the influence of porosity and pore size on UCS.

The permeability model (Wadsworth et al., 2016) provides theoretical permeability-porosity curves for grain diameters of 0.1  $\mu\text{m}$ , 1  $\mu\text{m}$ , 10  $\mu\text{m}$ , and 100  $\mu\text{m}$  (Figs. 14A and S7). The porosity-permeability data for the lapilli tuff samples cannot be described by a single modeled curve, and thus reflect a variable representative grain size, and therefore pore size. Overall, measured permeability decreases with depth, which suggests a component of lithostatic compaction as measured through levelling surveys (Moore et al., 1992), as well as the partial closure of pores with mineral cements (Figs. 6–8).

The modeled curve for an average grain diameter of 0.1  $\mu\text{m}$  coincides with low-permeability measurements for the compact submarine and subseafloor subcores. The predicted range in grain diameter is significantly smaller than the typical coarse ash- to fine lapilli-sized grain diameter (1–10 mm; McPhie et al., 2020; Moore and Jackson, 2020) and instead better represents the very fine-ash fraction of the binding matrix (Figs. 3H–3L and 3N). By contrast, the modeled curve for an average grain diameter of 100  $\mu\text{m}$  correlates with high permeability data for the porous subseafloor lapilli tuff, D13 and D15, and the submarine inflow zone, B6, which contain

little fine-ash fraction (Figs. 3F, 3M, and 3O), as well as some B1 and B2 subcores from the subaerial tuff cone. The analysis suggests that permeability is largely controlled by the smallest grain size fraction and, therefore, the smallest pore size fraction.

In the pore-crack micromechanical model (Sammis and Ashby, 1986), the term  $\frac{K_{IC}}{\sqrt{\pi r}}$  in

the analytical solution for the model, provided by Zhu et al. (2010), incorporates the two unknowns:  $K_{IC}$  the fracture toughness (a material property that describes the resistance of brittle materials to the growth and propagation of cracks), and  $r$ , the pore radius. If these variables are constant over the dataset, then one theoretical curve should capture the trend of all the data. However, the experimental data are bracketed

between  $\frac{K_{IC}}{\sqrt{\pi r}} = 3 \text{ MPa}$  and  $\frac{K_{IC}}{\sqrt{\pi r}} = 27 \text{ MPa}$

(Fig. 14B), which suggests that the  $K_{IC}$  or the pore radius of the lapilli tuff is not constant. If the  $K_{IC}$  for all of the subcores is held constant,

the model can be used to explore the pore size that is controlling the mechanical behavior (Equation S4). Selecting two values of  $K_{IC}$  for the basaltic tuff, 0.3  $\text{MPa}\cdot\text{m}^{0.5}$  and 0.15  $\text{MPa}\cdot\text{m}^{0.5}$  (Zhu et al., 2011; Heap et al., 2015; Heap and Violay, 2021), the analysis demonstrates that for 0.3  $\text{MPa}\cdot\text{m}^{0.5}$ , the maximum and minimum pore radii, 3.18 mm and 0.04 mm, are too large for most lapilli tuff fabrics. However, for 0.15  $\text{MPa}\cdot\text{m}^{0.5}$ , the maximum and minimum pore radii, 0.8 mm and 0.01 mm, fall within the range of most fabrics (Fig. 3). Indeed, the very low UCS measured for the B6 subcores with large vesicular pyroclasts and little fine-ash matrix, 10–11 MPa, falls on the curve suggesting larger pores, while the very high UCS, 70 MPa, of the compact D12 subcores with abundant very fine-ash matrix (Fig. 3L) falls on the curve suggesting very small pores. Thus, the analysis implies that pore size controls the mechanical behavior.

### Reworked Tephra in Surtseyan Vent Deposits

Large pores that surround vesicular pyroclasts in Surtseyan tephra deposits commonly form near the surface through the entrapment

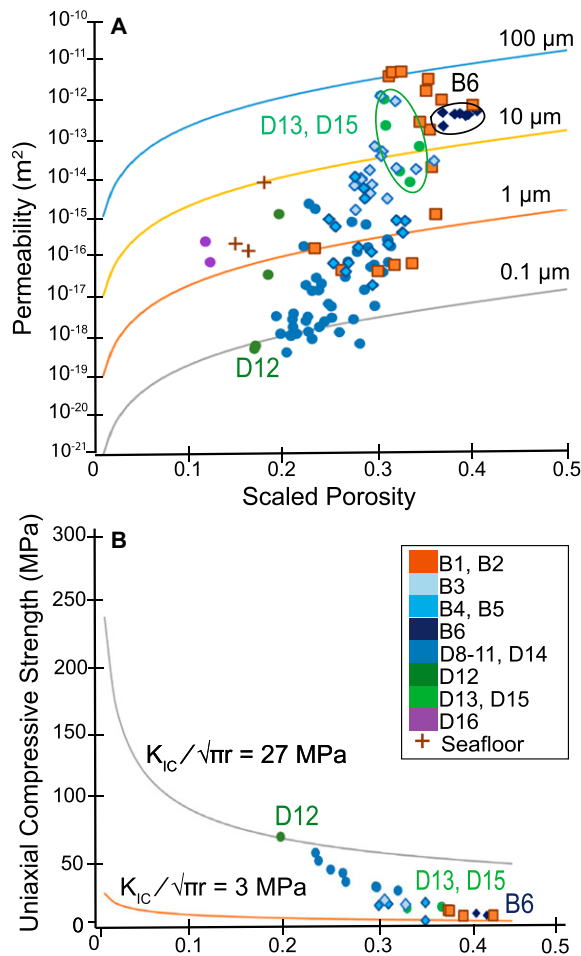


**Figure 14. Permeability and micromechanical modeling.** (A) Permeability as a function of scaled fractional porosity (connected porosity minus 0.03) for the lapilli tuff subcores (Table 3). Modeled curves for monodisperse grain diameters from 0.1  $\mu\text{m}$  to 100  $\mu\text{m}$  use Equations S2 and S3 (see text footnote 1). (B) Uniaxial compressive strength as a function of fractional connected porosity for the lapilli tuff subcores. Modeled curves for  $\frac{K_{IC}}{\sqrt{\pi r}} = 3 \text{ MPa}$  (upper gray curve) and  $\frac{K_{IC}}{\sqrt{\pi r}} = 27 \text{ MPa}$  (lower black curve) use the pore-crack model of Sammis and Ashby (1986; Equation S4 [see text footnote 1]).

or entrainment of steam or liquid water (Lorenz, 1974; Go and Sohn, 2021); the pores are unlikely to form in deposits of lapilli or ash that fall on the sea surface and descend through the submarine environment. Matrix pores measured in thin sections of submarine lapilli tuff from the 1979 SE-01 and 2017 SE-02B cores show decreasing volume with depth (Moore, 1985; Moore and Jackson, 2020). In the seafloor deposits of the SE-03 core, however, six of 16 reference samples contain 5–15 vol% matrix pores.

The  $\mu$ -computed tomography reconstructions of seafloor lapilli tuff (Kahl et al., 2021b) illustrate porous fabrics dominated by coarse pyroclasts surrounded by large, connected pores (Figs. 6I and 6J), as well as compact fabrics dominated by very fine-ash matrix with pores <7.5  $\mu\text{m}$  voxel size resolution (Fig. 6K). The porous fabrics suggest that tephra entrapped steam or other atmospheric gases near the surface and then descended through the eruptive conduit (Moore, 1985; McPhie et al., 2020). This may be somewhat similar to processes in continental maar-diatreme volcanoes, where extensive syn-eruptive subsidence of pyroclastic deposits is documented in some localities (White and Ross, 2011; Delpit et al., 2014; Bélanger and Ross, 2018). The compact fabrics reflect phreatomagmatic eruptions that, by their nature, tend to generate abundant ash, including fine ash. A fine- to very fine-ash fraction can be produced through brittle fragmentation (Wohletz et al., 2013), brittle disintegration of vesicular pyroclasts (Liu et al., 2015), and in situ granulation of tephra (Colombier et al., 2019). These processes may also occur during explosive reworking of freshly erupted tephra (Moore, 1985; McPhie et al., 2020).

### Thermal Property Modeling

With increasing porosity, thermal conductivity and diffusivity measurements of the lapilli tuff subcores decrease while specific heat-capacity measurements remain more-or-less constant, in accordance with previous studies (Figs. 12D–12F; e.g., Robertson and Peck, 1974; Heap et al., 2020b). To provide insights into the thermal properties of the water-saturated pyroclastic deposits, data for the vacuum-dry thermal conductivity, thermal diffusivity, and specific heat capacity (Table 4) are evaluated against effective medium approaches (Fig. 15; Supplemental Text S6; Heap et al., 2020b).

The thermal conductivity measurement data (Fig. 13E) can be bracketed between modeled curves (using the Maxwell equation) that assume values for thermal conductivity at zero porosity,  $\lambda_0$ , of 0.85  $\text{W}\cdot\text{m}^{-1}\cdot\text{K}^{-1}$  and 1.30  $\text{W}\cdot\text{m}^{-1}\cdot\text{K}^{-1}$  (Fig. 15A, yellow curves; Equation S5). For these curves,  $\lambda_p$ , the conductivity of the pore fluid (i.e., air), is taken as 0  $\text{W}\cdot\text{m}^{-1}\cdot\text{K}^{-1}$ . The difference in  $\lambda_0$  could be explained by variable in situ alteration (Heap et al., 2022). For the water-saturated prediction, modeled curves use  $\lambda_p = 0.6 \text{ W}\cdot\text{m}^{-1}\cdot\text{K}^{-1}$  (i.e., liquid water). Saturation can significantly increase thermal conductivity at higher porosities (Fig. 15A, blue curves). At a connected porosity of 0.4, for example, the upper-bound difference in dry and water-saturated thermal conductivity is 0.65  $\text{W}\cdot\text{m}^{-1}\cdot\text{K}^{-1}$  and 0.99  $\text{W}\cdot\text{m}^{-1}\cdot\text{K}^{-1}$ , respectively (Fig. 15A, black triangles). This suggests that porous lapilli tuff could have a wet upper bound for thermal conductivity that is nearly double the measured vacuum-dry thermal conductivity (0.5–0.7  $\text{W}\cdot\text{m}^{-1}\cdot\text{K}^{-1}$ ).

The thermal diffusivity measurement data (Fig. 12E) fall mainly within the dry upper and lower bounds of the effective medium model predictions (Fig. 15B, yellow curves; Equations S6 and S7; Heap et al., 2020b). The predicted water-saturated thermal diffusivity would decrease from  $\sim 0.45 \text{ mm}^2\cdot\text{s}^{-1}$  to  $\sim 0.35 \text{ mm}^2\cdot\text{s}^{-1}$  for porous lapilli tuff (Fig. 15B, black triangles); it would decrease from  $\sim 0.5 \text{ mm}^2\cdot\text{s}^{-1}$  to  $\sim 0.4 \text{ mm}^2\cdot\text{s}^{-1}$  for compact lapilli tuff (Fig. 15B, gray triangles). The data for specific heat capacity are centered on the dry curve of the model prediction at  $\sim 1.0 \text{ kJ}\cdot\text{kg}^{-1}\cdot\text{K}^{-1}$ , with small excursions for higher and lower porosity lapilli tuff and the basaltic intrusion (Fig. 15C). As for the predicted thermal conductivities (Fig. 15A), water saturation can significantly increase the specific heat capacity of porous lapilli tuff. The modeled curves do not accurately describe data for intrusive basalt characterized by, for example, a different  $\lambda_0$ . The best-fit value of  $\lambda_0$  would be 1.6  $\text{W}\cdot\text{m}^{-1}\cdot\text{K}^{-1}$ , similar to that of basaltic lava from Hawai'i, USA (Robertson and Peck, 1974).

Stefánsson et al. (1985) used laboratory measurements of thermal conductivity of wet Surtur lapilli tuff, 1.0  $\text{W}\cdot\text{m}^{-1}\cdot\text{K}^{-1}$  (Axelsson et al., 1982), to model heat flow in the submarine deposits below water level. The well-lithified 2017 submarine lapilli tuff, zone 3, has vacuum-dry thermal conductivity of  $\sim 0.6 \text{ W}\cdot\text{m}^{-1}\cdot\text{K}^{-1}$  and connected porosity of 30%–33% (Tables 3 and 4, and subcores B4 and B5). The effective medium model indicates wet thermal conductivity in the range of 0.8–1.1  $\text{W}\cdot\text{m}^{-1}\cdot\text{K}^{-1}$  (Fig. 15A, black triangles), which is nearly identical to the 1979 measurement. The calculated thermal diffusivity and estimated specific heat capacities in Stefánsson et al. (1985), 0.33  $\text{mm}^2\cdot\text{s}^{-1}$  and 1.54

TABLE 4. THERMAL PROPERTIES OF SUBCORE SAMPLES OF 2017 SURTUR DRILL CORE SEGMENTS FROM PRINCIPAL STRUCTURAL AND HYDROTHERMAL ZONES

Structural and thermal zones*	Vertical depth† (m.b.s.)	Subcore sample	Thermal conductivity ( $\text{W}\cdot\text{m}^{-1}\cdot\text{K}^{-1}$ )	Thermal diffusivity ( $\text{mm}^2\cdot\text{s}^{-1}$ )	Specific heat capacity ( $\text{kJ}\cdot\text{kg}^{-1}\cdot\text{K}^{-1}$ )	Volume-specific heat capacity ( $\text{kJ}\cdot\text{m}^{-3}\cdot\text{K}^{-1}$ )
Subaerial tuff cone (0–56 m.b.s.; zone 1)	12.2	B1	0.470	0.287	1.048	1.636
	35.0	B2	0.524	0.325	1.107	1.622
Tidal flux zone (56–65 m.b.s.; zone 2)	57.6	B3	0.538	0.317	1.056	1.703
	105.0	B4	0.589	0.363	1.024	1.625
Upper submarine lapilli tuff (65–142 m.b.s.; zone 3)	137.1	B5	0.622	0.357	1.016	1.746
	89.5	D8	0.719	0.383	1.052	1.880
	109.1	D9	0.624	0.367	1.030	1.709
	148.1	B6	0.472	0.351	0.873	1.346
	145.6	D10	0.788	0.436	0.986	1.809
Submarine inflow zone (142–155 m.b.s.; zone 4)	178.9	D11	0.814	0.446	0.947	1.832
	181.3	C7‡	0.547	0.529	0.630	1.038
	196.0	D12	0.862	0.365	0.897	2.395
	198.0	D13	0.633	0.420	0.917	1.508
Lower submarine tephra and lapilli tuff (145–186 m.b.s.; zone 5)	271.0	D14	0.866	0.485	0.918	1.784
	281.3	D15	0.654	0.455	0.900	1.438
	281.9	D16	1.259	0.661	0.761	1.903
Seafloor volcanoclastic sedimentary rock (zone 8)	Subaerial tuff cone	S8T	0.872	0.402	0.989	2.171

Note: m.b.s.—meters below surface.

\*See Figures 1, 2, 11–13; Table S1 (see text footnote 1).

†Top of the 30-cm-long core segment. Vertical boreholes: SE-02A, ICDP Hole B; SE-02B, ICDP Hole C. Inclined borehole: SE-03, ICDP Hole D (subcore samples and vertical depths below surface shown in italics). ICDP—International Continental Scientific Drilling Program.

‡Fragment; the C7 core segment disaggregated during subcore preparation.



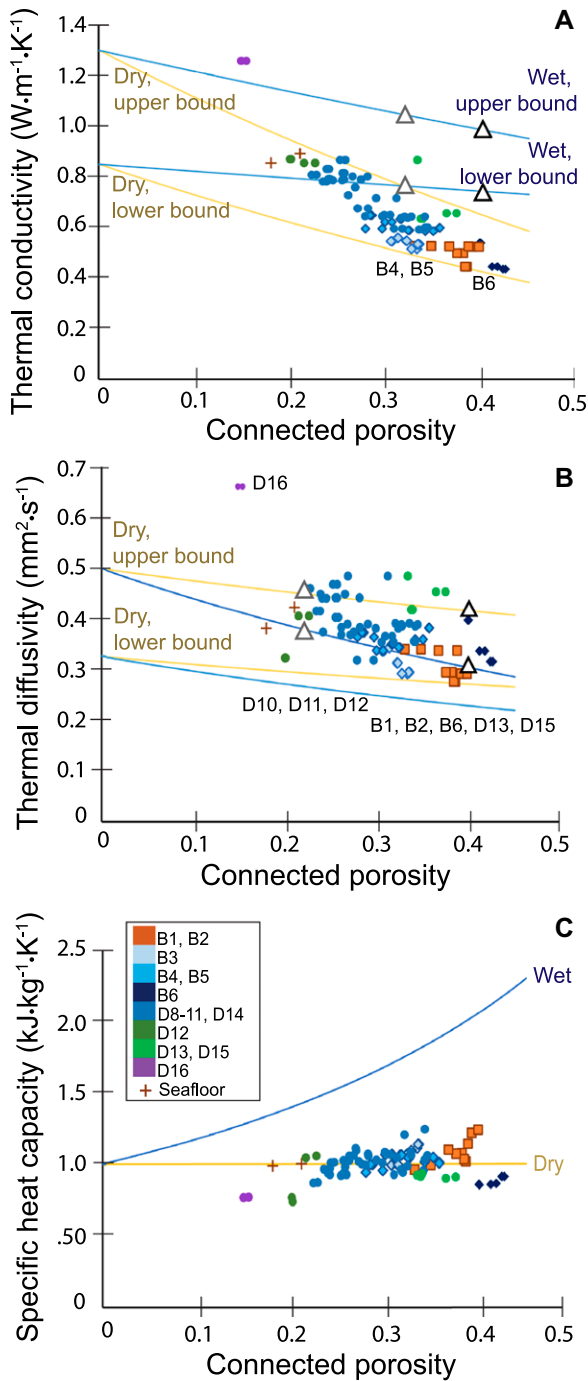


**Figure 15. Thermal property modeling as a function of connected porosity for Surtur pyroclastic basalt, intrusive basalt, and seafloor sedimentary rock subcores: (A) thermal conductivity; (B) thermal diffusivity; and (C) specific heat capacity. Modeled curves use the effective medium approaches described in Equations S6 and S7 (see text footnote 1) to evaluate dry (or steam-saturated) and water-saturated rocks.**

$\text{kJ}\cdot\text{kg}^{-1}\cdot\text{K}^{-1}$ , fall mainly within the range of measured and modeled values (Figs. 15B and 15C). Thermal diffusivity, however, may be  $>0.33 \text{ mm}^2\cdot\text{s}^{-1}$  for dry (or steam-saturated) lapilli tuff or lapilli tuff with porosity of  $<40\%$ . The dry (or steam-saturated) specific heat capacity is likely not  $>1.25 \text{ kJ}\cdot\text{kg}^{-1}\cdot\text{K}^{-1}$  and, in the case of water-saturation, is likely  $<2 \text{ kJ}\cdot\text{kg}^{-1}\cdot\text{K}^{-1}$ . The new data and models can be used to further refine heat flow models through the Surtur structure, although temperature, a factor known

to influence thermal properties (Vosteen and Schellschmidt, 2003), is not considered.

#### Rates of Material Change

##### Vertical Cores, 1979–2017

The physical characteristics of weakly consolidated tephra deposits in proximity to the cool pre-eruption seafloor do not appear to have changed substantially since they were drilled in 1979 (Oddsson, 1982): total porosity, 31.9%–

45.2% in 1979 and 40.3% in 2017, remains high, and dry bulk density,  $1.52 \text{ g}\cdot\text{cm}^{-3}$  in 1979 and  $1.54 \text{ g}\cdot\text{cm}^{-3}$  in 2017, remains low. Although no authigenic minerals were detected in 1979 at 140.0–143.8 m.b.s. (Jakobsson and Moore, 1986), traces of clinocllore and smectite minerals, anhydrite, and calcite are detected in 2017 (Figs. 3F, 4A, 4B, and 5). A measurable gain in cohesion occurred in this inflow zone, 4, which maintained a borehole temperature of  $85\text{--}90^\circ\text{C}$ . (Fig. 2B). Prause et al. (2022) found an overall mass increase in bulk-rock weight percent gains for  $\text{SiO}_2$ ,  $\text{Al}_2\text{O}_3$ ,  $\text{FeO}$ ,  $\text{MgO}$ , and  $\text{Na}_2\text{O}$  in SE-02B core samples at 140–150 m.b.s. relative to the composition of 1963 Surtur scoria (Schipper et al., 2015). This suggests that in situ mineralization (rather than leaching) is ongoing.

Mineral surface coatings in the matrix pores of upper submarine lapilli tuff from zone 3 were well-established in 1979 (Figs. 6E and 7B–7D); rock strength was sufficient to preserve 2-m-long core runs (Jakobsson and Moore, 1982, 1986). Early decreases in the connectivity of pore space, which influences permeability, could have produced the Ca-Si-Al-enriched solutions from which Al-tobermorite crystallized on analcime selvages (Kleine et al., 2020). The average values of permeability for B4 and B5, however, are two to three orders of magnitude less than the  $2.5\text{--}4.1 \times 10^{-13} \text{ m}^2$  calculated for equivalent deposits in 1979 (but without borehole or laboratory permeability measurements; Axelsson et al., 1982; Stefánsson et al., 1985). The difference suggests a possible overestimate of permeability calculated for the 65–100 m.b.s. depth in 1979 as compared with 2017 laboratory measurements at equivalent depth. The apparent discrepancy could also be explained by fractures, which are not present in the subcores.

##### Inclined Core, 2017

The highly altered D13 and D15 lapilli tuff subcores with abundant matrix pores contain 34–35 wt% crystalline cements, yet have physical characteristics similar to weakly altered, submarine lapilli tuff of the B6 subcore, with  $<2 \text{ wt}\%$  crystalline cements (Figs. 11 and 12; Tables 1 and 3). Permeability ranges from  $10^{-14} \text{ m}^2$  to  $10^{-13} \text{ m}^2$  in all three samples. The D13 and D15 subcores have UCS and P-wave velocities that are only slightly higher than those of the B6 subcores (Figs. 13A and 13D). An abundance of mineral cements does not necessarily confer high strength to the porous lapilli tuff.

By contrast, the well-lithified D8, D10, and D11 subcores have UCS and P-wave velocities that approach those of D12 subcores, 70 MPa and  $3.44\text{--}3.74 \text{ km}\cdot\text{s}^{-1}$  (Figs. 11–13). The borehole temperature measured in 2018 at D12,  $67^\circ\text{C}$ , is substantially lower than at D8 and D9, which is

125 °C and 87 °C, respectively (Weisenberger et al., 2021). The mass proportion of crystalline cements, 33–35 wt%, is nearly identical, however (Fig. 4A; Table 1). Higher temperature in the 2017 hydrothermal system does not necessarily correlate with higher strengths, P-wave velocities, or greater mass proportions of mineral cements.

Xonotlite, a hydrothermal calcium-silicate mineral, is detected in B3–B5 and D8–D15 lapilli tuff (Fig. 4; Table 1). Laboratory synthesis of xonotlite readily takes place at >180 °C, while low-temperature synthesis occurs over days and months at 150–180 °C. Al-tobermorite may convert to xonotlite at >175 °C in the absence of NaOH (Barnes and Scheetz, 1989; Shaw et al., 2000). These syntheses suggest that: (1) xonotlite may have continued to develop near 125 m.b.s. (Jakobsson and Moore, 1986) in upper submarine deposits transected by the SE-02A and SE-02B cores (Figs. 4A and 4C) and (2) early temperatures in deeper deposits transected by the SE-03 core may have been substantially higher than those measured in 2018. The intrusion of basaltic dikes, perhaps including those that fed lavas, could have heated the wet, warm deposits of reworked tephra in the eruptive conduit, possibly to >150 °C (e.g., Valentine and White, 2012). These hypothesized high temperatures do not appear to have had a primary, systematic influence on the progressive acquisition of rock strength, however. Rather, higher UCS correlates with abundant binding fine-ash matrix and lower connected porosity (Figs. 12C and 13). This suggests toughening through the packing of very fine ash among shards of fine ash, which substantially reduces pore size in the matrix (Fig. 6) and appears to control mechanical behavior (Fig. 14B).

#### **Nanocrystalline Clay Mineral in Altered Glass**

QPA-XRPD analyses of highly altered submarine and subseafloor lapilli tuff detect a high content in amorphous phases, 36–44 wt% (Figs. 4C and 4D; Table 1). Here, very fine ash remains isotropic in cross-polarized light, which suggests transitionally nanocrystalline domains. These domains have phyllosilicate diffraction peaks that are consistent with chlorite and trioctahedral smectite-group minerals, but without long-range order (Figs. 5 and S3–S5). Similar domains were previously identified as nanocrystalline nontronite, an Fe(III)-rich dioctahedral smectite clay mineral, in  $\mu$ XRD studies of archived 1979 drill core (Jackson et al., 2019a) or as trioctahedral and dioctahedral clay mineral species (Montesano et al., 2023). Mixed amorphous and nanocrystalline domains with diffraction patterns indicative of trioctahedral and dioctahedral smectite-group clay minerals

have been described in transmission electron microscopy studies of basaltic paleosoils (Smith and Horgan, 2021). Trioctahedral clay minerals identified on oriented mounts of Krafla, Iceland, basaltic drill core are predominantly saponite, corrensite (with 1:1 regular interstratification of trioctahedral chlorite and trioctahedral smectite), and chlorite. Spatial distribution is not correlated with borehole temperature but rather with kinetic effects related to the fluid/rock ratio as well as fluid transport and/or the cooling rate (Escobedo et al., 2021).

Materials described as amorphous gel-palagonite or as palagonite show a progression to intimate mixtures of authigenic smectitic clay minerals, including dioctahedral and trioctahedral members, such as nontronite and/or saponite in diverse pyroclastic deposits (Hay and Iijima, 1968; Zhou et al., 1992; Stroncik and Schmincke, 2002; Pauly et al., 2011). A negative volume change of 10–20 vol% is considered common in palagonitized tuffs (Hay and Iijima, 1968; Zhou and Fyfe, 1989; Prause et al., 2022). Much of this incipient compaction should be accommodated by vesicles in pyroclasts and matrix pores. By contrast, the progressive transformation of basaltic glass to nanocrystalline clay mineral(s) in very fine-ash matrix may produce consolidation across pores of <5  $\mu$ m in diameter (Fig. 6) that further decreases bulk-rock permeability.

#### **The Surtur Structure in 2017**

Surtsey is the subaerial segment of a volcanic ridge (Fig. 1A) that includes the submarine remnants of Surtla, a flat-topped seamount, and Syrtlingur and Jólnir, ephemeral islands rapidly eroded by oceanic waves (Thorarinsson et al., 1964; Thorarinsson, 1967; Romagnoli and Jakobsson, 2015). Quantification of erosion and sedimentation of Surtsey subaerial deposits since 1967 with digital elevation model differencing indicates that ~45% of the lava fields, but only ~16% of the tuff cones, have eroded away (Óskarsson et al., 2020). Marine abrasion reached the core of the Surtungur tuff cone on the northwestern coast in 1983–1985 (Fig. 1B), yet coastal erosion of the southeastern Surtur tuff cone is still largely protected by lava fields (Jakobsson et al., 2000). Even so, surficial abrasion by vortex shedding is induced by wind-driven currents, and seasonal runoff of rain deepens gullies in unconsolidated tephra down to lithified lapilli tuff (Óskarsson et al., 2020). When the lava fields eventually erode away, wave abrasion will attack the weakly consolidated submarine deposits of zones 4 and 5 (Fig. 1C), although a reduction in the intensity of wave erosion should occur at deeper water depths of 85–130 m.b.s.l. (Sunamura, 2021). The abrupt, lateral discon-

tinuity from weakly consolidated tephra (C7) to very well-lithified tuff (D10–D12; Figs. 2A and 13) could prove to be a critical factor in slowing abrasion. The projected erosion curve of Jakobsson et al. (2000) predicts that erosion will reach the core of the island in ~100 years, but the core itself may survive for centuries as a tuff crag. The strongly cohesive fabrics of the D10–D12 subcores further validate the prospect of Surtsey evolving to a well-lithified island with steep sea cliffs, as has occurred elsewhere in the Vestmannaeyjar archipelago (Fig. 1A).

There is no contiguous layer of weakly consolidated lapilli tuff in the inclined SE-03 drill core (McPhie et al., 2020, their fig. 3), despite intermittent deposits with coarse vesicular pyroclasts and connected pores (Jackson, 2020; Moore and Jackson, 2020; Kahl et al., 2021a, 2021b). The submarine inflow zone (4) and underlying zone of weakly consolidated lapilli tuff and tephra (5) therefore do not seem to present a throughgoing zone of low cohesion and high permeability that would threaten the overall stability of the island. Instead, the great vigor of the tall, continuous uprush eruptive columns, ranging from 100 m to 250 m in basal diameter (Thorarinsson, 1965), suggests that the depth of explosive quarrying of seafloor rock, as well as previously erupted tephra, could extend below the base of the SE-03 borehole at 200 m.b.s.l. (Moore, 1985). Although the structure of the eruptive conduit remains poorly defined, the well-lithified, upper subseafloor lapilli tuff could further stabilize the subaerial presence of the island over time.

#### **Clues to Surtseyan Volcanism Worldwide**

G.K. Gilbert (1890) described Pahvant Butte as a “cratered cone” that emerged from Pleistocene Lake Bonneville. The “material is a volcanic tuff, that is to say, it consists of light lapilli cemented into a coherent mass. The vesicles of the lapilli are not filled, but the fragments are so finely held together that they are frequently broken across when the mass is fractured ... The associated lake phenomena suggest, and indeed demonstrate, that Lake Bonneville afforded the moisture necessary for cementation, and that the eruption was subaqueous.” At Surtur, a “cratered cone” of smaller size, the hypothesis that the susceptibility of the lapilli deposits to erosion is “prevented by the cement” (1890, p. 327) is validated by the rapid mineralization and consolidation of submarine lapilli tuff in 1979 (Jakobsson and Moore, 1986). In 2017, the mass proportion of mineral cements, 33–35 wt%, was roughly equivalent through the moderately to strongly lithified submarine and subseafloor lapilli tuff deposits (Fig. 4A). Large variations in permeability and strength (Figs. 13A and 13C) are controlled mainly by the smallest grain size frac-

tion and, therefore, the smallest pore size fraction (Fig. 14), rather than a simple abundance of mineral cements.

The weakly lithified surficial deposits of tuff cones produced by Surtseyan eruptions, whose “sides are conspicuously furrowed by erosion” (Gilbert, 1890, p. 327), may belie a highly resilient pyroclastic rock interior with intermittent permeabilities and strengths similar to core sample measurements of coherent oceanic basalt (Fisher, 1998; Violay et al., 2012). Deep eruptive conduits initially contain unstable tephra infill (with heterogeneous fabrics) yet may generate hydrothermal systems that produce rapid lithification and decreases in permeability at the decadal time scale. The physical and mechanical complexities of subaqueous and conduit infill deposits in Surtseyan volcanoes will have implications for predicting sites of future eruptions, the stabilization and longevity of eruptive structures, and perhaps hazard mitigation in cities overlying volcanoes.

## CONCLUSIONS

Time-lapse drilling of cored boreholes at Surtsey in 1979 and 2017 provides a uniquely informative window for exploring the interdependent processes that produce consolidation and lithification in very young, subaqueous, basaltic volcanoes. The integration of laboratory physical property measurements with chemical, mineralogical, and microstructural analyses from 15 lapilli tuff core segments (Figs. 1 and 2), referenced to archival data from the 1979 core (Figs. 4A, 6, 7, and 10), reveals the highly heterogeneous physical characteristics of Surtur pyroclastic deposits (Fig. 13).

Studies of the initiation of alteration in pyroclastic deposits in proximity to the cool pre-eruption seafloor and in a submarine inflow zone, quantified through QPA-XRPD and synchrotron X-ray microdiffraction analyses, reveal that basaltic glass has been largely altered to nanocrystalline clay mineral. Although translucent, yellowish gray (5Y 7/2) domains occur in some pyroclasts (Fig. 3), these domains no longer represent sideromelane, which is defined as fresh basaltic glass. Rather, true basaltic glass is rare (Fig. 5; Jackson et al., 2019a).

The mass proportion of crystalline cements (zeolites, calcium-silicate hydrates, sulfites, and carbonates) and clay mineral(s), ~33–35 wt% and 15–20 wt%, quantified through QPA-XRPD analysis, is similar within the 2017 suite of moderately to strongly lithified lapilli tuff core segments (Fig. 4). X-ray microdiffraction maps of matrix pores reveal diverse alteration paths within the submarine deposits (Kleine et al., 2020; Prause et al., 2020, 2022) and illus-

trate complexities in the material commonly described as palagonite (Fig. 6 and 8). Xonotlite, a layered calcium–silicate–hydrate hydrothermal mineral detected in the 1979 SE-01 core only at 125 m.b.s., at ~141 °C (Jakobsson and Moore, 1986), now occurs in many submarine and sub-seafloor lapilli tuff samples (Fig. 4A; Table 1). This suggests that early temperatures in sub-seafloor deposits close to the eruptive vent (e.g., D12–D15) could have been substantially higher than those of the 2018 borehole measurements, 67–57 °C (Fig. 2C; Weisenberger et al., 2021).

Uniaxial compressive strength, connected porosity, permeability, and P-wave velocity measurements of lapilli tuff subcores show pronounced variations within the submarine, deep-submarine, and subseafloor pyroclastic deposits (Figs. 10–13). Higher borehole temperatures do not necessarily correlate with greater strengths or, by inference, greater abundances of mineral cements and/or more rapid rates of consolidation and lithification. Rather, a model investigating the role of porosity and grain and pore diameter suggests that permeability in the lapilli tuff is largely controlled by the smallest grain size fraction and, therefore, the smallest pore size (Fig. 14A). Subcores with abundant very fine-ash matrix have very low permeability,  $10^{-19}$  m<sup>2</sup> to  $10^{-18}$  m<sup>2</sup>, less than that of subcores of intrusive basalt,  $10^{-17}$  m<sup>2</sup> to  $10^{-16}$  m<sup>2</sup>. A micromechanical model further suggests that compressive strength is dependent on porosity and pore size (Fig. 14B). Subcores with abundant, very fine-ash matrix have high UCS, 45–70 MPa, yet subcores with large vesicular pyroclasts and connected pores have low UCS, 10–16 MPa. Despite pervasive mineral cements, their properties are similar to those of a submarine inflow zone, where fresh glass is preserved in pyroclasts and mineral cements form <2 wt% of the rock (Figs. 4B, 4D, and 5). Cohesion produced by mineral cements thus appears to be a function of bonding across a critical matrix pore size.

Thermal properties of vacuum-dry lapilli tuff subcores also show large differences through the Surtur structure (Figs. 11D, 12E, 12F, and 13E). Effective medium approaches capture variations in thermal conductivity, thermal diffusivity, and specific heat capacity, which allow these parameters to be estimated for both dry (or steam-dominated) and water-saturated conditions, when only porosity is known (Fig. 15).

A deep-submarine zone of strong and compact lapilli tuff near the Surtur eruptive conduit at the level of the pre-eruption seafloor may find expression in the tuff crags of the Vestmannaeyar archipelago that preserve remnants of previous emergent volcanism (Jakobsson et al., 2009; Romagnoli and Jakobsson, 2015; Óskarsson et al., 2020; Fig. 1A). The subseafloor lapilli tuff

corresponds to deposits produced by explosive quarrying of the pre-eruption seafloor, as well as reworked and remobilized tephra in the eruptive conduit (Moore, 1985; McPhie et al., 2020). The well-lithified, subseafloor lapilli tuff and intrusive basalt could further stabilize the subaerial presence of the island over time.

## ACKNOWLEDGMENTS

We dedicate this article to James G. Moore, who inspired the return to drilling on Surtsey and has guided and supported our research since its inception. Funding was provided by the International Continental Scientific Drilling Program (ICDP) through a grant to the Surtsey Underwater Volcanic System for Thermophiles, Alteration Processes and Innovative Concretes (SUSTAIN) project, <https://www.icdp-online.org/projects/by-continent/europe/sustainable/iceland/>; Icelandic Research Fund, ICF-RANNÍS; Bergen Research Foundation and K.G. Jebsen Centre for Deep Sea Research at the University of Bergen, Norway; German Research Foundation (DFG); and DiSTAR, University of Naples, Federico II, Italy. The University of Utah, Salt Lake City, Utah, USA, and Icelandic power companies Reykjavík Energy and Landsvirkjun contributed additional funds. M. Heap was supported by ANR grant MYGALE (Modelling the Physical and Chemical Gradients of Hydrothermal Alteration for Warning Systems of Flank Collapse at Explosive Volcanoes; ANR-21-CE49-0010). M. Heap also acknowledges financial support from the Institut Universitaire de France (IUF). Data acquisition at beamline 12.3.2 at the Advanced Light Source at the Lawrence Berkeley Laboratories, Berkeley, California, USA, was supported by the director of the Office of Science, Department of Energy, under contract no. DE-AC02-05CH11231. J.G. Moore provided archival data and thin sections from the 1979 Surtsey Drilling Project. We thank S. Couper, B.I. Kleine, P. Perez, L.M. Ruff, B. Black, B. Renaud, and T. Reuschlé for research support. Reviews by M. Urlaub and P.-S. Ross substantially improved the article. Full information for the results presented in this article can be found in the Supplemental Material (see footnote 1).

## REFERENCES CITED

- Alexandersson, T., 1972, The sedimentary xenoliths from Surtsey turbidites indicating shelf growth: Surtsey Research Progress Report, v. 6, p. 101–116.
- Axelsson, G., Stefánsson, V., Gudmundsson, G., and Steingrímsson, B., 1982, Thermal condition of Surtsey: Surtsey Research Progress Report, v. 9, p. 102–110.
- Barnes, M.W., and Scheetz, B.E., 1989, The chemistry of Al-tobermorite and its coexisting phases at 175 °C: Materials Research Society Online Proceedings Library, v. 179, p. 243–272, <https://doi.org/10.1557/PROC-179-243>.
- Bélanger, C., and Ross, P.-S., 2018, Origin of nonbedded pyroclastic rocks in the Cathedral Cliff diatreme, Navajo volcanic field, New Mexico: Bulletin of Volcanology, v. 80, no. 7, 61, <https://doi.org/10.1007/s00445-018-1234-0>.
- Benzerara, K., Menguy, N., Banerjee, N.R., Tylliszczak, T., Brown, G.E., Jr., and Guyot, F., 2007, Alteration of submarine basaltic glass from the Ontong Java Plateau: A STXM and TEM study: Earth and Planetary Science Letters, v. 260, no. 1–2, p. 187–200, <https://doi.org/10.1016/j.epsl.2007.05.029>.
- Bergsten, P., Vannier, P., Klonowski, A.M., Knobloch, S., Gudmundsson, M.T., Jackson, M.D., and Marteinsson, V.T., 2021, Basalt-hosted microbial communities in the subsurface of the young volcanic island of Surtsey, Ice-

- land: *Frontiers in Microbiology*, v. 12, <https://doi.org/10.3389/fmicb.2021.728977>.
- Bergsten, P., Vannier, P., Frion, J., Mougeolle, A., and Martheinsson, V.T., 2022, Culturable bacterial diversity from the basaltic subsurface of the young volcanic island of Surtsey, Iceland: *Microorganisms*, v. 10, <https://doi.org/10.3390/microorganisms10061177>.
- Bernstein, S., Thomas, K., and Hochleitner, R., 2009, Crystal chemistry of xonotlite. Part I: Determination of polytypes using X-ray powder diffraction (XRPD): *Neues Jahrbuch für Mineralogie. Abhandlungen*, v. 186, no. 2, p. 153–162, <https://doi.org/10.1127/0077-7757/2009/0139>.
- Caraballo, M.A., Michel, F.M., and Hochellam, M.F., 2015, The rapid expansion of environmental mineralogy in unconventional ways: *The American Mineralogist*, v. 100, p. 14–25, <https://doi.org/10.2138/am-2015-4749>.
- Cole, P.D., Guest, J.E., Duncan, A.M., and Pacheco, J.M., 2001, Capelinhos 1957–1958, Faial, Azores: Deposits formed by an emergent Surtseyan eruption: *Bulletin of Volcanology*, v. 63, p. 204–220, <https://doi.org/10.1007/s004450100136>.
- Colombier, M., et al., 2018, Vesiculation and quenching during Surtseyan eruptions at Hunga Tonga-Hunga Ha'apai volcano, Tonga: *Journal of Geophysical Research: Solid Earth*, v. 123, p. 3762–3779, <https://doi.org/10.1029/2017JB015357>.
- Colombier, M., et al., 2019, In situ granulation by thermal stress during subaqueous volcanic eruptions: *Geology*, v. 47, p. 179–182, <https://doi.org/10.1130/G45503.1>.
- Delpit, S., Ross, P.-S., and Hearn, B.C., 2014, Deep bedded ultramafic diatremes in Missouri River Breaks volcanic field, Montana, USA: 1 km of syn-eruptive subsidence: *Bulletin of Volcanology*, v. 76, no. 7, <https://doi.org/10.1007/s00445-014-0832-8>.
- Di Muro, A., Schwarzlmüller, F., Kueppers, U., Heap, M., and Dingwell, D., 2021, Petrophysical characterisation of volcanic ejecta to constrain subsurface lithological heterogeneities: Implications for edifice stability at basaltic volcanoes: *Volcanica*, v. 4, no. 1, p. 41–66, <https://doi.org/10.30909/vol.04.01.416>.
- Eggertsson, G.H., Lavallée, Y., Kendrick, J.E., and Markússon, S.H., 2020, Improving fluid flow in geothermal reservoirs by thermal and mechanical stimulation: The case of Krafla volcano, Iceland: *Journal of Volcanology and Geothermal Research*, v. 391, <https://doi.org/10.1016/j.jvolgeores.2018.04.008>.
- Escobedo, D., Patrier, P., Beaufort, D., Gilbert, B., Levy, L., Findling, N., and Mortenson, A., 2021, Contribution of the paragenetic sequence of clay minerals to re-examination of the alteration zoning in the Krafla geothermal system: *Minerals*, v. 11, no. 9, <https://doi.org/10.3390/min11090935>.
- Farquharson, J., Heap, M.J., Varley, N.R., Baud, P., and Reuschlé, T., 2015, Permeability and porosity relationships of edifice-forming andesites: A combined field and laboratory study: *Journal of Volcanology and Geothermal Research*, v. 297, p. 52–68, <https://doi.org/10.1016/j.jvolgeores.2015.03.016>.
- Fisher, A.T., 1998, Permeability within basaltic oceanic crust: *Reviews of Geophysics*, v. 36, no. 2, p. 143–182, <https://doi.org/10.1029/97RG02916>.
- Fisher, A.T., and Wheat, C.G., 2010, Seamounts as conduits for massive fluid, heat, and solute fluxes on ridge flanks: *Oceanography*, v. 23, p. 74–87, <https://doi.org/10.5670/oceanog.2010.63>.
- Fisk, M.R., Storrie-Lombardi, M.C., Douglas, S., Popa, R., and Di Meo-Savoie, C., 2003, Evidence of biological activity in Hawaiian subsurface basalts: *Geochemistry, Geophysics, Geosystems*, v. 4, no. 12, 1103, <https://doi.org/10.1029/2002GC000387>.
- Franzson, H., Guðlaugsson, S.P., and Friðleifsson, G.Ó., 2001, Petrophysical properties of Icelandic rocks, in *Proceedings of the Nordic Symposium on Petrophysics*, 6th, Trondheim, Norway: Nordic Energy Research Programme, p. 1–14.
- Gilbert, G.K., 1890, Lake Bonneville: U.S. Geological Survey Monograph 1, 438 p.
- Go, S.Y., and Sohn, Y.K., 2021, Microtextural evidence for vesiculated tuff formation in Songaksan tuff ring, Jeju Island, Korea: *Journal of Volcanology and Geothermal Research*, v. 417, <https://doi.org/10.1016/j.jvolgeores.2021.107311>.
- Grilli, S.T., et al., 2019, Modelling of the tsunami from the December 22, 2018 lateral collapse of Anak Krakatau volcano in the Sunda Straits, Indonesia: *Scientific Reports*, v. 9, no. 1, p. 1–13, <https://doi.org/10.1038/s41598-019-48327-6>.
- Gualtieri, A.F., Riva, V., Bresciani, A., Maretti, S., Tamburini, M., and Viani, A., 2014, Accuracy in quantitative phase analysis of mixtures with large amorphous contents: The case of stoneware ceramics and bricks: *Journal of Applied Crystallography*, v. 47, p. 835–846, <https://doi.org/10.1107/S160057671400627X>.
- Gustafsson, S.E., 1991, Transient plane source techniques for thermal conductivity and thermal diffusivity measurements of solid materials: *The Review of Scientific Instruments*, v. 62, no. 3, p. 797–804, <https://doi.org/10.1063/1.1142087>.
- Hay, R.L., and Iijima, A., 1968, Nature and origin of palagonite tuffs of the Honolulu Group on Oahu, Hawaii, in *Coats, R.R., Hay, R.L., and Anderson, C.A., eds., Studies in Volcanology: Geological Society of America Memoir 116*, p. 331–376, <https://doi.org/10.1130/MEM116-p331>.
- Heap, M.J., and Kennedy, B.M., 2016, Exploring the scale-dependent permeability of fractured andesite: *Earth and Planetary Science Letters*, v. 447, p. 139–150, <https://doi.org/10.1016/j.epsl.2016.05.004>.
- Heap, M.J., and Violay, M.E.S., 2021, The mechanical behaviour and failure modes of volcanic rocks: A review: *Bulletin of Volcanology*, v. 83, no. 33, <https://doi.org/10.1007/s00445-021-01447-2>.
- Heap, M.J., Baud, P., Meredith, P.G., Vinciguerra, S., and Reuschlé, T., 2014, The permeability and elastic moduli of tuff from Campi Flegrei, Italy: Implications for ground deformation modelling: *Solid Earth*, v. 5, p. 25–44, <https://doi.org/10.5194/se-5-25-2014>.
- Heap, M.J., et al., 2015, Mechanical behaviour and failure modes in the Whakaari (White Island volcano) hydrothermal system, New Zealand: *Journal of Volcanology and Geothermal Research*, v. 295, p. 26–42, <https://doi.org/10.1016/j.jvolgeores.2015.02.012>.
- Heap, M.J., et al., 2017a, A multidisciplinary approach to quantify the permeability of the Whakaari/White Island volcanic hydrothermal system (Taupo Volcanic Zone, New Zealand): *Journal of Volcanology and Geothermal Research*, v. 332, p. 88–108, <https://doi.org/10.1016/j.jvolgeores.2016.12.004>.
- Heap, M.J., Kushnir, A.R., Gilg, H.A., Wadsworth, F.B., Reuschlé, T., and Baud, P., 2017b, Microstructural and petrophysical properties of the Permo-Triassic sandstones (Buntsandstein) from the Soutz-sous-Forêts geothermal site (France): *Geothermal Energy*, v. 5, no. 1, p. 1–37, <https://doi.org/10.1186/s40517-017-0085-9>.
- Heap, M.J., Gravelly, D.M., Kennedy, B.M., Gilg, H.A., Bertollet, E., and Barker, S.L., 2020a, Quantifying the role of hydrothermal alteration in creating geothermal and epithermal mineral resources: The Ohakuri ignimbrite (Taupō Volcanic Zone, New Zealand): *Journal of Volcanology and Geothermal Research*, v. 390, <https://doi.org/10.1016/j.jvolgeores.2019.106703>.
- Heap, M.J., Kushnir, A.R.L., Vasseur, J., Wadsworth, F.B., Harlé, P., Baud, P., Kennedy, B.M., Troll, V.R., and Deegan, F.M., 2020b, The thermal properties of porous andesite: *Journal of Volcanology and Geothermal Research*, v. 398, <https://doi.org/10.1016/j.jvolgeores.2020.106901>.
- Heap, M.J., Villeneuve, M., Albino, F., Farquharson, J.I., Brothelande, E., Amelung, F., Got, J.-L., and Baud, P., 2020c, Towards more realistic values of elastic moduli for volcano modelling: *Journal of Volcanology and Geothermal Research*, v. 390, <https://doi.org/10.1016/j.jvolgeores.2019.106684>.
- Heap, M.J., et al., 2022, The thermal properties of hydrothermally altered andesites from La Soufrière de Guadeloupe (Eastern Caribbean): *Journal of Volcanology and Geothermal Research*, v. 421, <https://doi.org/10.1016/j.jvolgeores.2021.107444>.
- Jackson, M.D., 2020, Petrographic and material observations of basaltic lapilli tuff, 1979 and 2017 Surtsey drill cores, Iceland: *Surtsey Research*, v. 14, p. 47–62, <https://doi.org/10.33112/surtsey.14.4>.
- Jackson, M.D., Mulcahy, S.R., Chen, H., Li, Y., Li, Q., Cappelletti, P., and Wenk, H.-R., 2017, Phillipsite and Al-tobermorite mineral cements produced through low-temperature water-rock reactions in Roman marine concrete: *The American Mineralogist*, v. 102, p. 1435–1450, <https://doi.org/10.2138/am-2017-5993CCBY>.
- Jackson, M.D., Couper, S., Stan, C.V., Ivarsson, M., Czabaj, M.W., Tamura, N., Parkinson, D., Miyagi, L.M., and Moore, J.G., 2019a, Authigenic mineral texture in submarine 1979 basalt drill core, Surtsey Volcano, Iceland: *Geochemistry, Geophysics, Geosystems*, v. 20, no. 7, p. 3751–3773, <https://doi.org/10.1029/2019GC008304>.
- Jackson, M.D., et al., 2019b, SUSTAIN drilling at Surtsey volcano, Iceland, tracks hydrothermal and microbiological interactions in basalt 50 years after eruption: *Scientific Drilling*, v. 25, p. 35–46, <https://doi.org/10.5194/sd-25-35-2019>.
- Jakobsson, S.P., 1979, Petrology of recent basalts of the Eastern Volcanic Zone, Iceland: *Acta Naturalia Islandica*, v. 26, p. 1–109.
- Jakobsson, S.P., and Gudmundsson, M.T., 2008, Subglacial and intraglacial volcanic formations in Iceland: *Jökull*, v. 58, p. 179–196.
- Jakobsson, S.P., and Moore, J.G., 1982, The Surtsey research drilling project of 1979: *Surtsey Research*, v. 9, p. 76–93, <https://doi.org/10.33112/surtsey.9.10>.
- Jakobsson, S.P., and Moore, J.G., 1986, Hydrothermal minerals and alteration rates at Surtsey volcano, Iceland: *Geological Society of America Bulletin*, v. 97, p. 648–659, [https://doi.org/10.1130/0016-7606\(1986\)97<648:HMAARA>2.0.CO;2](https://doi.org/10.1130/0016-7606(1986)97<648:HMAARA>2.0.CO;2).
- Jakobsson, S.P., Guðmundsson, G., and Moore, J.G., 2000, Geological monitoring of Surtsey, Iceland, 1967–1998: *Surtsey Research*, v. 11, p. 99–108, <https://doi.org/10.33112/surtsey.11.13>.
- Jakobsson, S.P., Thors, K., Vésteinsson, Á.T., and Ásbjörnsdóttir, L., 2009, Some aspects of the seafloor morphology at Surtsey volcano: The new multibeam bathymetric survey of 2007: *Surtsey Research*, v. 12, p. 9–20, <https://doi.org/10.33112/surtsey.12.2>.
- Kaduk, J.A., Billinge, S.J.L., Dinneber, R.E., Henderson, N., Madsen, I., Černý, R., Leoni, M., Lutterotti, L., Thakral, S., and Chateigner, D., 2021, Powder diffraction: *Nature Reviews: Methods Primers*, v. 1, no. 77, p. 1–22, <https://doi.org/10.1038/s43586-021-00074-7>.
- Kahl, W.-A., Türke, A., and Bach, W., 2021a, X-ray  $\mu$ -CT Data Reconstruction, Image Stack of ICPD Core ICDP5059\_1\_C: PANGAEA, <https://doi.org/10.1594/PANGAEA.935039>.
- Kahl, W.-A., Türke, A., and Bach, W., 2021b, X-ray  $\mu$ -CT data reconstruction, image stack of ICPD Core ICDP5059\_1\_D: PANGAEA, <https://doi.org/10.1594/PANGAEA.932142>.
- Kennedy, B., et al., 2022, Thermal impact of dykes on ignimbrite and implications for fluid flow compartmentalization in a caldera: *Volcanica*, v. 5, no. 1, p. 75–93, <https://doi.org/10.30909/vol.05.01.7593>.
- Kleine, B.L., Stefánsson, A., Kjartansdóttir, R., Prause, S., Weisenberger, T.B., Reynolds, H.I., Sveinbjörnsdóttir, Á.E., Jackson, M.D., and Gudmundsson, M.T., 2020, The Surtsey volcano geothermal system: An analogue for sea-water-oceanic crust interaction with implications for the elemental budget of the oceanic crust: *Chemical Geology*, v. 550, <https://doi.org/10.1016/j.chemgeo.2020.119702>.
- Kokelaar, B.P., and Durant, G.P., 1983, The submarine eruption and erosion of Surtla (Surtsey), Iceland: *Journal of Volcanology and Geothermal Research*, v. 19, p. 239–246, [https://doi.org/10.1016/0377-0273\(83\)90112-9](https://doi.org/10.1016/0377-0273(83)90112-9).
- Le Bas, M.J., Le Maitre, R.W., Streckeisen, A., and Zanettin, B., 1986, A chemical classification of volcanic rocks based on the total alkali-silica diagram: *Journal of Petrology*, v. 27, p. 745–750, <https://doi.org/10.1093/petrology/27.3.745>.
- Lévy, L., Gilbert, B., Sigmundsson, F., Flóvenz, Ó.G., Hersir, G.P., Briole, P., and Pezard, P.A., 2018, The role of smectites in the electrical conductivity of active hydrothermal systems: Electrical properties of core samples from Krafla volcano, Iceland: *Geophysical Journal International*, v. 215, no. 3, p. 1558–1582, <https://doi.org/10.1093/gji/ggy342>.
- Liu, E.J., Cashman, K.V., Rust, A.C., and Gislason, S.R., 2015, The role of bubbles in generating fine ash during hydromagmatic eruptions: *Geology*, v. 43, p. 239–242, <https://doi.org/10.1130/G36336.1>.



- Lorenz, V., 1974, Study of the Surtsey tephra deposits: Surtsey Research Progress Report, v. 7, p. 72–79.
- Marmoni, G.M., Martino, S., Heap, M.J., and Reuschlé, T., 2017, Gravitational slope-deformation of a resurgent caldera: New insights from the mechanical behaviour of Mt. Nuovo tuffs (Ischia Island, Italy): *Journal of Volcanology and Geothermal Research*, v. 345, p. 1–20, <https://doi.org/10.1016/j.jvolgeores.2017.07.019>.
- Marteinsson, V., Klonowski, A., Reynisson, E., Vannier, P., Sigurdsson, B.D., and Ólafsson, M., 2015, Microbial colonization in diverse surface soil types in Surtsey and diversity analysis of its subsurface microbiota: *Biogeosciences*, v. 12, p. 1191–1203, <https://doi.org/10.5194/bg-12-1191-2015>.
- McPhie, J., White, J.D.L., Gorny, C., Jackson, M.D., Gudmundsson, M.T., and Couper, S., 2020, Lithofacies from the 1963–1967 Surtsey eruption in SUSTAIN drill cores SE-2a, SE-2b and SE-03: *Surtsey Research*, v. 14, p. 19–32, <https://doi.org/10.33112/surtsey.14.2>.
- Montesano, G., Rispoli, C., Petrosino, P., Jackson, M.D., Weisenberger, T.B., Gudmundsson, M.T., and Cappelletti, P., 2023, Authigenic mineralization in Surtsey basaltic tuff deposits at 50 years after eruption: *Scientific Reports*, v. 13, 22855, <https://doi.org/10.1038/s41598-023-47439-4>.
- Moore, J.G., 1982, Tidal and leveling measurements on Surtsey, July–August, 1979: *Surtsey Research Progress Report*, v. 9, p. 98–101, <https://doi.org/10.33112/surtsey.9.12>.
- Moore, J.G., 1985, Structure and eruptive mechanism at Surtsey Volcano, Iceland: *Geological Magazine*, v. 122, p. 649–661, <https://doi.org/10.1017/S0016756800032052>.
- Moore, J.G., and Jackson, M.D., 2020, Observations on the structure of Surtsey: *Surtsey Research*, v. 14, p. 33–45, <https://doi.org/10.33112/surtsey.14.3>.
- Moore, J.G., Jakobsson, S., and Holmjarn, J., 1992, Subsidence of Surtsey volcano, 1967–1991: *Bulletin of Volcanology*, v. 55, p. 17–24, <https://doi.org/10.1007/BF00301116>.
- Nikitczuk, M.C.P., Schmidt, M.E., and Flemming, R.L., 2016, Candidate microbial ichnofossils in continental basaltic tuffs of central Oregon, USA: Expanding the record of endolithic microborings: *Geological Society of America Bulletin*, v. 128, p. 1270–1285, <https://doi.org/10.1130/B31380.1>.
- Németh, C., and Kósik, K., 2020, Review of explosive hydrovolcanism: *Geosciences*, v. 10, p. 44, <https://doi.org/10.3390/geosciences10020044>.
- Nono, F., Gibert, B., Parat, F., Loggia, D., Cichy, S.B., and Violay, M., 2020, Electrical conductivity of Icelandic deep geothermal reservoirs up to supercritical conditions: Insight from laboratory experiments: *Journal of Volcanology and Geothermal Research*, v. 391, <https://doi.org/10.1016/j.jvolgeores.2018.04.021>.
- Oddsson, B., 1982, Rock quality designation and drilling rate correlated with lithology and degree of alteration in volcanic rocks from the Surtsey 1979 drill hole: *Surtsey Research Progress Report*, v. 9, p. 94–97, <https://doi.org/10.33112/surtsey.9.11>.
- Ólafsson, M., and Jakobsson, S.P., 2009, Chemical composition of hydrothermal water and water-rock interactions on Surtsey volcanic island: A preliminary report: *Surtsey Research*, v. 12, p. 29–38, <https://doi.org/10.33112/surtsey.12.4>.
- Óskarsson, B.V., Jónasson, K., Valsson, G., and Belart, J.M.C., 2020, Erosion and sedimentation in Surtsey island quantified from new DEMs: *Surtsey Research*, v. 14, p. 63–77, <https://doi.org/10.33112/surtsey.14.5>.
- Peacock, M.A., and Fuller, R.E., 1928, Chlorphaeite, sideromelane and palagonite from the Columbia River plateau: *The American Mineralogist*, v. 13, no. 7, p. 360–383.
- Pauly, B.D., Schiffman, P., Zierenberg, R.A., and Clague, D.A., 2011, Environmental and chemical controls on palagonitization: *Geochemistry, Geophysics, Geosystems*, v. 12, <https://doi.org/10.1029/2011GC003639>.
- Prause, S., Weisenberger, T.B., Cappelletti, P., Grimaldi, C., Rispoli, C., Jónasson, K., Jackson, M.D., and Gudmundsson, M.T., 2020, Alteration progress within the Surtsey hydrothermal system, SW Iceland—A time-lapse alteration study of cores drilled in 1979 and 2017: *Journal of Volcanology and Geothermal Research*, v. 392, <https://doi.org/10.1016/j.jvolgeores.2019.106754>.
- Prause, S., Weisenberger, T.B., Kleine, B., Monien, P., Rispoli, C., and Stefánsson, A., 2022, Alteration of basaltic glass within the Surtsey hydrothermal system, Iceland—Implication to oceanic crust seawater interaction: *Journal of Volcanology and Geothermal Research*, v. 429, <https://doi.org/10.1016/j.jvolgeores.2022.107581>.
- Rhodes, J.M., and Vollinger, M.J., 2004, Composition of basaltic lavas sampled by phase-2 of the Hawaii Scientific Drilling Project: *Geochemical stratigraphy and magma types: Geochemistry, Geophysics, Geosystems*, v. 5, <https://doi.org/10.1029/2002GC000434>.
- Robertson, E.C., and Peck, D.L., 1974, Thermal conductivity of vesicular basalt from Hawaii: *Journal of Geophysical Research: Solid Earth and Planets*, v. 79, no. 32, p. 4875–4888, <https://doi.org/10.1029/JB079i032p04875>.
- Romagnoli, C., and Jakobsson, S.P., 2015, Post-eruptive morphological evolution of island volcanoes: Surtsey as a modern case study: *Geomorphology*, v. 250, p. 384–396, <https://doi.org/10.1016/j.geomorph.2015.09.016>.
- Saar, M.O., and Manga, M., 1999, Permeability-porosity relationship in vesicular basalts: *Geophysical Research Letters*, v. 26, no. 1, p. 111–114, <https://doi.org/10.1029/1998GL900256>.
- Sammis, C.G., and Ashby, M.F., 1986, The failure of brittle porous solids under compressive stress states: *Acta Metallurgica*, v. 34, no. 3, p. 511–526, [https://doi.org/10.1016/0001-6160\(86\)90087-8](https://doi.org/10.1016/0001-6160(86)90087-8).
- Schaefer, L.N., Kendrick, J.E., Oommen, T., Lavallée, Y., and Chigna, G., 2015, Geomechanical rock properties of a basaltic volcano: *Frontiers of Earth Science*, v. 3, no. 29, <https://doi.org/10.3389/feart.2015.00029>.
- Schipper, C.I., Jakobsson, S.P., White, J.D.L., Palin, J.M., and Bush-Marcinowski, T., 2015, The Surtsey magma series: *Scientific Reports*, v. 5, <https://doi.org/10.1038/srep11498>.
- Scott, S.W., Lévy, L., Covell, C., Franzson, H., Gibert, B., Valfels, Á., Newson, J., Frolova, J., Júlíusson, E., and Guðjónsdóttir, M.S., 2023, Valgarður: A database of the petrophysical, mineralogical, and chemical properties of Icelandic rocks: *Earth System Science Data*, v. 15, p. 1165–1195, <https://doi.org/10.5194/essd-15-1165-2023>.
- Shaw, S., Clark, S.M., and Henderson, C.M.B., 2000, Hydrothermal formation of the calcium silicate hydrates, tobermorite (Ca<sub>2</sub>Si<sub>4</sub>O<sub>16</sub>(OH)<sub>2</sub> · 4H<sub>2</sub>O) and xonotlite (Ca<sub>6</sub>Si<sub>6</sub>O<sub>17</sub>(OH)<sub>2</sub>): An in situ synchrotron study: *Chemical Geology*, v. 167, p. 129–140, [https://doi.org/10.1016/S0009-2541\(99\)00205-3](https://doi.org/10.1016/S0009-2541(99)00205-3).
- Smith, R.J., and Horgan, B.H.N., 2021, Nanoscale variations in natural amorphous and nanocrystalline weathering products in mafic to intermediate volcanic terrains on Earth: Implications for amorphous detections on Mars: *Journal of Geophysical Research: Planets*, v. 126, <https://doi.org/10.1029/2020JE006769>.
- Snyder, R.L., and Bish, D.L., 1989, Quantitative analysis, in Snyder, R.L., and Bish, D.L., eds., *Modern Powder Diffraction: De Gruyter*, p. 101–144, <https://doi.org/10.1515/9781501509018-008>.
- Stan, C.V., and Tamura, N., 2018, Synchrotron X-ray microdiffraction and fluorescence imaging of mineral and rock samples: *Journal of Visualized Experiments*, v. 136, <https://doi.org/10.3791/57874>.
- Staudigel, H., 2014, Chemical fluxes from hydrothermal alteration of the oceanic crust, in Holland, H.D., and Turekian, K.K., eds., *Treatise on Geochemistry* (second edition): Elsevier, p. 583–606, <https://doi.org/10.1016/B978-0-08-095975-7.00318-1>.
- Staudigel, H., and Hart, S.R., 1983, Alteration of basaltic glass: Mechanisms and significance for the oceanic crust-seawater budget: *Geochimica et Cosmochimica Acta*, v. 47, no. 3, p. 337–350, [https://doi.org/10.1016/0016-7037\(83\)90257-0](https://doi.org/10.1016/0016-7037(83)90257-0).
- Stefánsson, A., and Gislason, S.R., 2001, Chemical weathering of basalts, southwest Iceland: Effect of rock crystallinity and secondary minerals on chemical fluxes to the ocean: *American Journal of Science*, v. 301, p. 513–556, <https://doi.org/10.2475/ajs.301.6.513>.
- Stefánsson, V., Axelsson, G., Sigurdsson, O., Gudmundsson, G., and Steingrímsson, B., 1985, Thermal condition of Surtsey: *Journal of Geodynamics*, v. 4, p. 91–106, [https://doi.org/10.1016/0264-3707\(85\)90054-7](https://doi.org/10.1016/0264-3707(85)90054-7).
- Stronck, N.A., and Schmincke, H.-U., 2002, Palagonite—A review: *International Journal of Earth Sciences*, v. 91, p. 680–697, <https://doi.org/10.1007/s00531-001-0238-7>.
- Sunamura, T., 2021, A model for wave abrasion on underwater bedrock, with an application to rapidly downwearing tephra cones adjacent to Surtsey Island in Iceland: *Earth Surface Processes and Landforms*, v. 46, no. 8, p. 1600–1609, <https://doi.org/10.1002/esp.5128>.
- Tamura, N., 2014, XMAS: A versatile tool for analyzing synchrotron microdiffraction data, in Ice, G., and Barabash, B., eds., *Strain and Dislocation Gradients from Diffraction*: World Scientific, p. 125–155, [https://doi.org/10.1142/9781908979636\\_0004](https://doi.org/10.1142/9781908979636_0004).
- Terry, J.P., et al., 2022, Tonga volcanic eruption and tsunami, January 2022: *Geoscience Letters*, v. 9, no. 24, <https://doi.org/10.1186/s40562-022-00232-z>.
- Thorarinsson, S., 1965, Some facts about the Surtsey eruption: *Náttúrufræðingurinn*, v. 35, p. 153–181.
- Thorarinsson, S., 1967, Surtsey, The New Island in the North Atlantic: Viking Press.
- Thorarinsson, S., Einarsson, T., Sigvaldason, G., and Elisson, G., 1964, The submarine eruption off the Vestmann Islands 1963–64: *Bulletin Volcanologique*, v. 27, p. 435–445, <https://doi.org/10.1007/BF02597544>.
- Thors, K.J., and Jakobsson, S.P., 1982, Two seismic reflection profiles from the vicinity of Surtsey, Iceland: *Surtsey Research Progress Report*, v. 9, p. 149–151, <https://doi.org/10.33112/surtsey.9.18>.
- Toby, B.H., 2006, R factors in Rietveld analysis: How good is good enough?: *Powder Diffraction*, v. 21, no. 1, p. 67–70, <https://doi.org/10.1154/1.2179804>.
- Valentine, G.A., and White, J.D.L., 2012, Revised conceptual model for maar-diatremes: Subsurface processes, energetics, and eruptive products: *Geology*, v. 40, p. 1111–1114, <https://doi.org/10.1130/G33411.1>.
- Vanorio, T., Prasad, M., Patella, D., and Nur, A., 2002, Ultrasonic velocity measurements in volcanic rocks: Correlation with microtexture: *Geophysical Journal International*, v. 149, p. 22–36, <https://doi.org/10.1046/j.0956-540x.2001.01580.x>.
- Verolino, A., White, J.D.L., and Brenna, M., 2018, Eruption dynamics at Pahvant Butte volcano, Utah, western USA: Insights from ash-sheet dispersal, grain size, and geochemical data: *Bulletin of Volcanology*, v. 80, no. 81, <https://doi.org/10.1007/s00445-018-1256-7>.
- Verolino, A., White, J.D.L., Baxter, R.J.M., Schipper, C.I., and Thordarson, T., 2022, Characteristics of sub-aerially emplaced pyroclasts in the Surtsey eruption deposits: Implications for diverse Surtseyan eruptive styles: *Geosciences*, v. 12, no. 2, <https://doi.org/10.3390/geosciences12020079>.
- Vinciguerra, S., Del Gaudio, P., Mariucci, M.T., Marra, F., Meredith, P.G., Montone, P., Pierdominici, S., and Scarlato, P., 2009, Physical properties of tuffs from a scientific borehole at Alban hills volcanic district (central Italy): *Tectonophysics*, v. 471, no. 1–2, p. 161–169, <https://doi.org/10.1016/j.tecto.2008.08.010>.
- Violay, M., Gibert, B., Mainprice, D., Evans, B., Dauria, J.M., Azais, P., and Pezard, P., 2012, An experimental study of the brittle-ductile transition of basalt at oceanic crust pressure and temperature conditions: *Journal of Geophysical Research: Solid Earth*, v. 117, no. B3, <https://doi.org/10.1029/2011JB008884>.
- Violay, M., Gibert, B., Mainprice, D., and Burg, J.P., 2015, Brittle versus ductile deformation as the main control of the deep fluid circulation in oceanic crust: *Geophysical Research Letters*, v. 42, no. 8, p. 2767–2773, <https://doi.org/10.1002/2015GL063437>.
- von Waltershausen, W.S., 1853, Über die vulkanische Gesteine in Sicilien und Island und ihre Submarine Umbildung: Cambridge University Press, <https://doi.org/10.1017/CBO9781139226882>.
- Vosteen, H.D., and Schellschmidt, R., 2003, Influence of temperature on thermal conductivity, thermal capacity and thermal diffusivity for different types of rock: *Physics and Chemistry of the Earth, Parts A/B/C*, v. 289, p. 499–509, [https://doi.org/10.1016/S1474-7065\(03\)00069-X](https://doi.org/10.1016/S1474-7065(03)00069-X).

- Wadsworth, F.B., Vasseur, J., Scheu, B., Kendrick, J.E., Lavallée, Y., and Dingwell, D.B., 2016, Universal scaling of fluid permeability during volcanic welding and sediment diagenesis: *Geology*, v. 44, p. 219–222, <https://doi.org/10.1130/G37559.1>.
- Walker, R.J., Holdsworth, R.E., Armitage, P.J., and Faulkner, D.R., 2013, Fault zone permeability structure evolution in basalts: *Geology*, v. 41, p. 59–62, <https://doi.org/10.1130/G33508.1>.
- Walter, T.R., et al., 2019, Complex hazard cascade culminating in the Anak Krakatau sector collapse: *Nature Communications*, v. 10, no. 1, p. 1–11, <https://doi.org/10.1038/s41467-019-12284-5>.
- Warr, L., 2021, IMA–CNMNC approved mineral symbols: *Mineralogical Magazine*, v. 85, no. 3, p. 291–320, <https://doi.org/10.1180/mgm.2021.43>.
- Weisenberger, T.B., et al., 2019, Operational Report for the 2017 Surtsey Underwater volcanic System for Thermophiles, Alteration processes and INnovative concretes (SUSTAIN) drilling project at Surtsey Volcano, Iceland: GFZ German Research Centre for Geosciences, <https://doi.org/10.2312/ICDP.5059.001>.
- Weisenberger, T.B., et al., 2021, The SUSTAIN ICDP Drilling Project on Surtsey, in *Proceedings, World Geothermal Congress 2020+1*, Reykjavik, Iceland, April–October 2021: World Geothermal Congress, record no. 34556, <http://www.geothermal-energy.org/pdf/IGAstandard/WGC/2020/12068.pdf>.
- Weisenberger, T.B., Gudmundsson, M.T., Gunnarson, B.T., Jørgensen, S.L., and Jackson, M.D., 2022, Measurements of the inclination of the SE-03 borehole on Surtsey Volcano: *Surtsey Research*, v. 15, p. 121–126, <https://doi.org/10.33112/surtsey.15.9>.
- Wenk, H.-R., Joswig, W., Tagai, T., Korekawa, M., and Smith, B.K., 1980, The average structure of An 62–66 labradorite: *The American Mineralogist*, v. 65, p. 81–95.
- Wohletz, K., Zimanowski, B., and Buttner, R., 2013, Magma-water interactions, in Fagents, S.A., Gregg, T.K.P., and Lopes, R.M.C., eds., *Modeling Volcanic Processes*: Cambridge University Press, p. 230–257, <https://doi.org/10.1017/CBO9781139021562.011>.
- White, J.D.L., 1996, Pre-emergent construction of a lacustrine basaltic volcano, Pahvant Butte, Utah (USA): *Bulletin of Volcanology*, v. 58, p. 249–262, <https://doi.org/10.1007/s004450050138>.
- White, J.D.L., and Houghton, B.F., 2006, Primary volcaniclastic rocks: *Geology*, v. 34, p. 677–680, <https://doi.org/10.1130/G22346.1>.
- White, J.D.L., and Ross, P.-S., 2011, Maar-diatreme volcanoes: A review: *Journal of Volcanology and Geothermal Research*, v. 201, p. 1–29, <https://doi.org/10.1016/j.jvolgeores.2011.01.010>.
- Zhou, Z., and Fyfe, W., 1989, Palagonitization of basaltic glass from DSDP Site 335, Leg 37: *The American Mineralogist*, v. 74, p. 1045–1053.
- Zhou, Z., Fyfe, W.S., Tazaki, K., and Van de Gaast, S.J., 1992, The structural characteristics of palagonite from DSDP site 335: *Canadian Mineralogist*, v. 30, p. 75–81.
- Zhu, W., Baud, P., and Wong, T.F., 2010, Micromechanics of cataclastic pore collapse in limestone: *Journal of Geophysical Research: Solid Earth*, v. 115, no. B4, <https://doi.org/10.1029/2009JB006610>.
- Zhu, W., Baud, P., Vinciguerra, S., and Wong, T.F., 2011, Micromechanics of brittle faulting and cataclastic flow in Alban Hills tuff: *Journal of Geophysical Research: Solid Earth*, v. 116, no. B6, <https://doi.org/10.1029/2010JB008046>.

SCIENCE EDITOR: MIHAI DUCEA  
ASSOCIATE EDITOR: MICHAEL ORT

MANUSCRIPT RECEIVED 14 MARCH 2023  
REVISED MANUSCRIPT RECEIVED 25 OCTOBER 2023  
MANUSCRIPT ACCEPTED 11 DECEMBER 2023